High-resolution reconstructions of Pacific–North America plate motion: 20 Ma to present

C. DeMets[1] and S. Merkouriev[2,3]

[1]*Department of Geoscience, University of Wisconsin-Madison, Madison, WI 53706, USA. E-mail:* chuck@geology.wisc.edu
[2]*Pushkov Institute of Terrestrial Magnetism of the Russian Academy of Sciences, St Petersburg Filial. 1 Mendeleevskaya Liniya, St. Petersburg 199034, Russia*
[3]*Institute of Earth Sciences, Saint Petersburg State University, Universitetskaya nab., 7-9, St. Petersburg, 199034, Russia*

SUMMARY

We present new rotations that describe the relative positions and velocities of the Pacific and North America plates at 22 times during the past 19.7 Myr, offering ≈1-Myr temporal resolution for studies of the geotectonic evolution of western North America and other plate boundary locations. Derived from ≈18 000 magnetic reversal, fracture zone and transform fault identifications from the Pacific–Antarctic–Nubia–North America plate circuit and the velocities of 935 GPS sites on the Pacific and North America plates, the new rotations and GPS-derived angular velocity indicate that the rate of motion between the two plates increased by ≈70 per cent from 19.7 to 9±1 Ma, but changed by less than 2 per cent since 8 Ma and even less since 4.2 Ma. The rotations further suggest that the relative plate direction has rotated clockwise for most of the past 20 Myr, with a possible hiatus from 9 to 5 Ma. This conflicts with previously reported evidence for a significant clockwise change in the plate direction at ≈8–6 Ma. Our new rotations indicate that Pacific plate motion became obliquely convergent with respect to the San Andreas Fault of central California at 5.2–4.2 Ma, in agreement with geological evidence for a Pliocene onset of folding and faulting in central California. Our reconstruction of the northern Gulf of California at 6.3 Ma differs by only 15–30 km from structurally derived reconstructions after including 3–4 km Myr^{-1} of geodetically measured slip between the Baja California Peninsula and Pacific plate. This implies an approximate 15–30 km upper bound for plate non-rigidity integrated around the global circuit at 6.3 Ma. A much larger 200±54 km discrepancy between our reconstruction of the northern Gulf of California at 12 Ma and that estimated from structural and marine geophysical observations suggests that faults in northwestern Mexico or possibly west of the Baja California Peninsula accommodated large amounts of obliquely divergent dextral shear from 12–6.3 Ma. Pacific–North America plate motion since 16 Myr estimated with our new rotations agrees well with structurally summed deformation along two transects of western North America between the Colorado Plateau and western California, with a difference as small as 40 km out of 760 km of margin-parallel motion. A strong resemblance between a 20-Myr-to-present flow line reconstructed with our new rotations and the traces of the 700-km-long Queen Charlotte Fault and continental slope west of Canada suggests that the plate margin geometry was influenced by the passage of the Pacific plate and Yakutat block. The new rotations also suggest that (1) oblique convergence west of Canada initiated at 12–11 Ma, 5–8 Myr earlier than previously estimated, (2) no significant margin-normal shortening has occurred in areas of Canada located east of the Haida Gwaii archipelago since 20 Ma and (3) Pacific plate underthrusting of Haida Gwaii has accommodated the margin-normal component of plate motion since 12–11 Ma. Our rotations suggest an ≈70 per cent increase in the rate that the Pacific plate has been consumed by subduction beneath the Aleutian arc since 19.7 Ma, with still-unknown consequences for the rate of arc magmatism.

Key words: Plate motions; Continental margins: transform; North America.

1 INTRODUCTION

The approach of the Pacific–Farallon Rise with North America's western margin between ~28 and 12 Myr fragmented the eastward-subducting Farallon plate into a series of oceanic microplates that ultimately subducted beneath North America or attached to the Pacific plate (Atwater 1970; Atwater 1989; Lonsdale 1991; Michaud *et al.* 2006). The corresponding, gradual change from convergent plate motion along the western margin to dextral shear profoundly affected the geotectonic evolution of large areas of western North America. At a regional scale, dextral shear along North America's western margin initiated distributed extension in the northern and central Basin and Range Province (e.g. Snow & Wernicke 2000; McQuarrie & Wernicke 2005; Colgan *et al.* 2006). Farther south, broadly distributed extension in northwestern Mexico before 12 Ma (e.g. Oskin & Stock 2003; Seiler *et al.* 2010; Bennett *et al.* 2013) transferred to faults in the proto-Gulf of California between 12 and ~6 Ma (Stock & Hodges 1989; Oskin *et al.* 2001; Sutherland *et al.* 2012), thereby detaching the Baja California Peninsula from North America and opening the modern Gulf of California (Larson *et al.* 1968). Numerous, more localized effects include the capture of the now-extinct Monterey microplate by the Pacific plate (Fig. 1), which rotated the western Transverse Ranges of southern California into their present position and influenced the geometry of the San

Andreas Fault in southern California (e.g. Luyendyk *et al.* 1980, 1985; Luyendyk 1991; Nicholson *et al.* 1994), and a postulated clockwise rotation of Pacific–North America plate motion after ≈5 Ma (Harbert & Cox 1989; Page *et al.* 1998) that may have triggered the Pliocene-to-recent folding, faulting, and topographic uplift in central California.

Efforts to quantify Pacific–North America plate motion initiated shortly after the exposition of the theory of plate tectonics. In the seminal paper on the topic, Atwater (1970) used seafloor spreading magnetic lineations west of North America to reconstruct the Cenozoic positions and velocities of the Pacific, Farallon, Kula, Juan de Fuca and Rivera plates relative to North America assuming that motion between the Pacific and North America plates during the entire Cenozoic was parallel to the San Andreas Fault at a constant rate of 60 mm yr^{-1}. Atwater & Molnar (1973) subsequently estimated Pacific–North America plate rotations for the past 38 Myr by summing rotations around a global plate circuit defined by the Pacific–Antarctic, Antarctic–Africa and Africa–North America plate boundaries (Fig. 2). Subsequent authors have estimated Pacific–North America rotations using either the same plate circuit (e.g. Stock & Molnar 1988; Atwater & Stock 1998; Argus & Gordon 2001; Wilson *et al.* 2005; Royer *et al.* 2006; Doubrovine & Tarduno 2008) or by linking the Africa plate to the Pacific plate via their respective hotspot tracks and assuming fixity between hotspots
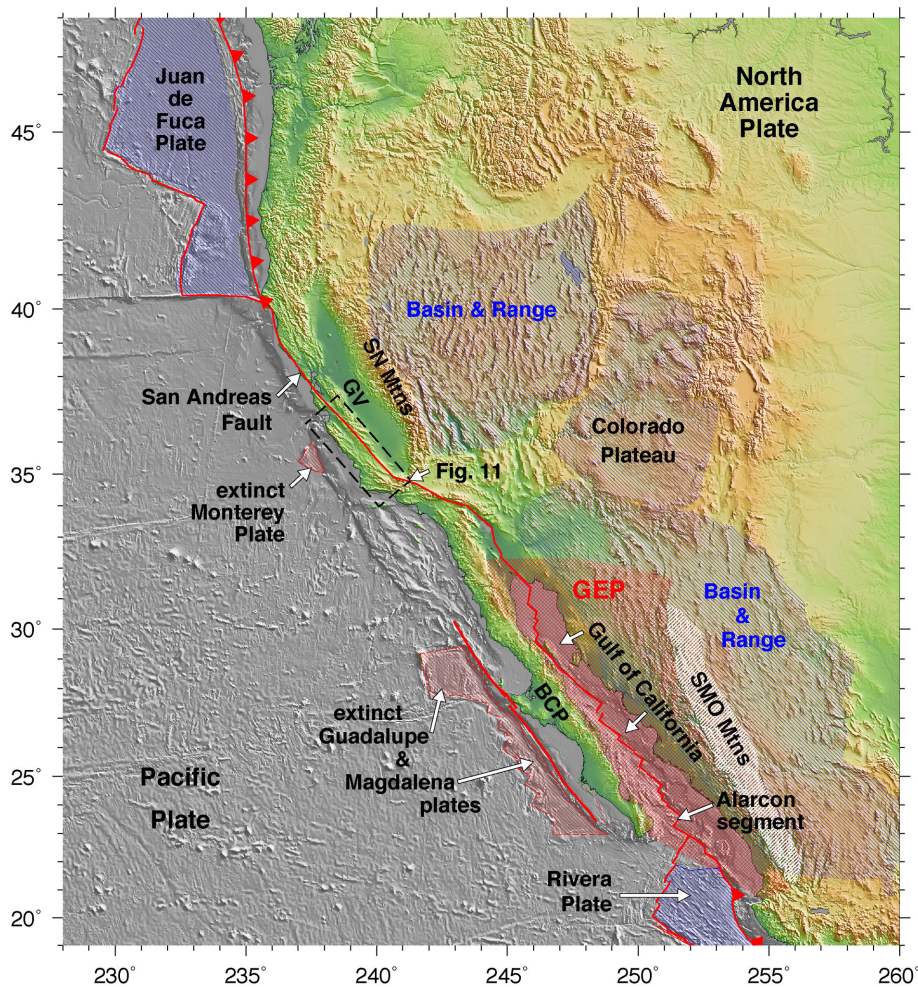
Figure 1. Locations of major features described in the text. Abbreviations: BCP, Baja California Peninsula; GEP, Gulf Extensional Province; GV, Great Valley; SMO, Sierra Madre Occidentale; SN Mtns, Sierra Nevada Mountains.
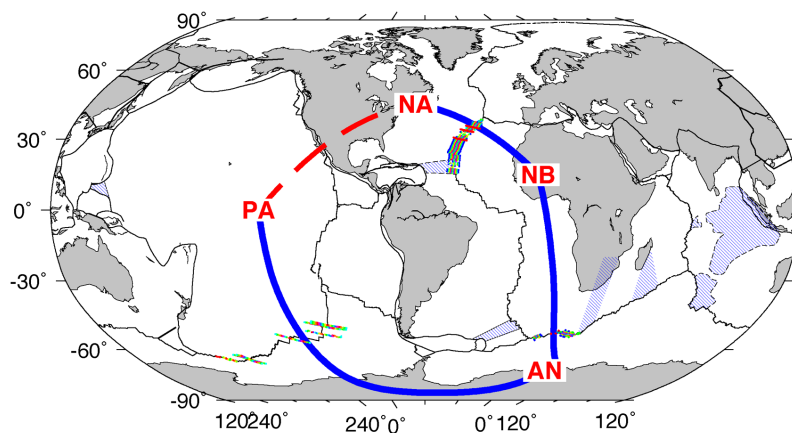
Figure 2. Plate circuit and plate kinematic observations used to estimate Pacific–North America finite and stage rotations. Small coloured circles show the locations of nearly 13 000 magnetic reversal identifications that were reconstructed to estimate Nubia–North America (Merkouriev & DeMets 2014), Nubia–Antarctica (DeMets *et al.* 2015b) and Pacific–Antarctic (Croon *et al.* 2008) finite rotations for the past 20 Myr. Plate name abbreviations are as follows: AN, Antarctic; NA, North America; NB, Nubia; PA, Pacific.

in the Pacific and Atlantic basins (Engebretson *et al.* 1985; Harbert & Cox 1989). Angular velocities that describe Pacific–North America plate motion during the past 1–3 Myr have also been estimated from inversions of globally distributed seafloor spreading rates, oceanic transform fault azimuths, and earthquake slip directions (Chase 1972; Minster *et al.* 1974; Minster & Jordan 1978; DeMets *et al.* 1990, 1994, 2010).

Herein, we determine a new sequence of Pacific–North America plate rotations for the past 20 Myr, spanning most of the time the two plates have shared a boundary in western North America. Following Atwater & Molnar (1973) and some subsequent authors, we combine finite rotations from the Pacific–Antarctica–Nubia–North America plate circuit to estimate Pacific–North America rotations. We also estimate an instantaneous angular velocity from the velocities of 935 GPS sites on the Pacific and North America plates. The newly determined rotations differ from previous estimates in several respects. First, 22 independent rotations spanning the past 19.7 Myr are estimated, an average of only ∼1-Myr between rotations. The closely spaced rotations provide better temporal resolution, more redundancy, and require less interpolation than do previous estimates. Second, the new rotations are derived from ∼18 000 identifications of magnetic reversals and fracture zones (Fig. 2) from up-to-date compilations and analyses of magnetic anomaly and bathymetric data from all three boundaries in the global plate circuit (Croon *et al.* 2008; Merkouriev & DeMets; 2014; DeMets *et al.* 2015b). Many of the magnetic reversals were identified from dense magnetic surveys of the three constituent plate circuit boundaries, an effective means of reducing magnetic reversal miscorrelations that can adversely affect rotation accuracies. Third, we use a newly described Bayesian methodology (Iaffaldano *et al.* 2012, 2014) to reduce noise in each of the constituent plate circuit rotation sequences prior to estimating Pacific–North America rotations. Finally, all of the rotations are corrected for the biasing effects of outward displacement, a significant, potential error source in young rotations (DeMets & Wilson 2008).

2 DATA

2.1 Finite rotation sequences

The Pacific–Antarctic-Nubia–North America plate circuit rotations that are the basis for our new estimates of Pacific–North America

finite rotations and stage angular velocities are taken from four sources. For the Pacific–Antarctic leg of the plate circuit, we use 22 finite rotations derived by Croon *et al.* (2008) from 616 crossings of magnetic reversals 1n (0.781 Ma) through 6no (19.722 Ma) and 915 fracture zone crossings well distributed along the Pacific–Antarctic rise. The Croon *et al.* rotations satisfy the Hellinger (1981) great-circle criteria for reconstructing conjugate segments of magnetic reversal and fracture crossings (also see Chang 1987, 1988). We describe noise-reduced rotations determined from the Croon *et al.* (2008) best-fitting rotations in Section 4.1.

For the Nubia–North America leg of the plate circuit, we use best-fitting finite rotations from Merkouriev & DeMets (2014) and noise-reduced rotations determined by DeMets *et al.* (2015a) from those best-fitting rotations. The best-fitting rotations reconstruct ≈13 000 magnetic reversal, fracture zone, and transform fault crossings from the Mid-Atlantic Ridge from ≈15° to 37°N at 21 times from Chron 1n to Chron 6. The rotations that best fit these observations satisfy the Hellinger (1981) great-circle fitting criteria for magnetic reversal crossings, the Shaw & Cande (1990) flow-line methodology for fracture zone crossings, and a small-circle fitting function for transform fault crossings (Merkouriev & DeMets 2014). The noise-reduced rotations were determined using the same Bayesian methodology as is described in Section 3.3.

The Nubia–Antarctic finite rotations are from DeMets *et al.* (2015b), who estimate best-fitting and noise-reduced rotations for 19 times back to Chron 6 from ∼3500 Southwest Indian Ridge magnetic reversal, fracture zone, and transform fault crossings located between the Bouvet Triple Junction (0°E) and the Andrew Basin transform fault (∼32°E). The rotations were estimated using the same fitting criteria and Bayesian methodology as for the Nubia–North America rotations.

None of the rotation sequences listed above have been used by previous authors to estimate Pacific–North America rotations. Consequently, the newly estimated Pacific–North America rotations are independent of all previous estimates. Notable differences between the rotations we use for the three adjacent plate pairs and previously published estimates include the following: (1) The circuit rotations used herein are spaced every ≈1 Myr, much closer than the ≈3–10 Myr spacing typical of the rotations used for previous studies. (2) Most of the circuit rotations described above were estimated from 10–100 times more data than for previous studies. (3) The new rotation sequences define significant changes in

Table 1. GPS-derived angular velocities.

Chron	Lat. (°N)	Long. (°E)	$\dot{\omega}$ (° Myr^{-1})	Covariances					
				a	*b*	*c*	*d*	*e*	*f*
NA-IGS08	−6.49	271.53	0.184	0.45	−0.48	0.36	15.83	−11.03	8.34
PA-IGS08	−62.58	110.85	0.679	51.80	9.95	−2.50	13.36	0.89	14.95
NA-PA	49.95	283.74	0.760	52.28	9.47	−2.14	30.19	−10.15	23.29
SN-PA*	46.47	272.19	0.733	2.94**	5.10**	−4.42**	8.73**	−7.68**	6.79**

These angular velocities describe rotation of the first listed plate relative to either IGS08 or the second listed plate. The IGS08 reference frame is constrained to evolve in a manner identical to ITRF08 (Altamimi *et al.* 2011), hence the angular velocities are the same as if ITRF08 were the geodetic reference frame. The angular rotation rate $\dot{\omega}$ has units of degrees Myr^{-1}. Angular velocity covariances either have units of 10^{-11} radians^2 Myr^{-2}, or if marked by a double asterisk, 10^{-8} radians^2 Myr^{-2}. Abbreviations: NA, North America plate; PA, Pacific plate; SN, Sierra Nevada-Great Valley block. * The SN-PA angular velocity and its covariances were derived by combining the NA-PA angular velocity in the table with an angular velocity of 26.1°S, 196.7°E, 0.113° Myr^{-1}, which describes the present motion of the SNGV block relative to North America (McCaffrey 2015). Elements *a*, *d*, and *f* are the variances of the (0°N, 0°E), (0°N, 90°E), and 90°N components of the rotation. The covariance matrices are reconstructed as follows:

$$\begin{pmatrix} a & b & c \\ b & d & e \\ c & e & f \end{pmatrix}$$

Nubia–Antarctic and Nubia–North America plate motions undetected by previous, lower-resolution studies of these plate boundaries. (4) The noise-reduced rotation sequences used herein describe simpler plate motion histories than do previously published estimates. Comparisons of the fits of the simpler, noise-reduced rotations and the noisier, best-fitting rotations for the Nubia–North America and Nubia–Antarctic plate pairs show no significant fitting penalty with respect to the underlying plate kinematic data (DeMets *et al.* (2015a,b). Readers are referred to Croon *et al.* (2008), Merkouriev & DeMets (2014) and DeMets *et al.* (2015a,b) for more details.

2.2 GPS site velocities

We estimated an instantaneous Pacific–North America angular velocity (Table 1) from the velocities of 908 GPS sites on the North America plate and 27 Pacific plate GPS stations. The raw GPS data span the period January 1993 to November 2015. The methods used to process the raw GPS observations are documented in Section 1 of the Supporting Information.

Fig. 3(a) shows the locations of the 908 GPS sites that we used to estimate the North America plate angular velocity. We omitted all stations from areas affected by extension across the central and
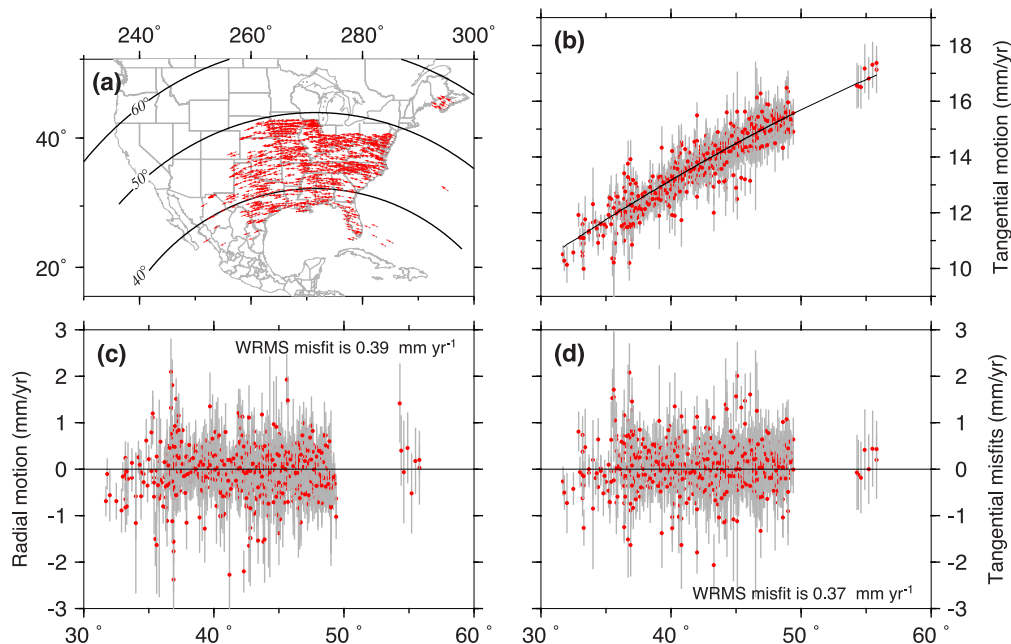
Figure 3. Velocities and locations of 908 GPS stations used to estimate the instantaneous North America-IGS08 angular velocity. (a) Station velocities in IGS08. Small circles show angular distances from the best-fitting North America-IGS08 pole. (b) Component of station velocities parallel to the small circle around the best-fitting pole (red circles). Grey lines show the estimated standard errors. Black line shows the velocity component at each site as estimated with the best-fitting angular velocity. (c) Component of station velocities that is locally orthogonal to the small circle around the best-fitting pole. For an undeforming plate, the radial component at each site should be zero since sites should move neither towards nor away from their pole of rotation. 'WRMS' gives the weighted root-mean-square misfit of the best-fitting angular velocity to the observations. (d) Residual tangential velocity components, defined as the observed minus the estimated values shown in (b).

northwestern Basin and Range (e.g. Bennett *et al.* 1999), rotation of the Colorado Plateau (Kreemer *et al.* 2010) and/or elastic shortening associated with Rivera and Cocos plate subduction beneath western Mexico (Marquez-Azua & DeMets 2009). We also excluded sites from areas affected by glacial isostatic adjustment (GIA), including nearly all of Canada and large swaths of the northern United States (Calais *et al.* 2006; Sella *et al.* 2007). Section 2 and Supporting Information Figs S1 and S2 provide more information about the method that we used to identify areas of the plate affected by GIA and the dependence of our estimated angular velocity on the subset of the GPS site velocities that were inverted to estimate the North America plate angular velocity.

The 908 North America plate GPS station velocities vary sinusoidally with angular distance from their best-fitting pole, as expected (Fig. 3b). The tangential and radial components of the GPS site velocities are well fit by the best-fitting angular velocity (Figs 3c and d), with respective, weighted root-mean-square misfits of only 0.37 and 0.39 mm yr^{-1}. Reduced chi-square, the least-squares misfit normalized by the degrees of freedom, is 0.93, indicating that the average weighted misfits are 4 per cent smaller than the estimated velocity uncertainties. The station velocities are thus jointly consistent with the hypotheses that the plate interior does not deform measurably within the geographic limits spanned by the 908 sites and that the velocity uncertainties are approximately correct.

The distribution and velocities of the 27 GPS sites used to estimate the Pacific plate angular velocity (Table 1) are nearly the same as those described by DeMets *et al.* (2014a). Readers are thus referred to DeMets *et al.* (2014a) for further information.

3 METHODS

3.1 Estimation of plate rotations and uncertainties

Two types of Pacific–North America finite rotations are employed for the analysis. Best-fitting rotations are derived from the rotations that best reconstruct the numerous magnetic reversal and fracture zone data from the three plate circuit boundaries. In contrast noise-reduced rotations are derived by combining alternative plate circuit rotations based on Bayesian analyses of the best-fitting rotations for each of the three adjacent plate pairs in the global circuit. The Bayesian method is described briefly in Section 3.3 and documented in detail by Iaffaldano *et al.* (2012, 2014).

The best-fitting and noise-reduced Pacific–North America finite rotations and their covariances were determined using standard methods for combining finite rotations around a plate circuit (e.g. Chang *et al.* 1990; Kirkwood *et al.* 1999; Doubrovine & Tarduno 2008). In particular, finite rotations $\hat{A}_{\text{PA}\rightarrow\text{NA}}$ that reconstruct the Pacific plate onto North America were derived following

$$\hat{A}_{\text{PA}\rightarrow\text{NA}} = (\hat{A}_{\text{NB}\rightarrow\text{NA}})(\hat{A}_{\text{AN}\rightarrow\text{NB}})(\hat{A}_{PA\rightarrow\text{AN}}) \qquad (1)$$

where for example $\hat{A}_{\text{PA}\rightarrow\text{AN}}$ describes the estimated rotation $\hat{A}$ for the Pacific onto the Antarctic plate (see eq. 2 of Doubrovine & Tarduno 2008). The 3 × 3 covariance matrices $C_{\text{PA}\rightarrow\text{NA}}$ that describe the uncertainties in $\hat{A}_{\text{PA}\rightarrow\text{NA}}$ were determined by propagating the rotation covariances for each of the circuit plate pairs around the plate circuit following eq. (3) from Doubrovine & Tarduno (2008). In particular,

$$C_{\text{PA}\rightarrow\text{NA}} = (\hat{A}_{\text{PA}\rightarrow\text{NB}})^T C_{\text{NB}\rightarrow\text{NA}} (\hat{A}_{\text{PA}\rightarrow\text{NB}})$$
$$+ (\hat{A}_{\text{PA}\rightarrow\text{AN}})^T C_{\text{AN}\rightarrow\text{NB}} (\hat{A}_{\text{PA}\rightarrow\text{AN}}) + C_{\text{PA}\rightarrow\text{AN}}, \qquad (2)$$

where $\hat{A}_{\text{PA}\rightarrow\text{NB}} = \hat{A}_{\text{AN}\rightarrow\text{NB}}\hat{A}_{\text{PA}\rightarrow\text{AN}}$. The operations in eq. (2) transform the covariances $C_{\text{NB}\rightarrow\text{NA}}$ and $C_{\text{AN}\rightarrow\text{NB}}$ into the same Pacific plate coordinate system as for the Pacific–Antarctic covariances from table 1 of Croon *et al.* (2008). The rotation covariances follow the Chang *et al.* (1990) convention whereby the covariances travel with the moving rather than the fixed plate. Operations related to eq. (2) were carried out with the ADDROT algorithm (Royer & Chang 1991, also see eq. 19 in Kirkwood *et al.* 1999).

Three types of rotation covariances are used herein. Rotation covariances that were determined using the method of Chang (1988) (also see Chang *et al.* 1990 and Kirkwood *et al.* 1999) depend in part on the geographic distribution of the data on each plate and by convention are tied to the moving-plate frame of reference. Pre- and post-multiplication of the estimated covariances by their associated best-fitting rotation $\hat{A}$ and its inverse $\hat{A}^T$ transforms the covariances from the moving to the fixed plate. Proper transformation of these covariances using eq. (2) requires consideration of which plate was fixed during the inversion. The second type of rotation covariances used herein was determined using a data-based boot-strapping method (Merkouriev & DeMets 2006). These covariances are invariant with respect to the fixed or moving plate and can thus be transformed by eq. (2) without consideration of the geographic framework of the covariances. Finally, we also use rotation covariances estimated with the REDBACK Bayesian algorithm (Section 3.3 and Iaffaldano *et al.* 2012, 2014). The REDBACK covariances are independent of the plate that is fixed during the analysis and can be transformed by eq. (2) without consideration of the geographic framework of the covariances.

Stage rotations that describe plate motion from time t_2 to t_1 were determined using the standard method, that is, given finite rotations $\hat{A}_{t_2}$ and $\hat{A}_{t_1}$ that reconstruct Plate B onto Plate A for times t_2 and t_1, the stage rotation $\hat{A}_{t_2\rightarrow t_1}$ that reconstructs the motion of Plate B relative to Plate A from t_2 to t_1 is given by $\hat{A}_{t_1}\hat{A}_{t_2}^T$. If the covariances for both finite rotations are expressed in a common frame of reference, the stage rotation covariances equal the sum of the covariances for $\hat{A}_{t_2}$ and $\hat{A}_{t_1}$. The stage rotations and their covariances vary depending on whether they are tied to Plate A or B in the above example and should thus be expressed relative to the same plate, most commonly that of the stationary plate (Plate A in the generic example above). The finite rotation covariances that express uncertainties in the movement of the Pacific plate when rotated into a North America frame of reference using eq. (2) are by convention tied to the moving Pacific plate. We therefore transformed those covariances to the North America plate frame of reference prior to estimating Pacific-relative-to-North America stage rotations and their covariances. All stage angular velocities and covariances were determined from their corresponding stage rotations by dividing the stage rotation angles by the stage time span and the stage rotation covariances by the square of the stage time span.

3.2 Rotation interpolations and geomagnetic reversal time scale

Minor interpolations of several Pacific–Antarctic and Antarctic–Nubia rotations were required in order to combine them with the Nubia–North America rotations. Following the method described by Doubrovine & Tarduno (2008), given finite rotations $\hat{A}_{t_2}$ and $\hat{A}_{t_1}$ for times t_2 and t_1, both expressed in a common frame of reference, we interpolated to times t intermediate in age between t_2 and t_1 via $\hat{A}_t = (\hat{A}_{t\rightarrow t_1})(\hat{A}_{t_1})$, where the stage rotation matrix $\hat{A}_{t\rightarrow t_1}$ is the product of the scalar $(t - t_1)/(t_2 - t_1)$ and $\hat{A}_{t_2\rightarrow t_1}$. This method

presumes constant plate motion from time t_2 to t_1. Given that only one of our interpolations spans an interval longer than 0.2 Myr, we consider the constant-motion approximation to be adequate.

Rotation interpolations and the derivation of stage angular velocities both require estimates of magnetic reversal ages. We use magnetic reversal ages from the astronomically tuned GTS12 time scale (Hilgen *et al.* 2012; Ogg 2012). The GTS12 reversal ages are the same as those used by DeMets *et al.* (2015a,b) for the Nubia–Antarctic and Nubia–North America rotations, but differ from those used by Croon *et al.* (2008). All ages assigned herein to the Croon *et al.* rotations are from GTS12.

3.3 Noise-reduction methodology

An important aspect of our analysis is to minimize noise in the plate circuit rotations given that the noise in those rotations will propagate into the Pacific–North America rotations and will be further accentuated when the finite rotations are differentiated to estimate stage rotations. Noise in closely spaced finite rotations such as those employed herein can give rise to erratic, short-duration variations in estimated plate velocities that are both kinematically and geodynamically implausible (Iaffaldano *et al.* 2012).

Methods for reducing noise in rotations include a spline smoothing algorithm described by Hanna & Chang (2000) and a trans-dimensional, hierarchical Bayesian method described by Iaffaldano *et al.* (2014). In the latter method, millions of candidate finite rotation sequences are first generated from a time series of starting finite rotations via a Monte Carlo algorithm. Each candidate rotation sequence is then assigned a probability of being a faithful realization of the true finite rotation sequence based on its distance from the starting rotations. The most representative rotation sequence, which we refer to hereafter as the noise-reduced rotations, is defined as the weighted average of the candidate estimates. Nominal covariances in the noise-reduced finite rotations are estimated from the range of candidate models that satisfy the algorithm's acceptability criteria. Covariances in noise-reduced stage angular velocities derived from the finite rotations are estimated separately based on the same acceptability criteria and are thus not propagated from the finite rotation covariances.

Iaffaldano *et al.* (2014) implement this algorithm in their openly available REDBACK software, which estimates noise-reduced finite rotations and stage angular velocities given a starting sequence of noisy rotations, and also identifies the time or times when changes in plate motion are most likely to have occurred. DeMets *et al.* (2015a,b) use REDBACK to estimate noise-reduced rotations and angular velocities for the Nubia–North America and Antarctic–Nubia plate pairs. In Section 4, we similarly use REDBACK to estimate Pacific–Antarctic noise-reduced rotations and angular velocities.

3.4 Corrections for outward displacement

Near-bottom surveys of magnetic reversal polarity transition zones along the mid-ocean ridges show that the midpoints of magnetic reversals are shifted away from the ridge axis by 1 km or more with respect to the idealized location of the reversal (e.g. Atwater & Mudie 1973; Sempere *et al.* 1987). Plate kinematic reconstructions of young magnetic reversals along well-surveyed segments of the mid-ocean ridges corroborate this result and indicate that the net outward bias ranges from 1 to 5 km and averages 2 km globally (DeMets & Wilson 2008). Estimates of recent seafloor spreading

rates that fail to correct for this bias may be as much as 40 per cent too high along parts of the mid-ocean ridge system (Merkouriev & DeMets 2008).

All of the finite rotations used herein are corrected for outward displacement. Merkouriev & DeMets (2014) estimate and apply a 1-km correction for the Nubia–North America plate pair. For the Nubia–Antarctic plate pair, DeMets *et al.* (2015b) estimate and apply a 5-km correction. Herein, we correct all of the Croon *et al.* (2008) Pacific–Antarctic rotations for 2 km of outward displacement based on evidence for 1–3 km of outward displacement along the Pacific–Antarctic Rise (DeMets & Wilson 2008). Details are given in Section 4.1.

4 RESULTS: BEST-FITTING AND NOISE-REDUCED ROTATIONS

4.1 Pacific–Antarctic plate motion

We determined noise-reduced rotations from Croon *et al.*'s (2008) best-fitting Pacific–Antarctic rotations in three stages. We first interpolated the best-fitting rotations from table 1 of their paper to the same 21 magnetic reversal tie points as for the Nubia–North America rotations. No interpolation spanned an interval longer than 0.2 Myr. We then corrected all of the rotations for 2 km of ridge-normal outward displacement by adding to each finite rotation a small-angle counter-rotation of 0.02 angular degrees about a pole located at 28.6°N, 108.2°W. In order to better constrain the noise-reduced rotations at the older end of our desired rotation sequence, we included Croon *et al.*'s rotations for C6An.2 (20.57 Ma) and C6Bn2 (22.27 Ma), suitably corrected for outward displacement. Finally, we applied REDBACK software (Iaffaldano *et al.* 2014) to the resulting sequence of best-fitting rotations.

Tables 2 and 3 list the noise-reduced finite rotations and stage angular velocities, respectively, from the REDBACK analysis. The noise-reduced finite poles migrate northwards through time (Fig. 4a), but without the erratic changes in location exhibited by the best-fitting poles (Figs 4a and b). The REDBACK analysis suggests that the stage pole location and angular rotation rate both changed significantly at 16–14 Ma (Supporting Information Fig. S3) and that the stage pole moved again at ∼8 Ma, consistent with changes in the estimated stage rates and directions at those times (Fig. 4).

Pacific–Antarctic spreading rates estimated with the noise-reduced stage angular velocities increase slowly after ≈17 Ma and then accelerate more rapidly after ≈8 Ma at both ends of the Pacific–Antarctic Rise (solid lines in Fig. 5a), similar to changes in the noisier, best-fitting stage rates (circles in Fig. 5a). Gradual clockwise rotations of the noise-reduced and best-fitting slip directions along a Pacific plate flow line that originates at the Pitman fracture zone began at ≈13 Ma and have reached 18° at present (Fig. 5b). These agree with gradual clockwise changes since 13 Ma that are described by Cande *et al.* (1995) and are also consistent with a geodetically derived slip direction (grey bars in Fig. 5b). Slip directions along the Menard fracture zone flow line have changed (clockwise) by only 2°–3° clockwise since 13 Ma (Fig. 5b), reflecting its greater distance from the Pacific–Antarctic pole of rotation.

4.2 Nubia–North America and Nubia–Antarctic plate motions

No modifications to the 21 best-fitting and noise-reduced rotations for the Nubia–North America plate pair (Merkouriev & DeMets

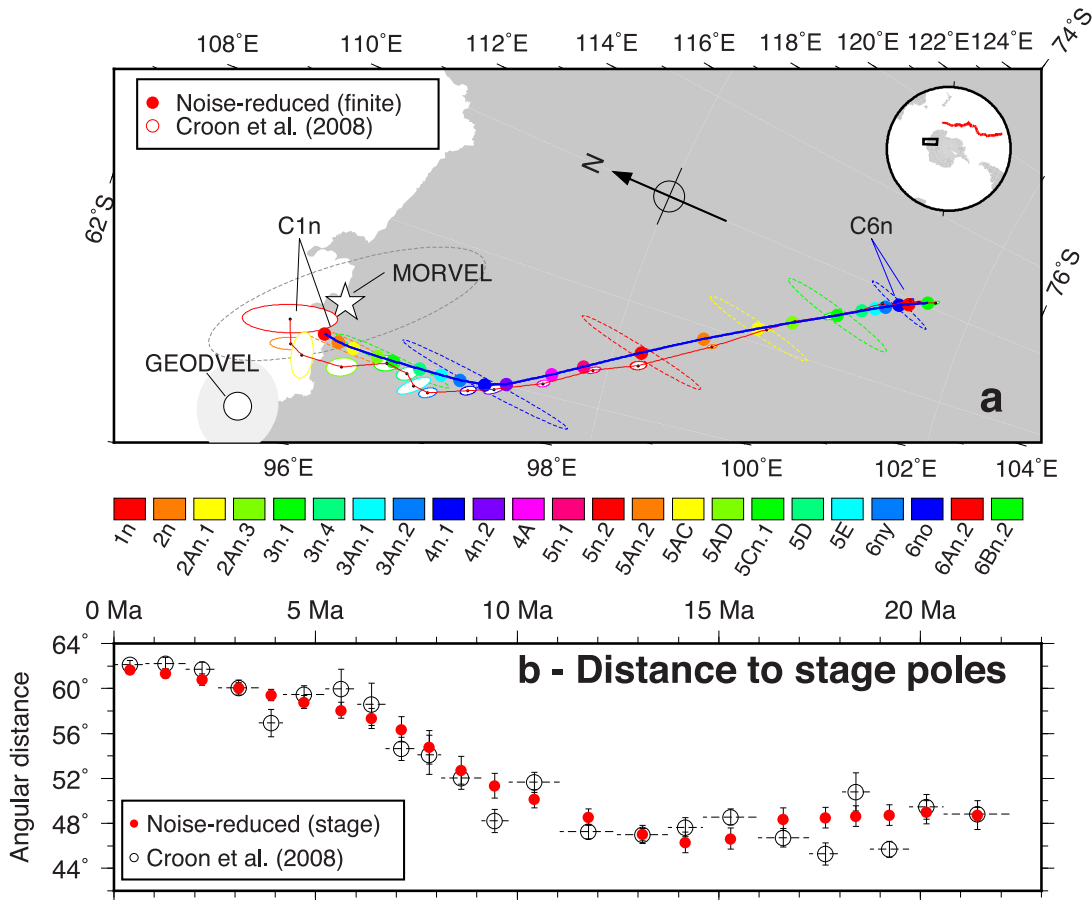**Table 2.** Pacific–Antarctic noise-reduced finite rotations.

Chron	Age[a] (Ma)	Lat. (°N)	Long. (°E)	Ω (deg.)	Covariances					
					a	b	c	d	e	f
1n(o)	0.781	65.72	− 79.78	0.667	0.3	− 0.9	0.0	2.4	0.5	5.3
2n(y)	1.778	65.95	− 79.95	1.523	1.2	− 3.1	0.3	8.1	0.0	8.9
2An.1(y)	2.581	66.20	− 80.04	2.212	2.3	− 6.1	0.8	16.2	− 0.8	13.5
2An.3(o)	3.596	66.58	− 80.11	3.086	5.1	− 13.2	1.9	34.6	− 2.9	23.2
3n.1(y)	4.187	66.82	− 80.14	3.596	8.0	− 20.5	3.1	52.8	− 4.8	33.9
3n.4(o)	5.235	67.24	− 80.18	4.497	17.4	− 43.2	7.3	108.4	− 13.4	54.1
3An.1(y)	6.033	67.57	− 80.21	5.179	30.1	− 73.5	13.7	181.0	− 28.3	61.6
3An.2(o)	6.733	67.87	− 80.22	5.777	47.1	− 113.5	22.2	275.5	− 47.7	72.1
4n.1(y)	7.528	68.25	− 80.16	6.456	74.5	− 176.6	35.9	421.2	− 78.0	90.0
4n.2(o)	8.108	68.57	− 79.92	6.951	93.9	− 218.3	45.5	511.0	− 97.7	103.6
4A(o)	9.105	69.20	− 79.06	7.802	111.9	− 244.9	53.8	539.3	− 106.8	126.9
5n.1(y)	9.786	69.63	− 78.37	8.387	117.1	− 244.8	55.5	515.3	− 103.2	140.6
5n.2(o)	11.056	70.42	− 77.07	9.478	120.2	− 232.5	54.8	453.6	− 88.6	168.1
5An.2(o)	12.474	71.27	− 75.60	10.700	122.4	− 220.5	51.9	401.9	− 69.6	205.9
5AC(y)	13.739	72.01	− 74.29	11.792	148.7	− 253.0	59.9	436.0	− 69.8	259.4
5AD(o)	14.609	72.48	− 73.43	12.542	192.1	− 311.4	77.6	511.6	− 85.8	311.3
5Cn.1(y)	15.974	73.08	− 72.28	13.719	270.2	− 405.4	108.7	617.8	− 107.6	407.0
5D(y)	17.235	73.41	− 71.58	14.744	247.9	− 353.2	100.4	511.6	− 95.4	340.5
5E(y)	18.056	73.59	− 71.19	15.385	233.7	− 320.8	101.3	446.3	− 104.8	252.6
6ny(y)	18.748	73.73	− 70.89	15.927	218.4	− 290.9	99.3	392.2	− 107.6	192.0
6no(o)	19.722	73.91	− 70.53	16.689	182.6	− 235.1	87.5	306.1	− 98.8	122.6
6An.2(o)	20.574	74.05	− 70.27	17.357	118.0	− 151.2	57.8	196.6	− 66.8	69.8
6Bn.2(o)	22.268	74.31	− 69.79	18.684	71.0	− 85.7	35.9	104.0	− 40.7	32.8

[a]Reversal ages are from Ogg (2012) and are applied throughout the analysis. '(o)' and '(y)' indicate old and young edges of the magnetic reversal, respectively. The noise-reduced rotations reconstruct the Pacific plate onto the Antarctic plate. Rotation angles Ω are positive CCW. See the text for the method used to derive the rotations and their covariances. The Bayesian-estimated covariances, which have units of 10^{-8} radians^2, approximate the range of acceptable rotations that were explored by the REDBACK software.

Table 3. Pacific–Antarctic noise-reduced stage angular velocities.

Age(o) (Ma)	Age(y) (Ma)	Lat. (°N)	Long. (°E)	$\dot\omega$ (° Myr^{-1})	Covariances					
					a	b	c	d	e	f
0.781	0.000	65.72	− 79.75	0.857	0.68	− 0.08	0.20	1.39	− 1.02	3.21
1.778	0.781	66.12	− 80.05	0.858	0.52	0.07	0.15	1.92	− 0.07	2.00
2.581	1.778	66.73	− 80.18	0.859	0.66	0.29	0.24	2.86	0.27	2.28
3.596	2.581	67.54	− 80.18	0.861	0.87	0.39	0.37	2.87	− 0.41	3.56
4.187	3.596	68.26	− 80.16	0.865	1.34	0.40	1.06	4.91	− 3.68	12.01
5.235	4.187	68.93	− 80.15	0.861	1.81	0.98	0.58	4.39	− 0.22	4.68
6.033	5.235	69.74	− 80.10	0.855	2.59	1.34	0.78	6.50	− 0.22	6.48
6.733	6.033	70.49	− 79.93	0.855	3.53	1.77	0.75	9.21	1.37	5.87
7.528	6.733	71.43	− 78.94	0.855	5.62	2.65	0.93	14.19	3.26	6.61
8.108	7.528	72.60	− 75.09	0.855	11.06	4.63	1.84	26.88	5.53	13.74
9.105	8.108	73.83	− 68.48	0.859	5.85	1.25	0.74	18.95	4.26	9.49
9.786	9.105	74.69	− 64.35	0.864	4.06	1.02	0.67	17.30	4.36	7.18
11.056	9.786	75.51	− 61.05	0.867	3.00	1.17	0.61	11.79	2.90	4.54
12.474	11.056	76.65	− 56.19	0.870	3.39	2.04	0.90	13.74	2.98	5.32
13.739	12.474	77.70	− 51.23	0.873	3.94	2.31	1.05	19.24	3.96	7.21
14.609	13.739	78.20	− 48.72	0.873	4.57	2.97	1.31	29.71	6.56	9.29
15.974	14.609	78.08	− 50.39	0.870	4.40	3.19	1.34	32.89	7.44	9.05
17.235	15.974	77.03	− 56.66	0.816	5.30	5.91	2.58	32.75	4.69	15.93
18.056	17.235	76.97	− 57.37	0.784	4.99	6.05	2.94	28.26	2.17	18.79
18.748	18.056	76.95	− 58.03	0.785	4.55	5.36	2.45	25.87	2.64	15.25
19.722	18.748	76.97	− 58.78	0.785	3.81	4.05	2.05	22.52	2.29	13.76
20.574	19.722	76.90	− 60.10	0.785	4.70	4.29	2.04	25.25	2.99	14.05
22.268	20.574	77.16	− 59.54	0.785	6.65	6.02	2.35	37.96	6.10	15.28

Interval angular velocities for Antarctic relative to Pacific plate motion in a frame of reference tied to the Pacific plate for the time period specified in the first two columns as determined from the REDBACK noise-reduction software (Iaffaldano *et al.* 2014). The angular rotation rates $\dot\omega$ are positive anticlockwise for the old to the young limit of each time interval. The angular velocity covariances are estimated by REDBACK from the range of angular velocities that satisfy a probability criteria that the angular velocity is a realization of its true value. The Cartesian covariances have units of 10^{-8} radians^2 Myr^{-2}. The footnotes for Table 1 provide further information about the covariances.

Figure 4. Post-23 Ma Pacific–Antarctic finite pole locations (a) and stage pole movement (b). (a) Best-fitting Pacific–Antarctic finite rotation poles from Croon *et al.* (2008) (open circles) and noise-reduced poles (solid circles) estimated in this study (Table 2), with selected 2D 95 per cent confidence regions, Chrons 1n to 6Bn.2. Most uncertainty ellipses are omitted for clarity. Star and dotted line show the 3-Myr-average MORVEL Pacific–Antarctic pole and its 95 per cent confidence ellipse (DeMets *et al.* 2010) and large circle and shaded ellipse indicate the pole and 95 per cent confidence ellipse for the GEODVEL Pacific–Antarctic geodetic angular velocity (Argus *et al.* 2010). The map is a stereographic projection that is centred on 69°S, 180°W. The circular inset map shows the location of the area encompassed by panel (a) (rectangle) relative to the Pacific–Antarctic Rise (red line). (b) Angular distance from the Pacific–Antarctic stage poles in Table 3 to a reference point at the Menard fracture zone. Changes in the pole-to-boundary distance from one interval to the next are significantly smaller for the noise-reduced stage poles than for the best-fitting stage poles, implying a smoother evolution of the plate motion for the former. The horizontal dotted lines show the intervals that are spanned by each stage pole.

2014; DeMets *et al.* 2015a) were made for this analysis. The noise-reduced rotations constitute our preferred estimates for the analysis below given that they provide a simpler description of Nubia–North America motion since 20 Ma without significantly degrading the fit to their underlying plate kinematic data (DeMets *et al.* 2015a).

The best-fitting and noise-reduced Nubia–Antarctica rotations estimated by DeMets *et al.* (2015b) sample 19 of the 21 times that are represented in the Nubia–North America rotations, but exclude Chrons 5D (17.24 Ma) and 5E (18.06 Ma), for which too few data were available to estimate rotations. We thus interpolated rotations for both of these times from the next youngest and oldest rotations, those for Chrons 5Cn.3 (16.72 Ma) and 6ny (18.75 Ma). As noted by DeMets *et al.* (2015b), relatively few reliable identifications of Chron 6 are available from the sparsely surveyed, older seafloor along the Nubia–Antarctica plate boundary. The Nubia–Antarctic rotations for times older than Chron 5Cn.3 (16.72 Ma) are thus less reliable than are the other circuit rotations used for this analysis. The potential inaccuracies in our estimates of Pacific–North America plate motion for times before 16.7 Ma are thus larger than for the past 16.7 Myr. No significant fitting penalty to the data from the Southwest Indian Ridge is associated with the noise-reduced

rotations (DeMets *et al.* 2015b). We thus adopt them as our preferred estimates below.

4.3 Pacific–North America rotations and angular velocities

4.3.1 Rotations determined from best-fitting circuit rotations

Table 4 lists the Pacific–North America finite rotations that we determined by applying Equation 1 to the best-fitting plate circuit rotations described above. Covariances tied to the Pacific plate frame of reference were first determined using Equation 2 and were then transformed to the North America reference frame as a basis for estimating Pacific–North America stage angular velocities. Supporting Information Table S1 lists the best-fitting rotations that reconstruct the North America plate onto the Pacific plate and their associated covariances, which are tied to the Pacific plate.

In order to improve the signal-to-noise ratio in the stage angular velocities that we determined from the noisy best-fitting rotations, we estimated stage angular velocities that span overlapping, ≈2-Myr-long intervals, which is longer than the maximum temporal
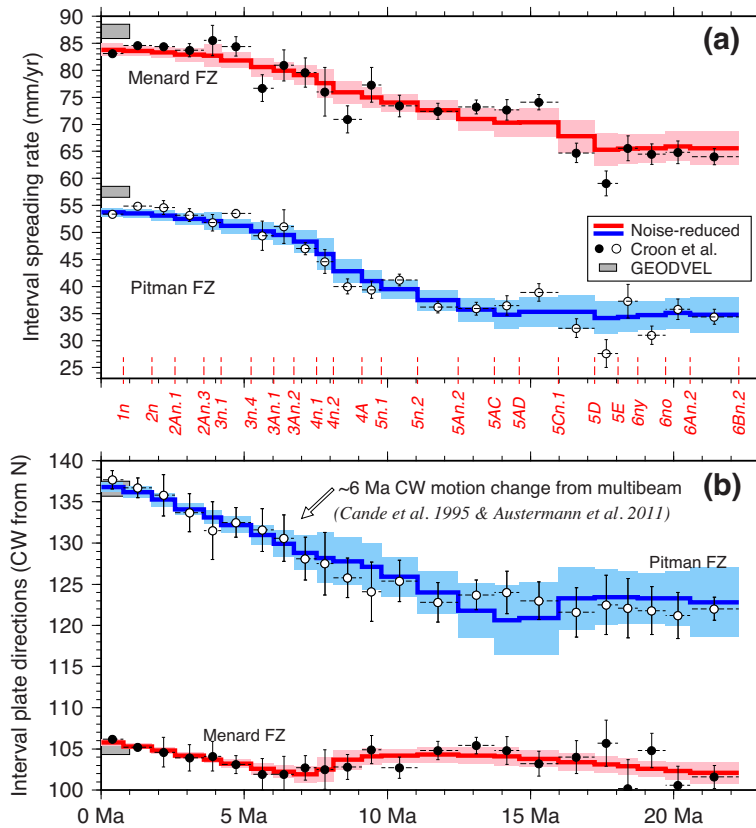
Figure 5. Pacific–Antarctica seafloor spreading rates (a) and plate slip directions (b) for time intervals shown by horizontal dashed lines. The noise-reduced angular velocities in Table 3 and angular velocities derived from the Croon *et al.* (2008) best-fitting finite rotations adjusted for 2 km of outward displacement are used to estimate motion along Pacific plate flow lines that originate at the Menard (49.7°S, 113.8°W) and Pitman fracture zones (64.5°S, 170.8°E), as indicated in the legend. One-sigma uncertainties shown by the vertical bars and shaded areas are propagated from the angular velocity covariances. Grey bars show opening rates and directions with their 1σ uncertainties estimated with the GEODVEL Pacific–Antarctic angular velocity (Argus *et al.* 2010). The interval velocities and uncertainties are determined in a Pacific plate reference frame.

Table 4. Pacific–North America best-fitting finite rotations and rotation covariances.

Chron	Age (Myr)	Lat. (°N)	Long. (°E)	Ω (deg.)	Covariances a	b	c	d	e	f
1n	0.781	48.03	286.79	0.553	1.5	−0.6	−0.4	1.0	0.8	1.5
2n	1.778	48.71	286.20	1.280	7.2	2.0	−9.2	1.7	−1.5	19.4
2An.1	2.581	48.29	286.78	1.821	8.9	1.3	−6.1	1.9	0.0	14.8
2An.3	3.596	48.27	288.52	2.593	19.1	5.6	−16.7	4.7	−2.9	33.2
3n.1	4.187	48.88	288.35	2.985	24.7	7.9	−23.3	6.1	−3.6	47.0
3n.4	5.235	50.11	287.64	3.773	31.4	8.3	−27.8	5.7	−5.9	51.3
3An.1	6.033	50.61	286.95	4.340	27.3	5.4	−20.6	6.6	0.6	49.5
3An.2	6.733	51.14	286.20	4.873	34.5	5.1	−33.8	4.5	−5.2	63.3
4n.1	7.528	51.35	287.28	5.360	45.1	8.8	−43.5	6.9	−10.0	72.8
4n.2	8.108	51.70	287.53	5.779	46.1	6.2	−44.7	9.6	−10.0	90.1
4A	9.105	51.46	289.02	6.278	77.0	7.8	−70.4	13.6	−19.9	100.9
5n.1	9.786	51.42	291.17	7.033	103.3	30.0	−95.0	18.9	−34.3	130.4
5n.2	11.056	52.86	290.12	7.729	31.5	5.7	−28.7	8.3	−4.2	57.3
5An.2	12.474	53.48	291.50	8.671	32.7	5.5	−37.7	6.7	−10.1	63.8
5AC	13.739	53.74	292.72	9.503	29.5	4.1	−23.1	5.9	−5.2	40.4
5AD	14.609	53.62	293.18	10.061	42.2	6.2	−36.2	7.7	−6.9	54.0
5Cn.1	15.974	54.10	293.49	10.688	241.0	29.6	−255.3	36.0	−65.8	375.1
5D	17.235	54.46	293.47	11.392	244.1	26.6	−256.6	33.0	−65.6	370.3
5E	18.056	54.60	293.50	11.799	241.5	27.2	−257.6	34.7	−63.6	370.4
6ny	18.748	54.38	293.33	12.219	505.8	−19.5	−318.4	35.0	3.2	270.7
6no	19.722	56.65	289.71	12.864	91.4	25.4	−50.2	45.2	−6.0	84.8

These rotations, which reconstruct the Pacific plate onto the North America plate, were determined using eq. (1) in the text. The rotation angles Ω are positive anticlockwise. The rotations and their covariances are determined from the North America–Nubia, Nubia–Antarctic and Antarctic–Pacific best-fitting rotations using methods described in the text. The covariances, which have units of 10^{-8} radians^2, are tied to the North America plate.
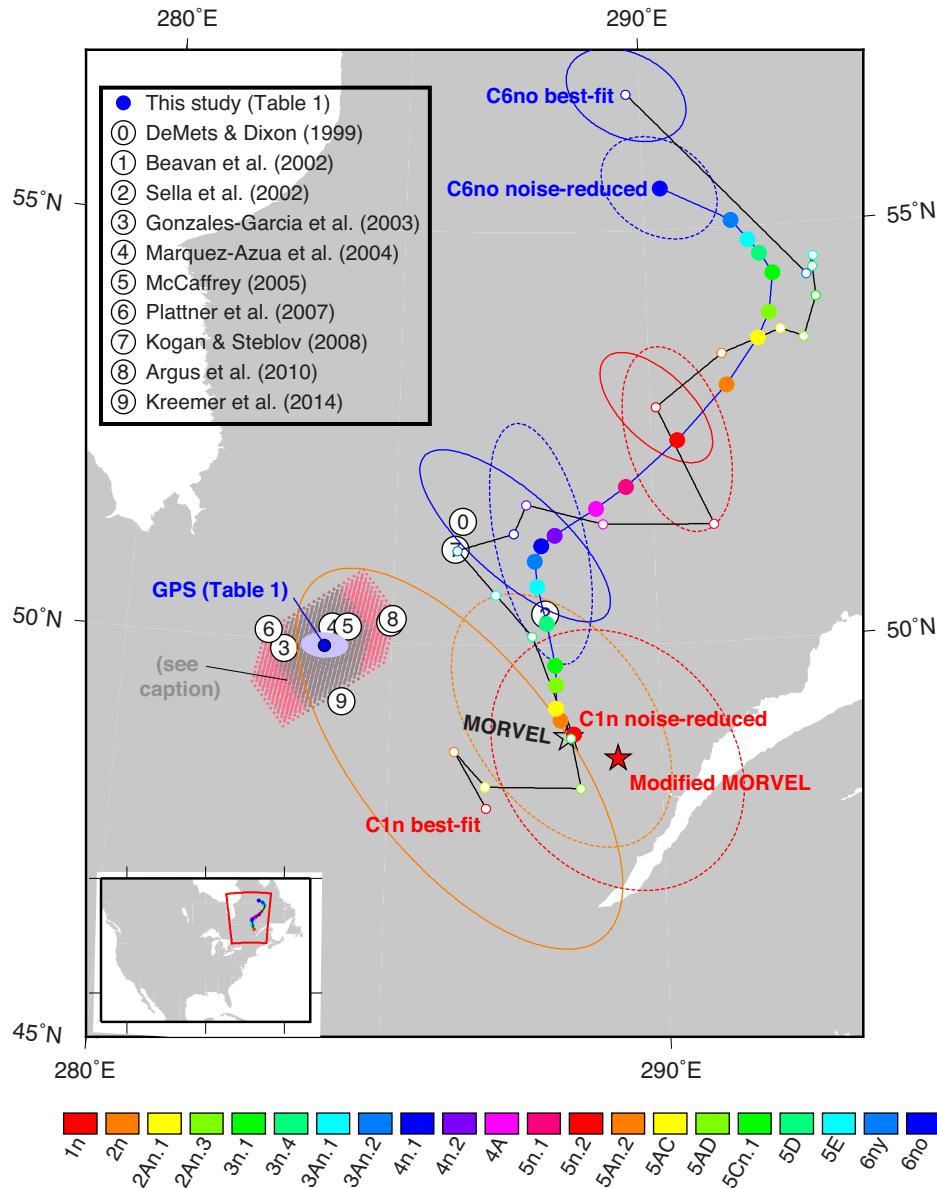
Figure 6. Pacific–North America best-fitting and noise-reduced poles and selected, 2-D, 95 per cent confidence regions and previous studies. The open and solid circles show the best-fitting and noise-reduced finite rotation poles respectively from Tables 4 and 5. The pole we determined from the modified MORVEL plate motion data (Section 5.1.1) is located ∼70 km southeast of the MORVEL pole (open black star). Geodetic poles are located by circled numerals identified in the legend. The grey- and pink-shaded regions show the distribution of alternative geodetic poles derived by relaxing the stationary geocentre assumption in ITRF2008 (Section 5.1.2). The confidence regions shown by solid and dashed lines are for the best-fitting and noise-reduced poles, respectively.

resolution of the closely spaced finite rotations. Given that angular velocities that span intervals longer than the maximum temporal resolution of the underlying rotation sequence may not accurately depict the plate motion (Iaffaldano *et al.* 2014), we do not tabulate the best-fitting angular velocities and instead use them solely for comparative purposes during the remainder of the analysis.

The best-fitting rotations and angular velocities reveal significant changes in Pacific–North America plate motion since 20 Ma. The best-fitting poles clearly migrate southwards from 19.7 Ma to the present (Fig. 6), albeit with erratic changes in the pole location from one time to the next. The southward pole migration is accompanied by a long-term, ≈20° clockwise rotation of the plate slip direction in western North America (grey circles in Fig. 7b). Implausible changes of 10° or more in the stage directions from one interval to the next are almost surely attributable to noise propagated from the

constituent best-fitting plate circuit rotations. The stage rates (grey circles in Fig. 7a) clearly suggest a significant speed-up in motion from 20–13 Ma and steady motion since 8 Ma, but vary erratically due to errors in the best-fitting circuit rotations.

4.3.2 Noise-reduced rotations, angular velocities and uncertainties

Table 5 lists the Pacific–North America finite rotations and co-variances determined by applying eqs (1) amd (2) to the noise-reduced plate circuit rotations described in the previous section, with the covariances once again tied to the North American plate. Angular velocities (Table 6) that we determined from these finite rotations sample the kinematic history at the maximum temporal
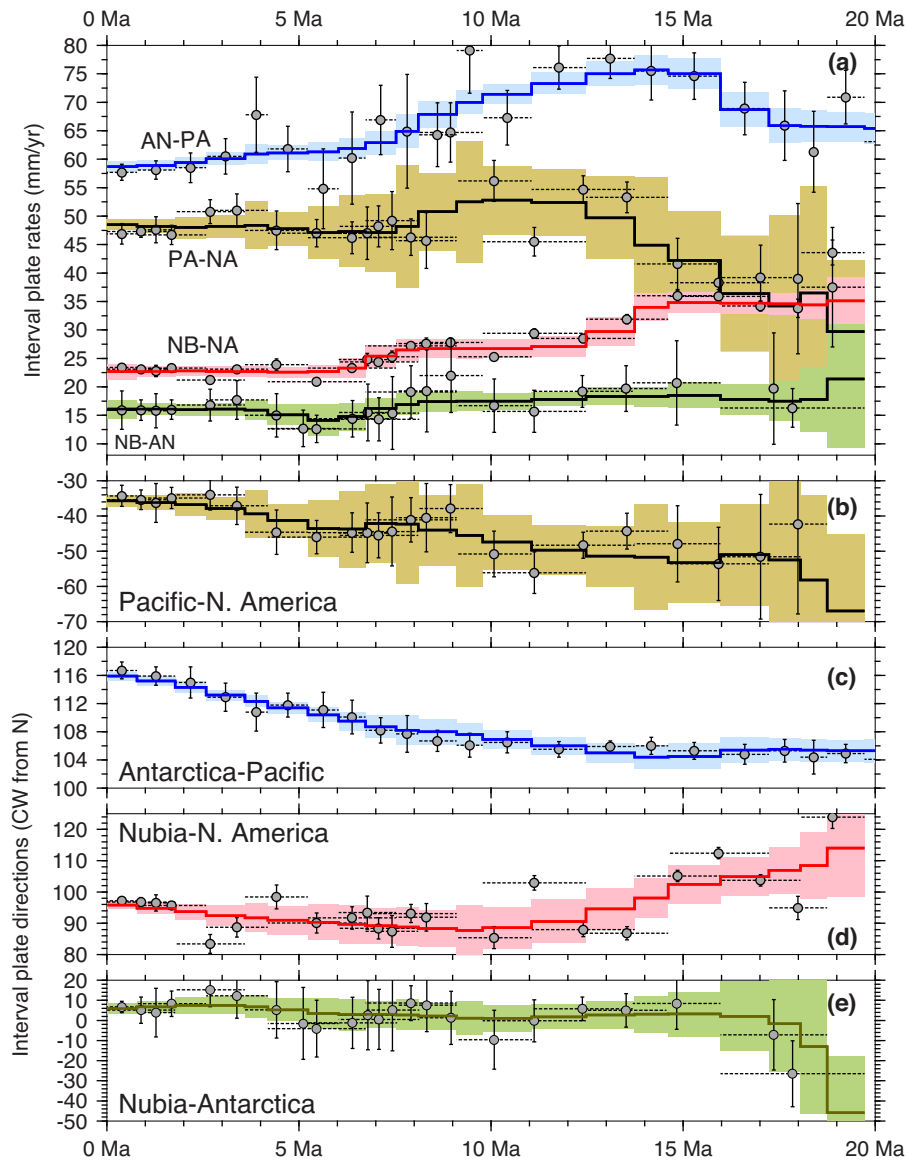
Figure 7. Interval motions since 20 Ma between the Antarctic (AN), Pacific (PA), North America (NA), and Nubia (NB) plates estimated with noise-reduced and best-fitting angular velocities for each plate pair at 36.0°N, 120.6°W on the San Andreas Fault. (a) Plate rates for time intervals shown by horizontal lines. Noise-reduced and best-fitting rates are shown by solid lines and circles, respectively. (b–e) Plate slip directions. Motions are for the first listed plate relative to the second. The Antarctic–Pacific and Pacific–North America noise-reduced interval velocities are estimated from the angular velocities in Tables 3 and 6, respectively.

resolution of the noise-reduced finite rotations, ranging from intervals as short as 0.58 Myr to intervals as long as 1.42 Myr. Hereafter, the noise-reduced rotations and angular velocities in Tables 5 and 6 are used as our preferred estimates of Pacific–North America plate motion.

Because the rotation covariances and angular velocity covariances that are estimated from the Bayesian analyses are not formal covariance estimates, they may not accurately convey the uncertainties that are imposed on the rotations by the underlying plate kinematic data. We thus used the scatter in the best-fitting finite and stage rotations to calibrate the Bayesian covariances so that they approximate rather than exceed the noise exhibited by the best-fitting rotations. On average, the scatter in the stage velocities estimated with the best-fitting stage rotations was only half as large as the velocity uncertainties that were propagated from the covariances initially estimated by REDBACK. The initial Bayesian uncertainty

estimates were thus implausibly large with respect to the noise in the best-fitting rotations. Scaling the Bayesian rotation covariances downwards by a factor of four gives rise to modified, 1σ velocity uncertainties that encompass roughly two-thirds of the scatter in the best-fitting stage velocities, as might be expected for covariances that approximate the 1σ uncertainties. All of the covariances in Tables 5 and 6 reflect this modification.

The noise-reduced rotations and angular velocities reproduce the first-order features of the best-fitting Pacific–North America kinematic history described in Section 4.3.1 and illustrated in Figs 6 and 7. The noise-reduced poles migrate southwards from 19.7 Ma to the present (Fig. 6), mimicking the best-fitting poles, but are more tightly clustered and describe a simpler path. The noise-reduced stage rates increase gradually between 20 and 13 Ma, similar to but less noisy than the change in the estimated best-fitting rates (Fig. 7a). During the past 8 Ma, the noise-reduced plate rates have varied by

Table 5. Pacific–North America noise-reduced finite rotations and rotation covariances.

Chron	Age (Myr)	Lat. (°N)	Long. (°E)	Ω (deg.)	Covariances					
					a	*b*	*c*	*d*	*e*	*f*
1n	0.781	48.92	288.40	0.558	2.9	− 0.1	− 1.8	1.6	0.1	2.8
2n	1.778	49.10	288.16	1.270	3.7	− 0.6	− 2.0	3.3	0.0	4.3
2An.1	2.581	49.24	288.08	1.841	4.7	− 1.2	− 2.1	5.7	− 0.3	6.3
2An.3	3.596	49.53	288.08	2.564	6.6	− 2.7	− 2.1	10.9	− 0.8	10.3
3n.1	4.187	49.76	288.07	2.987	8.3	− 4.4	− 2.1	15.9	− 1.3	14.1
3n.4	5.235	50.27	287.91	3.734	11.7	− 9.8	− 1.8	30.5	− 4.0	21.1
3An.1	6.033	50.71	287.74	4.298	16.3	− 17.7	− 1.4	49.6	− 7.8	25.2
3An.2	6.733	51.02	287.69	4.789	22.3	− 28.3	0.1	74.1	− 12.2	30.1
4n.1	7.528	51.21	287.81	5.334	30.0	− 44.4	4.7	110.7	− 19.4	35.4
4n.2	8.108	51.34	288.07	5.726	36.2	− 54.9	8.8	133.1	− 24.1	39.5
4A	9.105	51.65	288.88	6.398	44.0	− 61.3	13.6	140.3	− 26.4	47.5
5n.1	9.786	51.91	289.48	6.860	49.5	− 60.9	16.2	134.9	− 26.0	54.2
5n.2	11.056	52.45	290.53	7.713	57.4	− 56.9	18.7	120.5	− 24.6	69.0
5An.2	12.474	53.10	291.55	8.648	66.4	− 53.3	20.0	109.0	− 23.9	89.8
5AC	13.739	53.65	292.25	9.440	85.8	− 61.3	27.6	118.8	− 27.0	111.3
5AD	14.609	53.95	292.51	9.947	111.1	− 78.9	42.7	138.7	− 30.5	125.4
5Cn.1	15.974	54.42	292.63	10.720	142.7	− 110.2	62.3	169.3	− 33.5	150.6
5D	17.235	54.67	292.39	11.385	147.0	− 99.3	71.8	147.5	− 27.1	139.8
5E	18.056	54.84	292.17	11.802	151.7	− 90.4	81.3	134.0	− 28.2	123.8
6ny	18.748	55.08	291.84	12.191	160.9	− 85.5	93.1	124.5	− 32.6	118.1
6no	19.722	55.51	290.37	12.786	148.3	− 87.7	92.7	116.9	− 51.9	111.3

These rotations reconstruct the Pacific plate onto the North America plate. Rotation angles Ω are positive anticlockwise. The rotations and covariances were determined from the North AmericaNubia, NubiaAntarctic and AntarcticPacific noise-reduced rotations and covariances using eqs (1) and (2) from the text. The covariances have units of 10^{-8} radians^2 and express the uncertainties in the positions of Pacific plate points reconstructed onto North America.

Table 6. Pacific–North America noise-reduced stage angular velocities.

Age(o) (Ma)	Age(y) (Ma)	Lat. (°N)	Long. (°E)	$\dot{\omega}$ (° Myr^{-1})	Covariances					
					a	*b*	*c*	*d*	*e*	*f*
0.781	0.00	48.92	288.40	− 0.714	0.47	− 0.02	− 0.30	0.26	0.02	0.46
1.778	0.781	49.23	287.97	− 0.714	0.66	− 0.07	− 0.39	0.49	0.01	0.71
2.581	1.778	49.56	287.91	− 0.711	1.31	− 0.27	− 0.64	1.40	− 0.05	1.64
3.596	2.581	50.25	288.05	− 0.712	1.12	− 0.38	− 0.41	1.60	− 0.11	1.60
4.187	3.596	51.16	287.92	− 0.716	4.40	− 2.08	− 1.24	7.60	− 0.66	6.93
5.235	4.187	52.29	287.13	− 0.713	1.90	− 1.34	− 0.37	4.16	− 0.51	3.18
6.033	5.235	53.61	286.31	− 0.708	4.70	− 4.51	− 0.52	12.31	− 1.93	7.22
6.733	6.033	53.74	287.09	− 0.702	8.58	− 9.84	− 0.25	24.62	− 4.23	11.22
7.528	6.733	52.84	288.80	− 0.686	9.16	− 12.12	0.83	28.39	− 5.14	10.35
8.108	7.528	53.14	291.62	− 0.677	21.88	− 31.09	4.23	70.23	− 13.20	22.31
9.105	8.108	54.36	296.00	− 0.677	8.91	− 12.25	2.33	26.60	− 5.18	8.81
9.786	9.105	55.45	298.10	− 0.683	22.10	− 27.48	6.61	57.19	− 11.53	22.14
11.056	9.786	56.77	299.39	− 0.677	7.15	− 7.54	2.19	15.22	− 3.22	7.72
12.474	11.056	58.44	300.61	− 0.665	6.59	− 5.59	1.90	10.91	− 2.50	7.98
13.739	12.474	59.64	300.15	− 0.632	10.16	− 7.23	2.94	13.42	− 3.30	12.74
14.609	13.739	59.68	297.24	− 0.586	27.78	− 18.56	9.31	31.54	− 7.78	31.99
15.974	14.609	60.50	293.42	− 0.570	14.66	− 10.12	5.65	15.01	− 3.52	15.30
17.235	15.974	58.31	287.35	− 0.529	19.18	− 12.99	8.49	18.18	− 3.77	19.03
18.056	17.235	58.86	284.44	− 0.511	45.95	− 27.38	23.18	37.85	− 7.66	41.38
18.748	18.056	61.19	278.49	− 0.570	66.65	− 35.09	37.54	48.76	− 11.34	54.39
19.722	18.748	57.44	256.86	− 0.646	33.35	− 17.25	20.47	22.84	− 8.19	26.04

Pacific with respect to North America plate angular velocities for the time period given in the first two columns. The angular rotation rates $\dot{\omega}$ are positive anticlockwise for the old to the young limit of each time interval. The angular velocities and their Cartesian covariances are in a North America plate reference frame and are derived from the finite rotations given in Table 5. The covariances have units of 10^{-7} radians^2 Myr^{-2}. Refer to Table 1 footnotes for further information about the covariances.

less than 5 per cent and exhibit none of the erratic variations that characterize the best-fitting estimates (Fig. 7a).

5 IMPLICATIONS

We now evaluate the implications of the new Pacific–North America rotations and angular velocities for the post-20-Ma tectonic evolu-tion of the Pacific–North America plate boundary. Comparisons to plate velocities estimated with rotations estimated by previous authors are found throughout.

5.1 Plate motion from 4 Ma to present

Previous efforts to determine whether Pacific–North America plate motion has remained steady or changed during the past few Myr
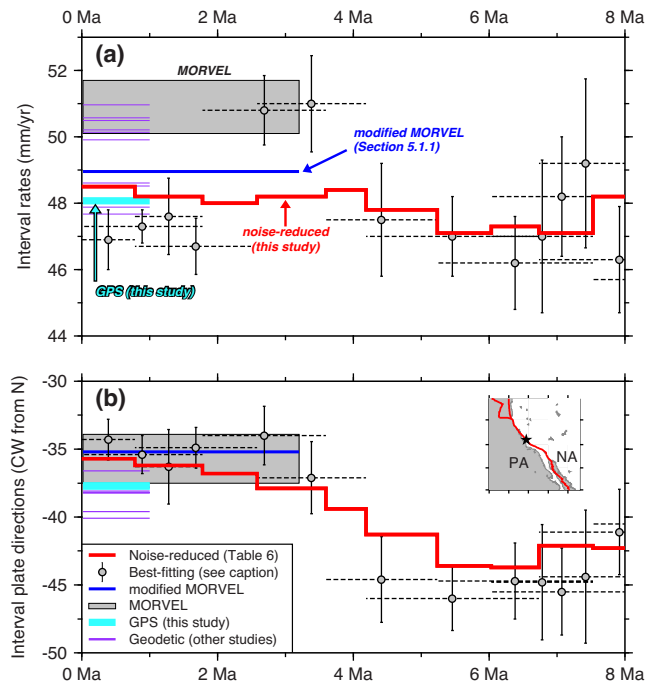
Figure 8. Pacific–North America interval rates (a) and slip directions (b) since 8 Ma estimated at 36.0°N, 120.6°W along the San Andreas Fault of central California (star in inset map). The best-fitting interval velocities were derived from finite rotations in Table 4 as described in Section 4.3.1. Other sources for the interval velocities are listed in the legend. Horizontal dashed lines show the time intervals spanned by the best-fitting interval rates and directions. Where shown, the uncertainties are 1σ and are propagated from the angular velocity covariances. Some uncertainties are omitted for clarity. The sources of the geodetic angular velocities used to estimate some of the linear velocities are found in the legend to Fig. 6.

were hindered by the lack of closely spaced reconstructions based on the global plate circuit (e.g. DeMets *et al.* 1987; Minster & Jordan 1987; DeMets & Dixon 1999; Argus & Gordon 2001). We thus begin by evaluating the steadiness of Pacific–North America plate motion during the past 4.2 Myr using our newly estimated geodetic angular velocity (Table 1) and the finite rotations and angular velocities from Tables 5 and 6. We also include the MORVEL angular velocity (DeMets *et al.* 2010), which averages plate motions over the past 1–3 Myr, and ten previously published geodetic angular velocities in the analysis.

5.1.1 Comparison to the MORVEL geological estimate

The MORVEL Pacific–North America angular velocity of DeMets *et al.* (2010) was determined using many of the same marine magnetic data and nearly the same plate circuit as is used herein, but via a different methodology. It is thus encouraging that the MORVEL Pacific–North America pole is located only 10 km from our newly estimated C1n pole (Fig. 6), well within the confidence regions of both poles. Their close proximity guarantees that the directions estimated with the two poles are nearly the same everywhere along the Pacific–North America plate boundary. For example, at a reference point along the San Andreas Fault, the MORVEL and C1n poles both suggest Pacific–North America slip directions of N35.7°W (Fig. 8b).

Given the close proximity of the C1n and MORVEL poles, their associated angular rotation rates can be compared directly to each

other as a measure of the consistency of the rates that are estimated with the two angular velocities. Surprisingly, their respective angular rotation rates, $0.750\pm0.007°$ Myr^{-1} and $0.714\pm0.009°$ Myr^{-1}, differ at the 95 per cent confidence level. Along the San Andreas Fault, the MORVEL angular velocity indicates a 50.9 ± 0.8 mm yr^{-1} slip rate (Fig. 8a), 2.4–2.9 mm yr^{-1} faster than the stage rates estimated with our noise-reduced angular velocities for the past 4.2 Myr. The discrepancy is puzzling given that all five of the newly estimated angular velocities for times since 4.2 Ma give rates (47.8–48.5 mm yr^{-1}) that are significantly slower than estimated with MORVEL. During the past 4.2 Ma, the newly estimated angular velocities suggest that the plate rate in western California has varied by less than 1 per cent from an average of 48.2 ± 0.25 mm yr^{-1} (red line in Fig. 8a).

We investigated the source of this discrepancy via a simple experiment with the plate kinematic data that were used to estimate the MORVEL angular velocities. Based on evidence presented by Merkouriev & DeMets (2014) that the azimuths of the Kane transform fault and fracture zone are anomalous with respect to the azimuths of other transform faults/fracture zones along the Nubia– North America plate boundary, we eliminated the azimuth of the Kane transform fault from the original MORVEL data. We further substituted five, well-determined Nubia–Antarctic seafloor spreading rates determined by DeMets *et al.* (2015b) from their analysis of closely spaced, Southwest Indian Ridge magnetic anomaly profiles for all of the Nubia–Antarctic opening rates in the original MORVEL data. This change is motivated by evidence described by DeMets *et al.* (2015b) that outward displacement along the Nubia– Antarctic segment of the ridge is 5 km rather than 2 km, as was assumed for the MORVEL analysis.

An inversion of the modified MORVEL observations, consisting of 1614 spreading rates, 170 transform fault azimuths, 56 earthquake slip directions, and 141 GPS site velocities that collectively constrain the relative movements of 25 plates, gives a revised Pacific–North America angular velocity of 48.6°N, 70.8°W, 0.712° Myr^{-1}. The revised angular velocity agrees with our noise-reduced angular velocities for times since 4.2 Ma (Table 6). For example, at the reference location on the San Andreas Fault, the rate estimated with the revised MORVEL angular velocity, 49.0 ± 0.8 mm yr^{-1}, differs insignificantly from the rates estimated with our noise-reduced angular velocities (compare blue and red lines in Fig. 8a). The revised pole location also differs insignificantly from that of the C1n pole (Fig. 6) and gives a direction insignificantly different from the directions estimated with our noise-reduced angular velocities (compare blue and red lines in Fig. 8b).

Two simple modifications to the MORVEL kinematic data thus reduce the difference between velocities that are estimated with our 0.78 Myr-to-present angular velocity (Table 6) and the MORVEL angular velocity to only 0.7 ± 0.8 mm yr^{-1}, 70 per cent less than the original 2.4 mm yr^{-1} difference (Fig. 9b). The evidence thus suggests that the original MORVEL estimate is biased by a small subset of the MORVEL plate kinematic data. We conclude that Pacific–North America plate motion during the past several million years is well described, barring further unforeseen systematic errors in the plate kinematic estimates.

5.1.2 Comparison to geodetic estimates

Based on the evidence cited above, we expect the following of geodetic estimates of Pacific–North America plate motion: (1) rates that are close to or the same as the 48.2 ± 0.25 mm yr^{-1} average rate
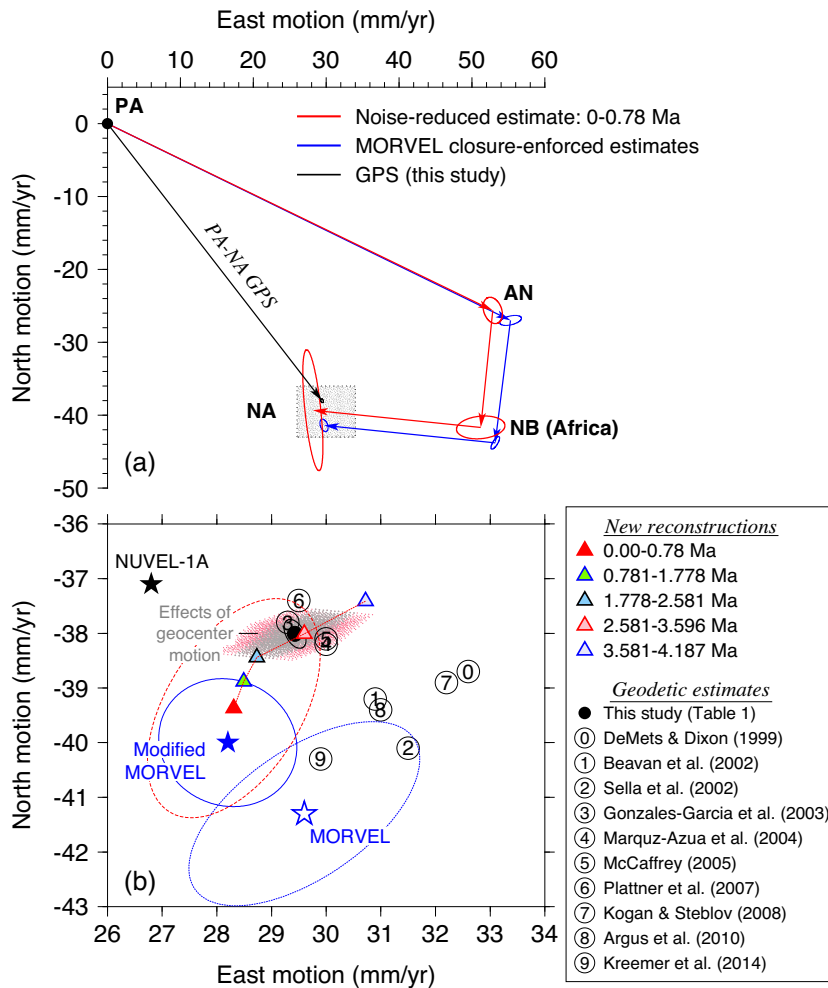
Figure 9. Plate circuit velocity diagram at 36.0°N, 120.6°W on the San Andreas Fault. (a) Linear velocities are estimated with (1) MORVEL angular velocities from the Pacific–Antarctic–Nubia–North America plate circuit (blue), (2) our new, high-resolution 0–0.78-Myr angular velocities for the same plate circuit (red), (3) our GPS-derived angular velocity in Table 1 (black). The shaded rectangle in (a) is enlarged in (b). (b) Comparison of Pacific–North America linear velocities estimated at 36.0°N, 120.6°W by (1) the six stage angular velocities that span the past 4.2 Myr (Table 6), (2) the MORVEL and NUVEL-1A (DeMets *et al.* 1994) angular velocities (open blue and black stars, respectively), (3) an angular velocity derived from an inversion of a modified version of the MORVEL global plate motion data (blue star), (4) the GPS-based angular velocity from Table 1 (black circle), and (5) angular velocities from ten geodetic studies listed in the legend. The grey and pink regions show the sensitivity of our newly estimated geodetic velocity (black circle) to a range of assumed geocentre motions in IGS08 (Section 5.1.2). Plate abbreviations are specified in Fig. 2 caption. All ellipses are 2-D, 1σ.

given by the new angular velocities for the past 4.2 Myr; (2) slip directions that are close to or slightly clockwise from our geologic estimates; (3) poles that are close to or south of the youngest geologic poles, consistent with long-term southward migration of the pole of rotation.

At a reference site on the San Andreas Fault, our newly estimated GPS angular velocity gives an instantaneous rate of 48.1±0.3 mm yr^{-1}. This agrees well with the 48.2 mm yr^{-1} average rate estimated from the angular velocities for the past 4.2 Myr (Table 6). The other ten geodetic angular velocities give rates of 47.7 to 51.0 mm yr^{-1} (light blue and purple lines in Fig. 8a). We provisionally conclude that the scattered geodetic rates are consistent with the plate kinematic evidence for a steady plate rate since 4.2 Ma. Similar comparisons at other locations along the plate boundary support this inference.

On average, slip directions that are estimated from the geodetic angular velocities are oriented 5±2° clockwise from slip directions for times before 5.2 Ma (Figs 8 b and 9b). The geodetic estimates thus corroborate the clockwise rotation of the plate slip direction

since 5.2 Ma, but suggest that it has been 2°–3° smaller than indicated by our geologically derived angular velocities.

Ten of the eleven geodetic poles are located several angular degrees north to northwest of our poles for Chrons 1n through 3n.1, outside the 95 per cent confidence region for the C1n pole (Fig. 6). Although this difference might indicate that the rotation pole has moved several angular degrees northwestwards since 0.78 Ma, it is difficult to reconcile with the evidence for southward migration of the geologic poles since at least 8 Ma (Fig. 6). Other causes must thus be sought. One source of potential systematic bias in the geodetic estimates is slow drift of Earth's centre of mass with respect to the origin of the international terrestrial reference frame (ITRF), as discussed by Argus (2007). Any drift of the geodetic reference frame relative to the geocentre will impart a systematic bias to all geodetic site velocities that are estimated in that frame of reference, which in turn will propagate into and bias geodetic estimates of plate angular velocities.

We explored the effects of possible origin drift on our Pacific–North America GPS angular velocity via a simple two-stage

procedure. From independent analyses of a variety of space geodetic data, Wu *et al.* (2011) and Argus (2012) estimate upper bounds of ~0.5 mm yr^{-1} on the X and Y components of any origin drift in ITRF2008 and respective upper limits of ~0.5 mm yr^{-1} and ~1.0 mm yr^{-1} on the Z component. We therefore systematically adjusted (in increments of 0.1 mm yr^{-1}) the Cartesian components of each of the 1012 Pacific and North America plate GPS station velocities included in our data (Section 2.2) for assumed origin drift of up to ±0.5 mm yr^{-1} in each of the X and Y components and ±1.0 mm yr^{-1} in the Z component. We then inverted each set of adjusted site velocities to determine their corresponding, best-fitting Pacific–North America angular velocity.

Fig. 6 shows the resulting distribution of geodetic poles, one (grey region) for the smaller ±0.5 mm yr^{-1} bounds estimated by Wu *et al.* (2011) for all three Cartesian drift components and the other (pink region) for the larger ±1 mm yr^{-1} bounds on the Z drift component estimated by Argus (2012). Both define pole uncertainty regions that are larger than the formal 1-σ confidence ellipse we derived from the original 1012 GPS site velocities (shown by the pale blue ellipse in Fig. 6). In three dimensions, the volumes of the 1σ error ellipsoids calculated for the two distributions described above are respectively 30 times and 75 times larger than the volume of the formal error ellipsoid. The uncertainty in the angular velocity due to possible drift of the geocentre is thus much larger than the formal uncertainties, whose validity depends on the probably incorrect assumption that errors in GPS site velocities are uncorrelated between sites.

The larger range of permissible geodetic solutions when we allow for drift of Earth's geocentre still falls outside the 95 per cent confidence region of our C1n rotation (Fig. 6), although some of the permissible geodetic solutions reduce the vector difference between the C1n and geodetic velocities to only 1.0 mm yr^{-1} at the reference point in California (Fig. 9). We postulate that the remaining difference is caused by other factors that may include biases or random errors in the geologic and/or geodetic data, possible distributed tectonic deformation of one or more of the Pacific, Antarctic, Nubia, or North America plates, and/or the horizontal effects of thermal contraction of the plates (e.g. Kumar & Gordon 2009; DeMets *et al.* 2014a; Kreemer & Gordon 2014).

5.2 Plate motion history: comparison to previous estimates

Other estimates of Pacific–North America plate motion that have been published during the past ≈20 yr include (but are not limited to) those of Atwater & Stock (1998), Argus & Gordon (2001), Wilson *et al.* (2005) and Doubrovine & Tarduno (2008). Royer *et al.* (2006) also discuss the implications of alternative sequences of Pacific–North America rotations they estimated for four times since 11.0 Ma, but do not tabulate their rotations. Comparisons between our new estimates and those of previous studies (excepting those of Royer *et al.* 2006) are shown in Fig. 10 and discussed briefly below. To facilitate the comparison, we focus on velocities calculated at a reference location on the San Andreas Fault (Fig. 10).

Pacific–North America plate motion estimated with our noise-reduced angular velocities (Fig. 10) has evolved in a simple fashion during the past 20 Myr, as follows: (1) Stage velocities increased from 30 mm yr^{-1} at 19.7–18.7 Ma to 52 mm yr^{-1} at 12 Ma, a speedup of ≈70 per cent, (2) Rates estimated for ten intervals since 8 Ma have varied by less than ±2 per cent from an 8-Ma-average rate of 47.8±0.7 mm yr^{-1} (Fig. 10a). (3) Slip directions have rotated ~25°
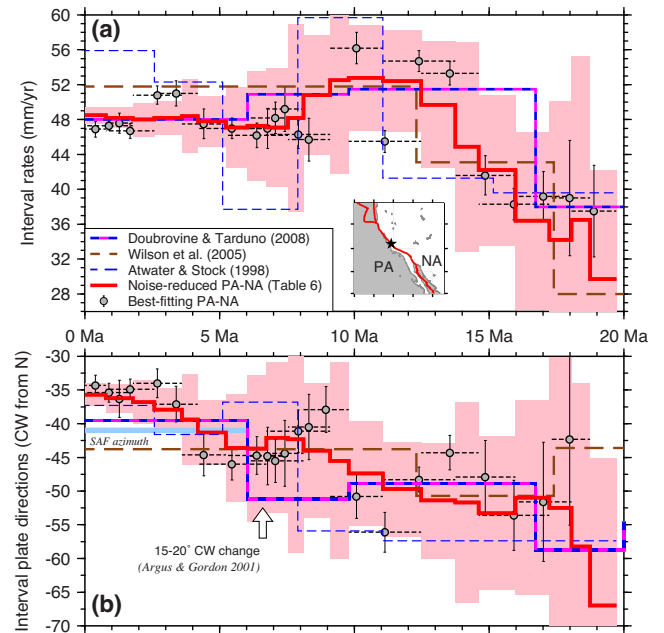
Figure 10. Pacific with respect to North America plate interval rates (a) and slip directions (b), 20 Ma to present, estimated on the San Andreas Fault (36.0°N, 120.6°W at the star in the inset map). The red lines and grey circles show interval velocities estimated with noise-reduced (Table 6) and best-fitting angular velocities, respectively. One-sigma uncertainties are propagated from the angular velocity covariances. Horizontal dashed lines show the intervals spanned by the best-fitting angular velocities. Light blue line shows the San Andreas Fault (SAF) azimuth in central California. The following finite rotations were used to determine the Atwater & Stock (1998) interval velocities: Chrons 2An.1 (2.581 Ma), 3n.4 (5.116 Ma), 4n.2 (7.90 Ma), 5n.2 (11.056 Ma), 5Bn.2 (15.16 Ma), and 6n (19.722 Ma) (J. Stock, private communication, 2015). The finite rotations used to determine the Wilson *et al.* (2005) interval velocities were for 12.3, 17.4 and 24.1 Ma (from table 3 of Wilson *et al.* 2005).

clockwise since 19.7 Ma (Fig. 10b). Within the uncertainties, the directions have changed continuously or rotated by 10–15° from 18 to 9 Ma and an additional 5°–7° from 5.2 Ma to the present. Some of the change in direction is clearly linked to significant clockwise rotation of the Pacific–Antarctic slip direction since 12–10 Ma (Fig. 7c).

We are less certain of the robustness of other, possible higher-order variations in the estimated motion, including a ~5-Myr-long period of possibly faster plate motion from 13–8 Ma (Fig. 10a). We consider the estimated stage motions for 19.7–18.7 Ma (C6no to C6ny) to be less robust because they depend partly on Nubia–Antarctic Chron 6ny and 6no rotations that are derived from a handful of possibly incorrect identifications of Anomaly 6 from the western end of the Southwest Indian Ridge (Section 4.2 and DeMets *et al.* 2015b). We thus place little or no emphasis on 19.7–18.7 Ma interval velocities below.

The stage rates given by angular velocities that we determined from finite rotations estimated by other authors vary widely (Fig. 10a). For example, rates estimated from the Atwater & Stock (1998) rotations vary erratically and fall outside the uncertainties of our estimated rates for all times since 13 Ma (dashed-blue line in Fig. 10a). The rates estimated with the Wilson *et al.* (2005) rotations confirm the 20–12 Ma ≈70 per cent speedup in motion that is indicated by our angular velocities, but are ~10 per cent faster than our rate estimates for times since 8 Ma. Stage rates that are derived from the Doubrovine & Tarduno (2008) rotations agree well with

our own estimates for 12 Ma to the present, but disagree for earlier times.

The slip directions given by our angular velocities and those for all but one previous study (that of Wilson *et al.* 2005) have rotated 20° or more clockwise since 19.7 Ma (Fig. 10b). A clockwise rotation of the plate slip direction at locations in western North America is therefore a robust feature of global plate circuit reconstructions. Our angular velocities suggest that this change occurred gradually or in two phases (Fig. 10b), whereas previous, lower-resolution studies suggest that it occurred rapidly between 8 and 6 Ma. We suspect that the rapid change in the plate slip direction at 8-6 Ma suggested by previous studies may be an artefact of undersampling of the underlying plate motion history.

5.3 Kinematic constraints on post-8 Ma deformation in central California

Reconstructions of Pacific–North America plate motion are important for our understanding of the tectonic evolution of central California in at least two respects. Accurate reconstructions are needed to test whether the well-described Pliocene (5.3–2.6 Ma) onset of folding, faulting, and topographic uplift in central California (e.g. Aydin & Page 1984; Page *et al.* 1998) could have been triggered by a change in plate motion. Estimates of Pacific–North America plate motion also constrain how oblique convergence between the Pacific Plate and Sierra Nevada/Great Valley block is partitioned between strike-slip faults in central and western California (i.e. the San Andreas, Rinconada, and Hosgri-San Gregorio strike-slip faults) and folds and thrust faults that accommodate the fault-normal, convergent component of motion (e.g. Page *et al.* 1998; Argus & Gordon 2001; Dickinson *et al.* 2005; Titus *et al.* 2011; Langenheim *et al.* 2013). Both topics are treated below.

5.3.1 A trigger for the central California Pliocene orogeny: Pacific–Sierra Nevada motion since 10 Ma

For the ensuing analysis, we estimated two sequences of rotations that describe the motion of the Sierra Nevada/Great Valley block (hereafter abbreviated SNGV) relative to the Pacific plate over the past 10 Myr. Both combine Pacific–North America rotations from Table 5 with North America-SNGV plate rotations extrapolated from geodetic angular velocities that were estimated from block modelling of the velocities of GPS sites in the western United States (d'Alessio *et al.* 2005; McCaffrey 2015). The assumption of steady-state SNGV-North America plate motion that is embedded in this part of the analysis constitutes a potentially important source of error, particularly for the oldest rotations we estimate.

Fig. 11 shows flow lines and stage velocities in central California reconstructed with the two SNGV-Pacific plate rotation sequences (found in Supporting Information Table S2) and their associated angular velocities. For ages of 9 Ma to 5.2 Ma, the estimated slip directions for both sequences of angular velocities were parallel to the San Andreas Fault within their uncertainties (Fig. 11c). Between 5.2 Ma and the present, the slip directions have rotated progressively farther clockwise from the fault to a present obliquity of 12° (Fig. 11c). The estimated fault-normal contraction rate has thus become progressively faster during the Pliocene. Geodetic estimates of the SNGV-Pacific angular velocity from d'Alessio *et al.* (2005) and this study (Table 1) confirm that SNGV-Pacific plate motion in central California is presently obliquely convergent to the San Andreas Fault (purple lines in Fig. 11c).

The kinematic evidence that SNGV-Pacific plate motion first acquired a convergent component orthogonal to the San Andreas Fault between 5.2 Ma and 4.2 Ma agrees with dates inferred by other authors for the onset of Pliocene uplift in central California. Miller (1999) estimates an onset age of 6–5.4 Ma for uplift of the Diablo Range northeast of the San Andreas Fault from a seismic stratigraphic study of sediments in the San Joaquin basin west of the fault. Page *et al.* (1998) estimate an approximate earliest onset age of 4 Ma for shortening in central California based on their analysis of folding and thrusting of Pliocene-Pleistocene-age non-marine sedimentary rocks in the coastal ranges of western California. Argus & Gordon (2001) estimate that 4^{+2}_{-1} Myr has been required for the mountains of central California to attain their present cross-sectional area at present geodetic shortening rates. And Ducea *et al.* (2003) estimate an approximate uplift age of 6 Ma for the Santa Lucia Range from a thermochronometric study of its uplift and denudation rates during the past 10 Myr.

We conclude that the Pliocene orogeny in western California began after 5.2 Ma when the direction of SNGV-Pacific plate motion rotated clockwise of the local N41°W azimuth of the San Andreas Fault (Fig. 10c). Contrary to previous studies that variously report 10°–20° clockwise changes in the Pacific–North America direction between 8 Ma and 6 Ma (Fig. 10b), we find no evidence for a sudden clockwise change in the slip direction that could have triggered the Pliocene orogeny. The new rotations instead reveal either a gradual reorientation of the plate slip direction since 10 Ma or a 2°–3° clockwise rotation at 5.2–4.2 Ma following a several-Myr-long period during which SNGV-Pacific plate motion was parallel to the San Andreas Fault (Fig. 10b).

5.3.2 Deformation partitioning in central California

The total post-5-Ma shortening associated with the Pliocene orogeny in central California can be quantified by resolving the flow-line displacements estimated with the SNGV-Pacific rotations in Supporting Information Table S2 onto the direction orthogonal to the N41°W-striking San Andreas Fault. For the rotations estimated with the McCaffrey (2015) SNGV-North America angular velocity (our preferred estimates), the maximum, estimated shortening is 24.4±3.5 km since 5.2 Ma and 22.9±2.6 km since 4.2 Ma. Including a ±1° uncertainty in the N41°W fault azimuth increases the respective 1σ uncertainties in the 5.2 Ma and 4.2 Ma shortening estimates to ±5 km and ±4 km. The fault-normal contraction rate has thus averaged 5.5±1 mm yr⁻¹ since 4.2 Ma.

The new estimates agree well with independent geodetic and geological observations. Measurements at GPS sites in central California indicate that present fault-normal shortening rates are 4–5.8 mm yr⁻¹ (d'Alessio *et al.* 2005; McCaffrey 2005; Titus *et al.* 2011; DeMets *et al.* 2014b). Geological estimates of the minimum amount of boundary-normal shortening that has occurred include a 12±2 km estimate from a structural analysis of post-Pliocene folding and faulting in the San Andreas Fault borderlands in central California (Titus *et al.* 2011) and a 15 km estimate from the cross-sectional area of mountain ranges that flank the San Andreas Fault's creeping segment (Argus & Gordon 2001). In addition, Namson & Davis (1988) estimate that as much as 33 km of shortening has occurred based on reconstructions of balanced cross-sections. Titus *et al.* (2011), however, argue that this overestimates the total shortening.

The newly estimated SNGV-Pacific plate rotations (Supporting Information Table S2) indicate that the component of the plate
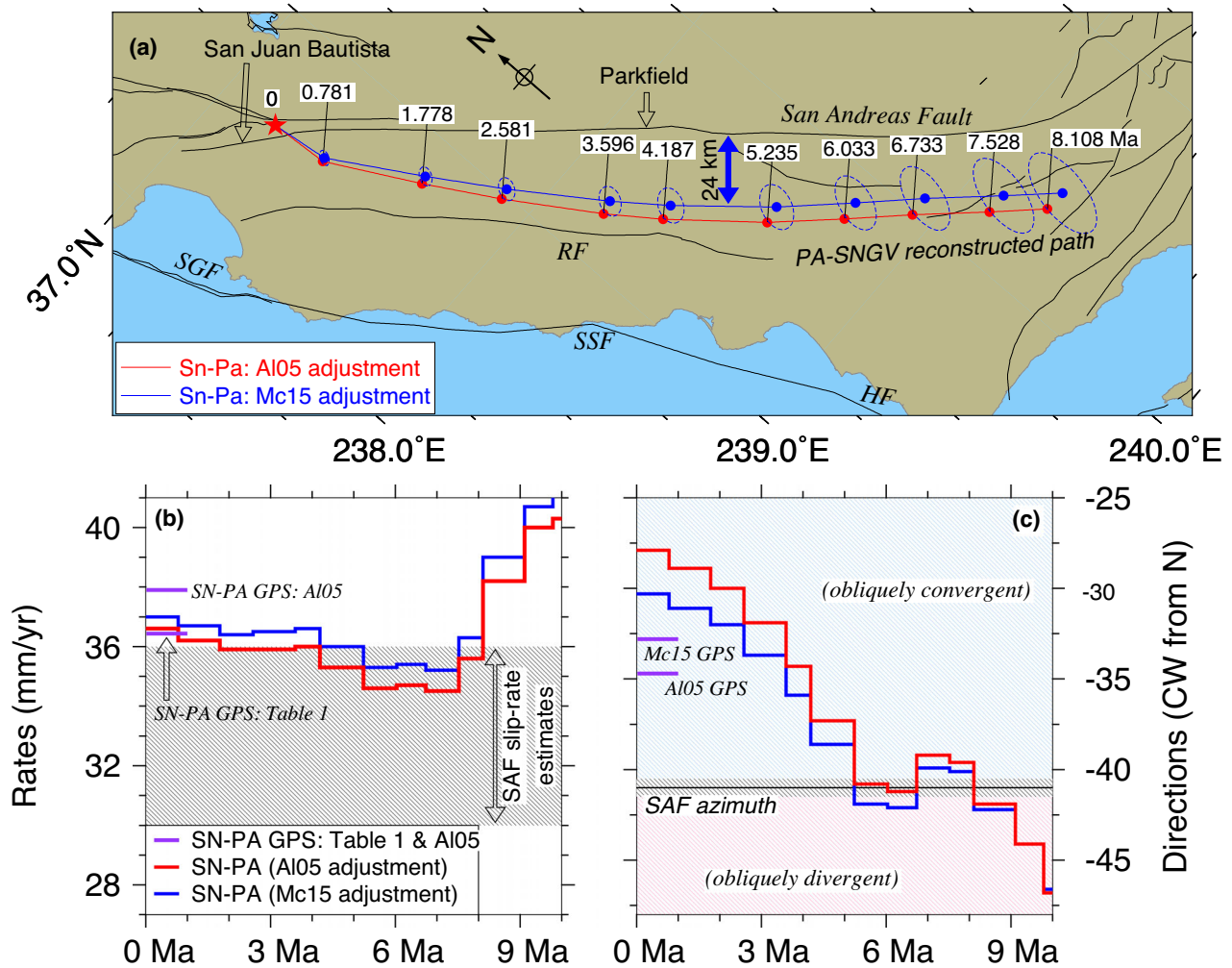
Figure 11. Pacific–Sierra Nevada relative motion in central California since 8 Ma. (a) Pacific plate displacement paths (blue and red lines) relative to the SNGV block reconstructed using rotations from Supporting Information Table S2 (see the text). The red and blue flow lines were derived from SNGV-Pacific rotations that were based partly on the SNGV-North America geodetic angular velocities estimated by d'Alessio *et al.* (2005) (abbreviated 'Al05' in the legend) and McCaffrey (2015) (abbreviated 'Mc15' in the legend). The double-headed blue arrow in (a) shows the cumulative 24±5 km component of convergence orthogonal to the San Andreas Fault (SAF) estimated to have occurred since 5.2 Ma, when the plate motion acquired a component orthogonal to the fault. The map projection is oblique Mercator with its horizontal axis aligned with the N41°W-striking San Andreas Fault. Map location is shown in Fig. 1. HF, RFZ, SGF and SSF are the Hosgri, Rinconada, San Simeon and San Gregorio faults, respectively. (b) SNGV-Pacific plate interval rates estimated on the San Andreas Fault (36.4°N, 121.0°W) by angular velocities derived from our SN-PA finite rotations (Supporting Information Table S2), by the d'Alessio *et al.* (2005) geodetic SNGV-Pacific angular velocity (labelled 'Al05 SN-PA'), and by our own geodetic angular velocity (labelled 'SN-PA GPS' and found in Table 1). The grey area in (a) spans the range of geodetic and geologic slip-rate estimates for the San Andreas Fault (e.g. Sieh & Jahns 1984; Noriega *et al.* 2006; Schmalzle *et al.* 2006; Titus *et al.* 2011; Tong *et al.* 2014). (b) SN-PA interval directions estimated with angular velocities identified in the Panel b legend compared to the San Andreas Fault azimuth. The pink and light blue regions show azimuths for which the plate motion is respectively obliquely divergent or obliquely convergent to the San Andreas Fault.

motion parallel to the San Andreas Fault has averaged 36.5-37 mm yr^{−1} since 0.78 Ma (blue and red lines in Fig. 11b). Encouragingly, the d'Alessio *et al.'* (2005) geodetically derived SNGV-Pacific plate angular velocity gives a fault-parallel slip component of 36.5 mm yr^{−1} and our new geodetic estimate (Table 1) gives 38 mm yr^{−1} (purple lines in Fig. 11b). These collectively indicate that the present, margin-parallel slip rate summed across all strike-slip faults in central California is 36.5–38 mm yr^{−1}.

Slip-rate estimates for the San Andreas Fault in central California include 33.9±2.9 and 32.4±3.2 mm yr^{−1} Holocene rates from stream offsets (Sieh & Jahns 1984; Noriega *et al.* 2006), a 31–32 mm yr^{−1} rate from GPS observations along the fault's creeping segment (Titus *et al.* 2011), and a 34.5 mm yr^{−1} rate from elastic

half-space modelling of the central creeping segment (Tong *et al.* 2014). The San Andreas Fault slip rates are all 2–5 mm yr^{−1} slower than the 36.5–38 mm yr^{−1} margin-parallel slip budget, consistent with additional slip along other strike-slip faults such as the Reliz-Rinconada and Hosgri-San Simeon-San Gregorio faults of western California (located in Fig. 11a). Geodetic and geologic evidence indicate that the Holocene slip rate is unlikely to exceed 1 mm yr^{−1} for the Reliz-Rinconada fault (Dibblee 1976; Rolandone *et al.* 2008; Titus *et al.* 2011; Langenheim *et al.* 2013) and 1–3 mm yr^{−1} for the Hosgri-San Gregorio fault zone (Hall *et al.* 1994; DeMets *et al.* 2014b; Johnson *et al.* 2014). We conclude that the plate kinematic, geologic, and geodetic estimates of the margin-parallel component of present deformation in central California are mutually consistent.
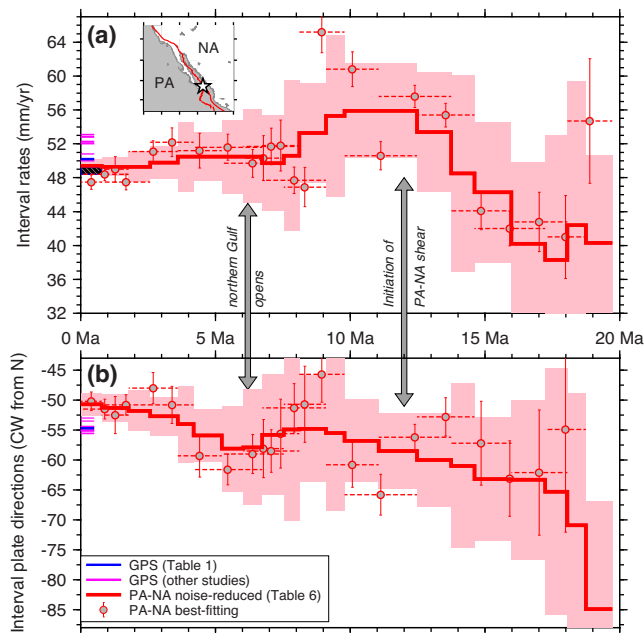
5.4 Comparison to Gulf of California geologic constraints

The Gulf of California plate boundary segment formed at ≈12 Ma, when the Pacific and North America plates first came into direct contact in the vicinity of the present Gulf of California (Lonsdale 1991; Stock & Lee 1994; Michaud *et al.* 2006). Structural and marine seismologic observations indicate that plate boundary deformation began localising along the former Miocene volcanic arc in the proto-Gulf of California and areas farther inland shortly after 12 Ma (e.g. Umhoefer *et al.* 2002; Sutherland *et al.* 2012; Bennett *et al.* 2013). Since 12 Ma, the plate motion has been accommodated variously by strike-slip faults and pull-apart basins within the Gulf of California, by the Tosco-Abreojos Fault Zone west of the Baja Peninsula (Fig. 1), and by normal faults and strike-slip faults in the Gulf Extensional Province and areas of northwestern Mexico (Fig. 1).

5.4.1 Pacific–North America plate motion history: Gulf of California

Fig. 12 shows stage velocities in the southern Gulf of California as estimated with the angular velocities in Table 6. During the past 8.1 Myr, the rates estimated for ten distinct intervals have varied from 49.3 to 50.6 mm yr^{-1}, consistent with the 50.2±0.2 mm yr^{-1} instantaneous rate estimated with our GPS angular velocity (Table 1) and with 49-53 mm yr^{-1} rates given by angular velocities from other geodetic studies (sources listed in Fig. 9). Slip directions have rotated 10°–15° clockwise between 18 Ma and the present (red line in Fig. 12b), either gradually or during two shorter phases, as described in Section 5.2.

No notable changes in the estimated stage rates or directions coincide with the well-dated onset of opening across the northern

Gulf of California at 6.2±0.2 Ma (Oskin & Stock 2003; Bennett *et al.* 2015). It thus seems unlikely that opening of the northern Gulf of California was triggered by a change in plate motion. The opening of the southern Gulf of California at ≈12 Ma, however, appears to be correlated with a kinematic change from accelerating plate motion prior to 12.4 Ma to nearly steady motion thereafter (Fig. 12a). A connection between the two thus cannot be dismissed.

5.4.2 Kinematic versus structural reconstructions of the Gulf of California at 6.3 Ma

Structural studies of the margins of the northern Gulf of California indicate that by 6.3 Ma, most Pacific–North America plate motion had concentrated along the former Miocene volcanic arc in the proto-Gulf of California (e.g. Oskin *et al.* 2001; Oskin & Stock 2003; Bennett *et al.* 2015). Relevant to this analysis, Oskin & Stock (2003) describe four well-exposed ignimbrite units that erupted along the Miocene volcanic arc between 12.5 Ma and 6.1±0.5 Ma that can be used to reconstruct the conjugate margins of the Gulf. From reconstructions of the relative locations of these ignimbrites prior to their separation, Oskin & Stock (2003) estimate that the conjugate, rifted ignimbrites have been offset by 255±10 km in a 130–132° direction since 6.2±0.2 Ma. When summed with additional deformation along this plate boundary transect, Oskin & Stock (2003) report net boundary-parallel movement of 276–296 km, equal to ≈90 per cent of the 6.3-Ma-to-present 320-km displacement extrapolated from Pacific–North America rotations estimated by Atwater & Stock (1998).

We revisited this comparison using our new rotations (Table 5) and new and/or revised estimates of deformation within three field areas along this transect. Bennett *et al.* (2015) propose that the conjugate ignimbrites and areas of thick continental crust that border the northern Gulf of California are better juxtaposed using a 235-km (130°) offset (Vector 1 in Fig. 13b) rather than the 255-km offset estimated by Oskin & Stock (2003). An analysis of new and existing palaeomagnetic measurements from a 6.4-Myr-old volcanic tuff exposed in the Puertocitos Volcanic Province and undeformed adjacent areas of the Baja Peninsula (located in Fig. 13a) reveals consistent, 15°±5° clockwise vertical-axis rotations within a 45-km-wide rotated domain (Bennett & Oskin 2014). Following Lewis & Stock (1998), we applied a uniform-rotation model (shown in their Fig. 8) to convert the observed rotation to equivalent displacement components parallel and orthogonal to the N20°W-striking rotated domain. This gives 11.6±4 km of boundary-parallel dextral slip and 3.1±1.1 km of boundary-normal extension. The net displacement vector of 11.7±4 km towards 332° (Vector 2 in Fig. 13b) is only half the 23±9 km (340°) offset previously estimated by Lewis & Stock (1998) for this area.

Detailed structural and palaeomagnetic measurements within the coastal Sonora fault zone at the eastern end of the plate boundary transect indicate a cumulative northwest/southeast dextral offset of 6.2±1.1 km internal to the fault zone from 7.0 to 5.5 Ma (Bennett *et al.* 2013). We assume here that most or all of this deformation occurred after 6.3 Ma, as permitted by their observations (Vector 3 in Fig. 13b). Along the Sacrificio and Infiernillo Faults that border the coastal Sonora fault zone, Oskin & Stock (2003) estimate that 20±10 km of dextral offset has occurred since 12.6 Ma (Vector 4 in Fig. 13b). Bennett *et al.* (2013) suggest that the offsets across these two bounding faults may have occurred between 7.0 and 5.5 Ma, during the well-dated period of rapid deformation internal to the coastal Sonora fault zone.

Figure 12. Pacific–North America (PA–NA) interval rates (a) and slip directions (b) since 20 Ma at the Alarcon spreading segment in the southern Gulf of California (23.5°N, 108.5°W at star in inset map) from Table 6 angular velocities. The horizontal dashed lines show the time intervals spanned by the best-fitting angular velocities. One-sigma uncertainties are propagated from angular velocity covariances. The sources for the GPS estimates are listed in Fig. 9.
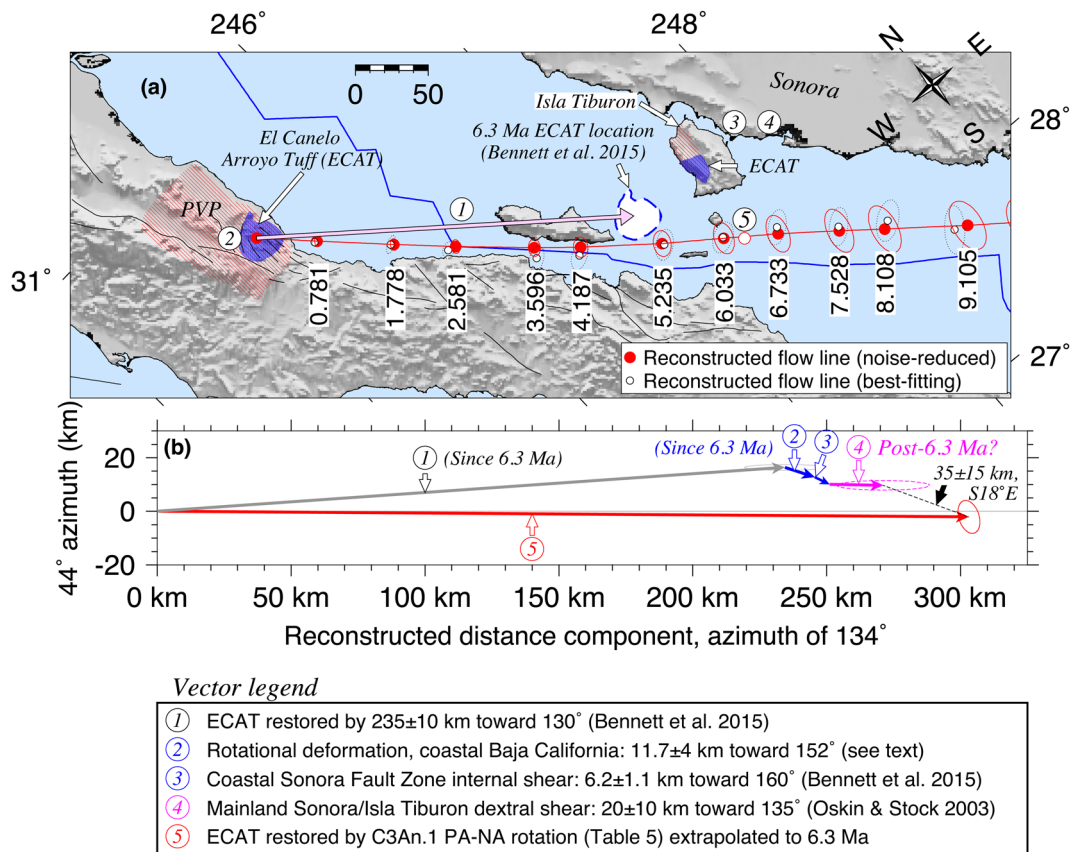
Figure 13. (a) Comparison of 6.3 Ma structural reconstruction of the Puertocitos Volcanic Province (PVP) on the conjugate rifted margins of the Upper Delfin Basin (Bennett *et al.* 2015) to noise-reduced and best-fitting Pacific–North America (PA–NA) flow lines estimated with rotations from Tables 4 and 5. Age- and geochemically correlative ignimbrites that include the El Canelo Arroyo Tuff (purple regions labelled ECAT) outcrop on both Isla Tiburon on the North America plate and Baja California on the Pacific plate (Oskin & Stock 2003). Map is an oblique Mercator projection centred on the Table 5 C3An.1 finite rotation. (b) Vector comparison of independent plate kinematic (red arrow) and structural displacements for the plate boundary transect depicted in (a). The sources for displacement vectors 1 through 5 are given in the legend. The 1σ error ellipses for Vectors 3 and 4 incorporate the uncertainties for Vectors 1–3 and 1–4, respectively, and are thus cumulative. The dextral shear shown by Vector 4 has occurred since 12.6 Ma (Oskin & Stock 2003) and possibly since 6.3 Ma based on post-6.3-Ma ages for shear within the Coastal Sonora Shear Zone (Bennett *et al.* 2013). See the text for further discussion.

Summing the deformations described above gives either 252 ± 11 km, S48.9°E or 272 ± 15 km, S48.6°E of net movement between the Baja Peninsula and North America for this transect depending on the age that we assign to the assumed 20 ± 10 km of slip on the Sacrificio and Infiernillo Faults (Fig. 13b). For comparison, the 6.03-Myr Pacific–North America rotation in Table 5 gives an extrapolated, 6.3-Ma-to-present displacement of 303 ± 5.6 km, S45.2°E±1.5° along this transect (Vector 5 in Fig. 13b). Subtracting the structural displacements referenced above from the estimated plate displacement leaves respective structural slip deficits of 35 ± 15 km (1σ) towards S18°E±11° or 54 ± 11 km (S28°E±6°), both parallel- to sub-parallel to the plate boundary.

Possible explanations for the 35 ± 15 or 54 ± 11 km residual displacements include (1) movement since 6.3 Ma between the Baja California Peninsula and Pacific Plate, possibly along the still-active Tosco-Abreojos Fault Zone west of the peninsula (Michaud *et al.* 2004), (2) other post-6.3-Ma deformation along faults in the Gulf Extensional Province and in the Baja California Peninsula and (3) inaccuracies in the ages, magnitudes, and/or directions of the structural/palaeomagnetic estimates (e.g. Seiler *et al.* 2010) and the C3An.1 plate rotation estimated herein. We consider these briefly below.

From GPS measurements at sites on the Baja Peninsula, North America and Pacific plates, Dixon *et al.* (2000) and Plattner *et al.*

(2007) show that the Baja Peninsula moves several millimetres per year relative to the Pacific plate. Along the flow line shown in Fig. 13 b (29°N, 113°W), the Baja Peninsula-North America angular velocity estimated by Plattner *et al.* (2007) gives motion of 44.7 ± 2.5 mm yr^{-1} towards N48.7°W±3.1°. At the same location, our newly estimated Pacific–North America GPS angular velocity (Table 1) gives movement of 48.1 ± 0.1 mm yr^{-1} towards N47.5°W±0.1°. Baja California's differential velocity relative to the Pacific plate is thus 3.5 ± 2.5 mm yr^{-1} towards S32.1°E±3.1°. Extrapolated back to 6.3 Ma, this gives 22.0 ± 16 km of motion towards S32.1°E±3.1°, consistent with nearly pure dextral slip along the N36°W-trending Tosco-Abreojos Fault Zone.

Subtracting the estimated, 6.3-Ma-to-present Baja-Pacific plate movement from the 35 ± 15 km, S18°E and 54 ± 11 km, S28°E structural slip deficits leaves modified residual displacements of 15 ± 22 km (S3°W) and 32 ± 19 km (S25°E). Uncertainties about the precise opening age of the northern Gulf of California affect the magnitudes of these estimated residual displacements by 5 km per 0.1 Myr, such that an opening age of 6.1 Ma instead of 6.3 Ma would reduce the respective structural slip deficits to 5 ± 22 km and 22 ± 19 km.

We conclude that our new plate kinematic estimate of Pacific–North America motion and independent, structurally summed displacements across the northern Gulf of California for the past
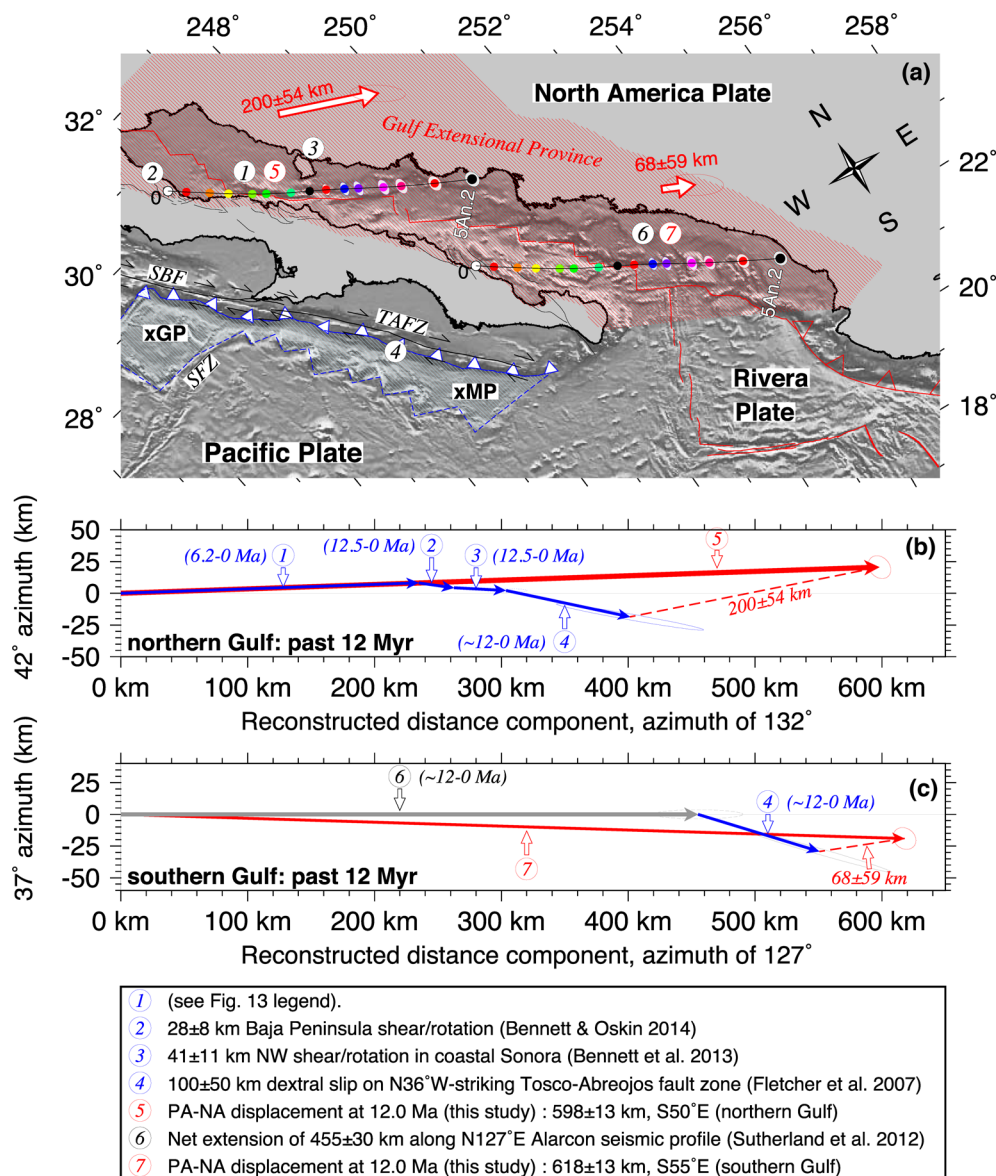
Figure 14. (a) Pacific plate flow lines for the past 12 Myr (coloured circles) for transects of the northern and southern Gulf of California reconstructed with finite rotations from Table 5. The circled numerals shown on the map and defined in the legend identify structural and seismic measurements of the plate boundary deformation that are shown in the Panel b and c vector diagrams. All ellipses are 2-D, standard error ellipses. (b) Summation of vectors 1 to 4 (defined in the legend) for the northern Gulf transect gives net deformation since 12 Ma that is 200±54 km (1σ) less than the estimated plate displacement (Vector 5). (c) Vector summation for the southern Gulf transect for which the residual displacement is only 68±59 km. The open red vectors in (a) show the direction and magnitude of the missing deformation for both transects. 'xGP' and 'xMP' locate the extinct Guadalupe and Magdalena microplates. 'TAFZ', 'SBF' and 'SFZ' identify the Tosco-Abreojos fault zone, San Benito Fault and Shirley fracture zone, respectively.

6.3 Myr are consistent within their combined 95 per cent uncertainties (±40 km) and possibly within their combined 1σ uncertainties (±20 km). We attribute the remaining ≈10–30 km differences between the structural and plate kinematic estimates to (1) uncertainties in our newly estimated finite rotations, (2) uncertainties in the magnitudes and directions of the displacements inferred from the structural and palaeomagnetic observations and in their estimated ages, (3) deformation along structures that are not represented in our analysis, and (4) uncertainties in the GPS estimate of Baja–Pacific plate motion and our approximation of that motion as steady for the past 6.3 Ma. The ≈10–30 km difference constitutes an approximate upper limit for the integrated effects of plate non-rigidity around the global plate circuit.

5.4.3 Kinematic versus structural reconstructions of the Gulf of California at 12 Ma

Stratigraphic evidence clearly indicates that distributed extension in southern regions of the proto-Gulf of California began at 14–12 Ma (Sutherland *et al.* 2012), some six to eight million years earlier than the northern Gulf of California began opening (Oskin & Stock 2003; Bennett *et al.* 2015). The different opening times for the two regions require that underwater faults in the present Gulf became active at least five million years earlier in the southern Gulf of California than in the north. It follows that the onshore and offshore faults that accommodate Pacific–North America plate motion must have partitioned the plate motion differently in the northern and

southern Gulf of California between 12 and 6 Ma. We next quantify this difference using our newly estimated rotations.

Fig. 14 summarizes the relevant model estimates and observations. Along a transect of the northern Gulf of California, our C5An.2 finite rotation (12.474 Ma) gives a finite displacement of 598 ± 13 km ($130.0\pm1.2°$ average azimuth) at 12.0 Ma (Figs 14 a and b). Independent, structural estimates of deformation since 12 Ma relevant to this transect (Fig. 14b) include (1) 235 ± 10 km of post-6.3-Ma offset along the faults within the Gulf (Bennett *et al.* 2015), (2) 28 ± 8 km of N40°W-directed displacement since 12.6 Ma across the Puertocitos Volcanic Province in eastern Baja California as constrained by palaeomagnetic evidence for $36\pm10.5°$ of clockwise rotation of the 12.5-Ma-old San Felipe Tuff (Bennett & Oskin 2014) (see the previous section for the method we used to estimate the net displacement), (3) 41 ± 11 km of northwest-directed dextral shear across the coastal Sonora fault zone since 11.5 Ma (Bennett *et al.* 2013), and (4) 100 ± 50 km of dextral slip along the Tosco-Abreojos fault zone (Fletcher *et al.* 2007) (or possibly less if some of that slip occurred before 12 Ma). Subtracting the vector sum of all four structural estimates from the 598 ± 13 km estimated plate displacement leaves a 200 ± 54 km (1-σ), S59°E$\pm5°$ residual displacement for the northern Gulf of California (open red arrow in Fig. 14a).

Along the southern transect, our C5An.2 rotation gives 618 ± 13 km of displacement since 12.0 Ma (red vector in Fig. 14c). Independent, structural estimates of deformation in the southern Gulf of California include (1) 455 ± 30 km of cumulative extension along a N127°E-trending seismic refraction transect of the Gulf (Sutherland 2006; Sutherland *et al.* 2012), and (2) 100 ± 50 km of dextral slip along the Tosco-Abreojos fault zone (Fletcher *et al.* 2007). Subtracting these from the estimated plate displacement leaves a residual displacement of 68 ± 59 km (1σ) towards S62°E (Figs 14 a and c).

Although the 200 ± 54 km and 68 ± 59 km residual displacements described above could be evidence for large errors in our estimate of Pacific–North America motion since 12.0 Ma, we consider it more likely that they approximate the amount of deformation that occurred between 12 Ma and 6.3 Ma on faults that were not included in the vector analysis. In the southern Gulf of California, where faults within the gulf began accommodating most of the plate motion as early as 12 Ma, our analysis indicates that little or possibly no deformation (68 ± 59 km) occurred before 6.3 Ma along faults exterior to the gulf. In the northern Gulf of California, where rapid opening within the gulf did not commence until 6.2 ± 0.2 Ma, our analysis suggests that the cumulative 12–6.2 Ma displacement integrated across faults excluded from our vector analysis was 200 ± 54 km, S59°E$\pm5°$. Some of these faults were likely to be located in the Gulf Extensional Province and the Mexican Basin and Range province (Stock & Hodges 1989; Gans 1997; Henry & Aranda-Gomez 2000; Oskin *et al.* 2001; Oskin & Stock 2003; Fletcher *et al.* 2007; Bennett *et al.* 2013). Others may have included the palaeosubduction zone and abandoned spreading segments west of the Baja California Peninsula (Michaud *et al.* 2006).

From structural observations, Gans (1997) estimates that normal faults west of the Sierra Madre Occidental of northwestern Mexico (Fig. 1) accommodated 20–30 km or less of ENE–WSW-directed extension since $\approx$12 Ma. Field and radiometric observations summarized by Henry & Aranda-Gomez (2000) indicate that unspecified, additional extension occurred between 12 and 6 Ma on normal faults in the Mexican Basin and Range east of the Sierra Madre Occidental. For comparison, rotating our 200 ± 54 km, S59°E$\pm5°$ residual displacement onto the ENE–WSW extension direction (N75°E)

indicated by Gans (1997) gives 138 ± 21 km (1σ) of ENE–WSW extension and 144 ± 52 km of dextral shear (N15°W). Whether faults in northwestern Mexico could have accommodated this much additional extension and shear or whether some of the missing plate motion was accommodated by the now-extinct subduction interface west of the Baja California Peninsula and/or the abandoned Guadalupe and Magdalena spreading centres between 12 Ma and 8–7 Ma, as postulated by Michaud *et al.* (2006), remains to be answered.

## 5.5 Comparison to post-16 Ma geologically summed deformation across western North America

Reconstructions of Pacific–North America motion during the past $\sim$20 Myr are useful for testing hypotheses related to the opening of the U.S. Basin-and-Range and quantifying partitioning of the plate boundary deformation across the western United States (e.g. Dickinson 1996; Dickinson & Wernicke 1997; Atwater & Stock 1998; McQuarrie & Wernicke 2005). Here, we briefly evaluate the consistency of our new rotations with independent geologic estimates of deformation since 16 Ma across two well-studied transects of the plate boundary.

Fig. 15 compares reconstructions of the path of the offshore Mendocino Triple Junction relative to North America with our own rotations and those of Atwater & Stock (1998) and Wilson *et al.* (2005). To first order, all of the reconstructed flow lines agree for the past 8 Myr. For earlier times, the Atwater & Stock flow line extends progressively farther inland than the new flow line, reaching a maximum difference of 75 km along a great circle that trends N65°E at 18-20 Ma. Resolved onto the directions parallel and orthogonal to the present plate boundary (N40°W and N50°E), this difference suggests there has been 72 km less divergence and 19 km less dextral slip between the two plates since 20 Ma.

Fig. 16 compares the margin-parallel component of our reconstructed flow line displacements to independent estimates of geologic offsets for faults crossed by two strategically selected transects of the western United States (green lines in Fig. 15). Both transects cross the San Andreas Fault in central California, which has a well-determined, geological offset of 315 ± 10 km since 16 Ma (Graham *et al.* 1989 and references therein). Both also cross the central Basin and Range between the Colorado Plateau and Sierra Nevada mountains. Palinspastic reconstructions of geologic features along a transect of the central Basin and Range at 36–37°N give 235 ± 20 km of N78°W-directed Sierra Nevada/Great Valley block translation relative to the Colorado Plateau since 16 Ma (McQuarrie & Wernicke 2005), including a 185 ± 16 km component parallel to the plate margin (N40°W).

The combined San Andreas Fault and central Basin and Range margin-parallel displacements for the two transects are thus 500 ± 19 km since 16 Ma (shown by the blue and red areas in Fig. 16a). Along the reconstructed flow line in Fig. 15, our 16.0-Myr rotation gives a 764 ± 9 km (1σ) margin-parallel component of plate motion (Fig. 16b). This exceeds the summed, margin-parallel displacements for the San Andreas Fault and Basin and Range transect by 264 ± 21 km. We next consider whether deformation across other structures crossed by the two transects can account for the missing deformation.

The northernmost transect crosses the Hosgri-San Gregorio and Reliz-Rinconada strike-slip faults of central-western California before terminating on presumably unfaulted Pacific plate (Fig. 16a).
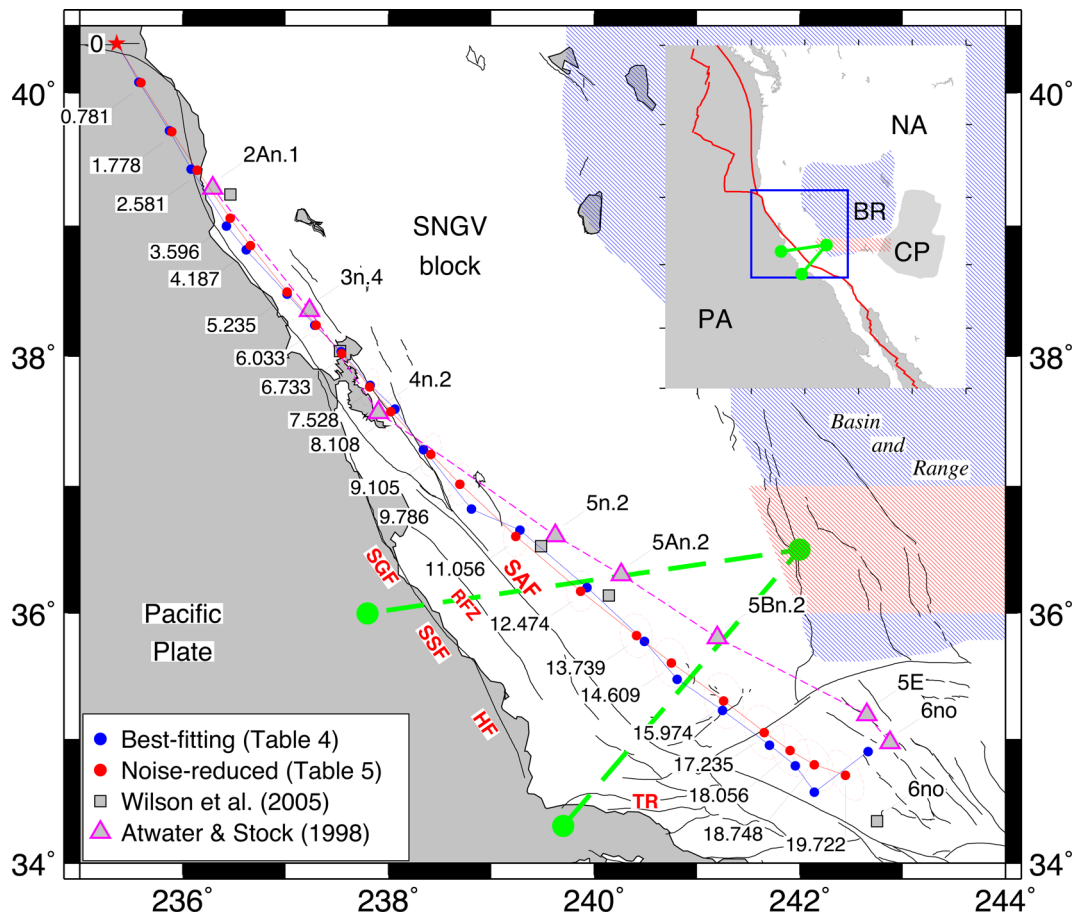
Figure 15. Positions since 19.72 Ma of a point on the Pacific plate near the Mendocino Triple Junction (40.37°N, 124.64°W) relative to North America reconstructed with rotations listed in the map legend. Ages in Myr of the reconstructed points are listed along the flow line. The uncertainty ellipses are 2-D, 95 per cent. The pink patterned areas in the maps identify the 36–37°N Basin and Range transect for which McQuarrie & Wernicke (2005) estimate 235±20 km of N78°W extension since 16 Ma. The green lines show the locations of two plate boundary transects discussed in the text. Abbreviations: BR, Basin and Range; CP, Colorado Plateau; HF, Hosgri Fault; NA, North America plate ; PA, Pacific plate; RFZ, Reliz-Rinconada fault zone; SAF, San Andreas Fault; SGF, San Gregorio Fault; SSF, San Simeon Fault; TR, Transverse Ranges.

Dickinson *et al.* (2005) estimate a total offset of 156±4 km for the Hosgri-San Gregorio fault zone, all during the past 12 Myr. Similarly, Langenheim *et al.* (2013) estimate 148–154 km of total offset based on a reconstruction of well-mapped magnetic sources that are offset by the fault. For the Reliz-Rinconada Fault, Graham (1978) estimates a post-early Miocene (i.e. post-16-Myr) offset of 43±4 km, consistent with a more recent 40-km estimate based on magnetic sources that are offset by the fault (Langenheim *et al.* 2013). Summing these with the offsets for the San Andreas Fault and Basin and Range gives 699±20 km of post-16-Ma displacement parallel to N40°W (see Transect N in Fig. 16b).

The southernmost transect crosses the Transverse Ranges of southern California (Fig. 16a). From reconstructions of the well-measured fault offsets and block rotations of the Transverse Ranges, Dickinson (1996) and Dickinson & Wernicke (1997) estimate that 208±22 km of distributed transrotational shear parallel to the plate margin has occurred since 16 Ma (Fig. 16b). Summed with the 500±19 km of post-16 Ma offset for the San Andreas Fault and Basin and Range, 708±29 km of margin-parallel displacement is indicated for the southern transect.

The margin-parallel displacements estimated for the two transects, 699±20 km and 708±29 km, agree within their uncertainties, but are respectively 65±20 km and 56±29 km less than the displacement estimated with our 16.0-Myr rotation (purple vec-

tors in Fig. 16b). Deformation along other structures probably accounts for some of the residual deformation. For example, geodetic (Kreemer *et al.* 2010) and palaeomagnetic (Bryan & Gordon 1990) measurements on the Colorado Plateau indicate that it rotates slowly clockwise relative to North America. A simplistic extrapolation of the Kreemer *et al.* (2010) GPS-derived angular velocity for the plateau back to 16 Myr gives net movement of 24±3 km towards N48°W at the SW corner of the plateau, or 24±3 km when projected onto the N40°W margin-parallel direction. Subtracting this from the residual displacements for the two transects reduces the residual displacements to only 32-41 km, representing only ∼5 per cent of the 764±9 km of margin-normal plate displacement since 16.0 Myr. Minor deformation along other structures and inaccuracies in our C5Cn.1 rotation and the magnitude and/or direction of Basin and Range deformation estimated by McQuarrie & Wernicke (2005) most likely account for the rest.

5.6 20 Ma-to-present motion along Canada's western margin

Numerous studies of the 700-km-long Queen Charlotte Fault and adjacent continental margin of western Canada (Fig. 17) have interpreted their tectonic histories based partly on the assumption that a
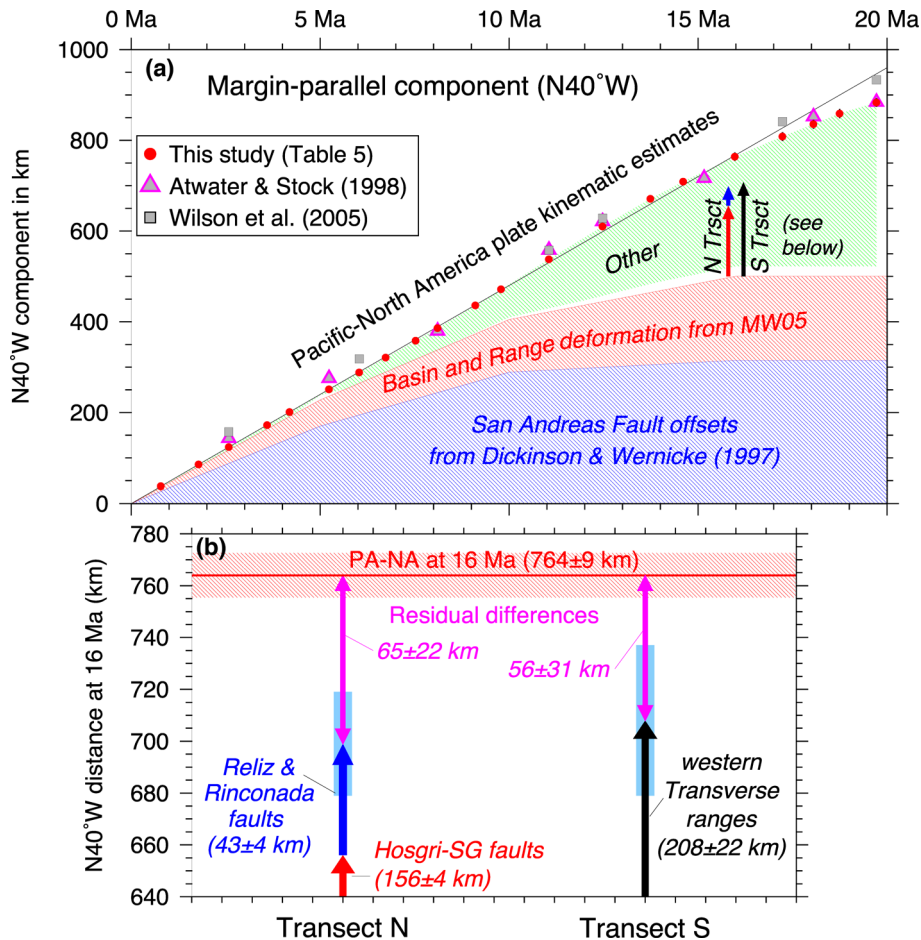
Figure 16. Time-series of plate kinematic and geologic estimates of the margin-parallel component of Pacific–North America (PA–NA) plate motion, western United States. (a) Boundary-parallel displacement components along the flow lines from the previous figure compared to geologic estimates of offsets along the San Andreas Fault (blue line) and deformation across the Basin and Range province (McQuarrie & Wernicke 2005; abbreviated MW05 in the figure). Arrows labelled 'N Trsct' and 'S Trsct' denote geologic offsets of structures crossed by the two plate boundary transects shown by the dashed green lines in Fig. 15. (b) Close-in view from Panel a of the margin-parallel displacement component estimated with our C5Cn.1 finite rotation (15.97 Ma) versus the cumulative offsets at 16 Ma for the San Andreas Fault (315±10 km), the Basin and Range Province (185±16 km) and faults crossed by the northern and southern plate boundary transects shown in the previous figure. The 65±22 km and 56±31 km differences between the kinematic and the geologic estimates for the two transects are attributable to deformation on structures not accounted for in the figure and errors in all of the above estimates. The pink bar shows the 1σ uncertainty in the plate kinematic estimate. The blue bar shows the combined 1σ uncertainty for the geologically determined offsets.

$\sim 20°$ clockwise rotation of the Pacific–North America slip direction occurred at or after 6 Ma (i.e. Hyndman & Hamilton 1993; Rohr & Currie 1997; Smith *et al.* 2003; Rohr & Tryon 2010; Hyndman 2015). Below, we present a revised flow line and velocity history for Canada's western margin and briefly discuss their implications.

5.6.1 Flow line comparison to the Queen Charlotte Fault: continental deformation

Fig. 17(a) shows an 830-km-long flow line reconstructed with our Table 5 rotations for a point on the Pacific plate presently at the north end of the Queen Charlotte Fault. For ages of 19.72–12.47 Ma, the flow line is parallel and close to the well-mapped Queen Charlotte Fault, the present-day plate boundary (compare black and red lines in Fig. 17a). On average, the points on the reconstructed flow line for these ages are located only 1.1 km from adjacent points on the Queen Charlotte Fault. The simplest (though not only) interpretation of the close proximity of the two is that the Queen Charlotte Fault directly west of the Haida Gwaii archipelago has accommodated all of the plate motion since 19.7 Ma. By implication, any shortening

of the North America plate inland from Haida Gwaii has been small (several km) or possibly zero since 20 Ma. Our analysis is relatively insensitive to possible upper plate deformation with a component parallel to the present plate boundary and thus does not preclude along-strike movement of Haida Gwaii or other crustal slivers.

Beginning at 12.47 Ma, the reconstructed flow line curves gradually clockwise, similar to the clockwise changes in the orientations of the Queen Charlotte Fault and continental slope (Fig. 17a). The similarity in the traces of the present continental margin and the flow line may indicate that the continental margin has been actively modified in response to the northward passage of the Pacific plate and the accompanying Yakutat block since 20 Ma. The observation that the Queen Charlotte Fault is located progressively farther east of the flow line for ages of 0 to 12.47 Ma, reaching a maximum difference of $\approx 25 \pm 8$ km (1σ) at flow-line ages of 9–8 Ma (Fig. 17a), suggests that the trace of the plate boundary has either jumped eastwards since ≈ 10 Ma or areas of North America inland from this portion of the flow line have accommodated $\approx 25 \pm 8$ km (1σ uncertainty) of boundary-normal shortening since ≈ 10 Ma. In support of the latter, GPS measurements in western Canada suggest
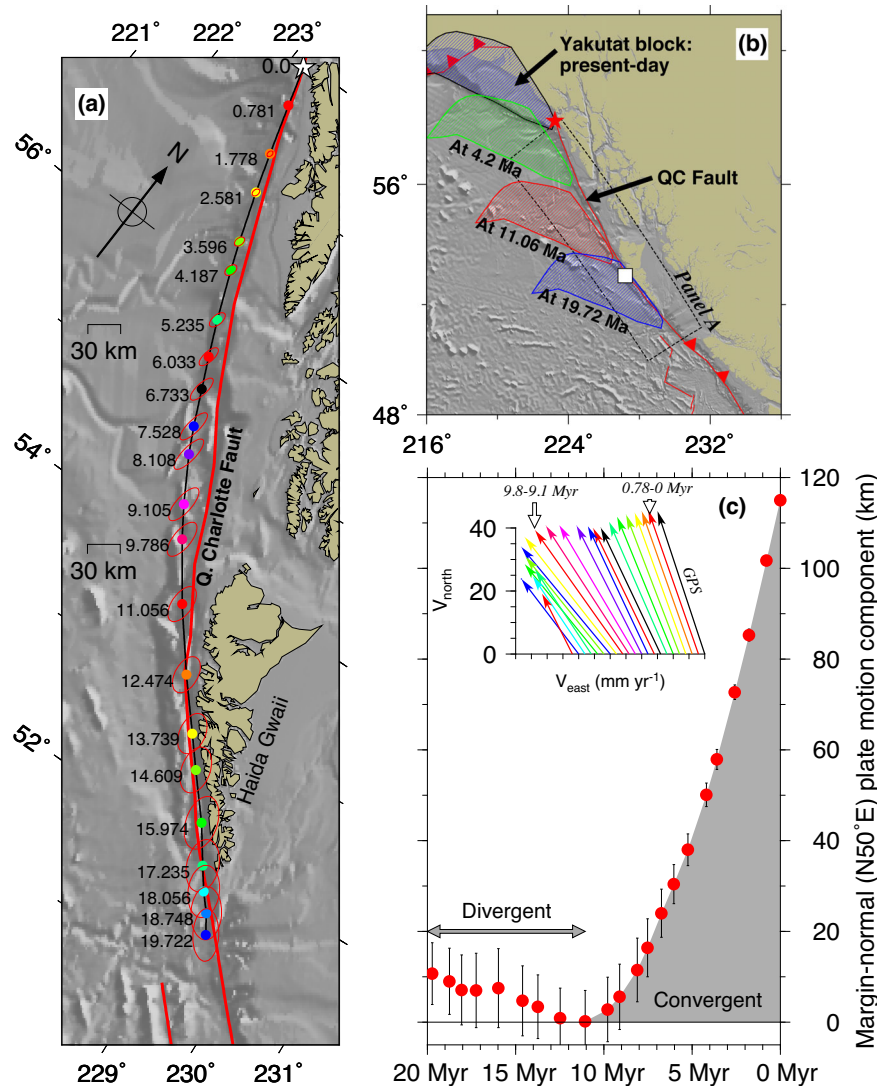
Figure 17. Pacific–North America motion along the Queen Charlotte Fault offshore from western Canada, 19.7 Ma to present. (a) Flow line reconstructed with Table 5 rotations for a point presently at the northern end of the Queen Charlotte Fault/southern edge of the Yakutat Block (star and solid black line). Ages in Myr are labelled to the left of each reconstructed point. Red line demarcates the trace of the Queen Charlotte Fault. The ellipses show the 2-D, 95 per cent reconstruction uncertainties. (b) Palaeolocations of the Yakutat Block reconstructed at C3n.1 (4.2 Ma), C5n.2o (11.06 Ma) and C6no (19.72 Ma) assuming the block has travelled with the Pacific plate to the present. (c) Reconstructed component of the estimated plate motion perpendicular to the N40°W-striking Queen Charlotte Fault offshore Haida Gwaii at 53.0°N, 132.8°W (square in Panel b) and 1σ uncertainties. The inset velocity diagram shows interval velocities from 19.72 Ma to the present (left to right) estimated with the Table 6 angular velocities and the GPS angular velocity from Table 1.

that 1–2 mm yr^{-1} of NE-directed shortening presently occurs in areas inland from this part of the flow line (Mazzotti *et al.* 2008; Elliott *et al.* 2010), close to the ≈2–3 mm yr^{-1} 10-Ma-average rate suggested by our flow-line analysis.

5.6.2 *Yakutat terrane reconstructions*

Given that the Yakutat terrane of southeastern Alaska also translated along Canada's western margin during the past 20 Myr (e.g. Bruns 1983), we reconstructed its palaeolocations at selected times assuming for simplicity that the terrane travelled with the Pacific plate (Fig. 17b). The palaeopositions of the terrane's eastern, inland boundary, which is presently defined by the Fairweather Fault of southeastern Alaska, are parallel or sub-parallel with the continental margin for all times back to 20 Ma, implying that the interaction between the Yakutat block and Canada's western margin may have

been dominated by margin-parallel shear for the past 20 Myr. Our newly estimated rotations give well-constrained limits on the southernmost possible location of the Yakutat terrane since 19.7 Myr (Fig. 17b), but do not resolve whether the terrane has travelled only a few hundred km from an origin north of Haida Gwaii (Perry *et al.* 2009) or has instead travelled more than 1000 km from a location along the Cascadia margin (e.g. Plafker *et al.* 1994).

5.6.3 *Timing of Pacific–North America motion change: western Canada*

Along the plate boundary west of the Haida Gwaii archipelago, the Table 6 angular velocities indicate that the plate slip direction was parallel to the Queen Charlotte Fault before 12.47 Ma, but has rotated progressively clockwise since 12.47 Ma to a present convergence obliquity of 21° ± 1.2° (Fig. 18b). The instantaneous rate
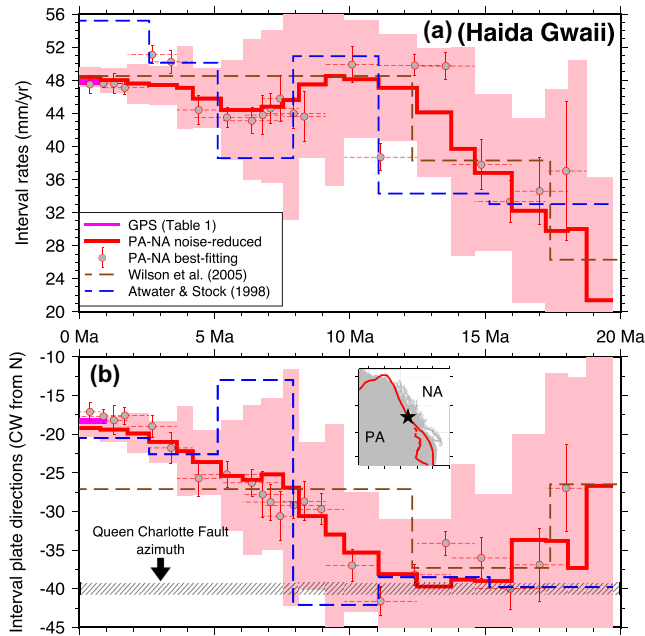
Figure 18. Pacific–North America interval rates (a) and slip directions (b) at 53.0°N, 132.8°W on the Queen Charlotte Fault (star in the inset map) estimated with angular velocities specified in the legend. The horizontal dashed lines show the time intervals spanned by the best-fitting angular velocities. Pink-shaded region shows the 1σ uncertainties propagated from the angular velocity covariances.

and direction given by our newly estimated GPS angular velocity (Table 1) differ by only 0.6 mm yr⁻¹ and 0.9° from those estimated with our 0.78-Myr-to-present angular velocity (Figs 17c and 18). The geologically recent motion along the plate boundary near Haida Gwaii thus appears to be accurately determined.

Our newly estimated Pacific–North America rotations thus indicate that the plate motion west of Haida Gwaii first acquired a convergent component of motion at 12–11 Ma (Fig. 18b), five to eight million years earlier than dates assumed by numerous previous authors based on previous kinematic estimates of Pacific–North America plate motion (Hyndman & Hamilton 1993; Rohr & Currie 1997; Smith *et al.* 2003; Rohr & Tryon 2010; Hyndman 2015). Our angular velocities also indicate that the slip direction has rotated steadily more clockwise since 12.47 Ma. The rate of the margin-normal convergent component of the plate motion has increased correspondingly to a present value of 17±1.3 mm yr⁻¹.

5.6.4 Implications for underthrusting versus upper plate shortening

Based on our new rotations, the cumulative boundary-normal convergent component of the plate motion west of Haida Gwaii has increased from zero at ≈12 Ma to 115±7 km at present (Fig. 17c). If shortening of the overlying North America plate had accommodated all of the estimated convergence, the present continental slope and Queen Charlotte Fault would be located 115 km inland from the reconstructed flow line west of Haida Gwaii. Both features instead coincide with the flow line (Fig. 17a). We infer that subduction of the Pacific plate beneath Haida Gwaii has accommodated most or all of the margin-normal component of motion.

Modelling of gravity data (Hyndman 2015) and receiver function analyses of seismic data from Haida Gwaii (Bustin *et al.* 2007; Gosselin *et al.* 2015) are consistent with Pacific plate underthrusting of
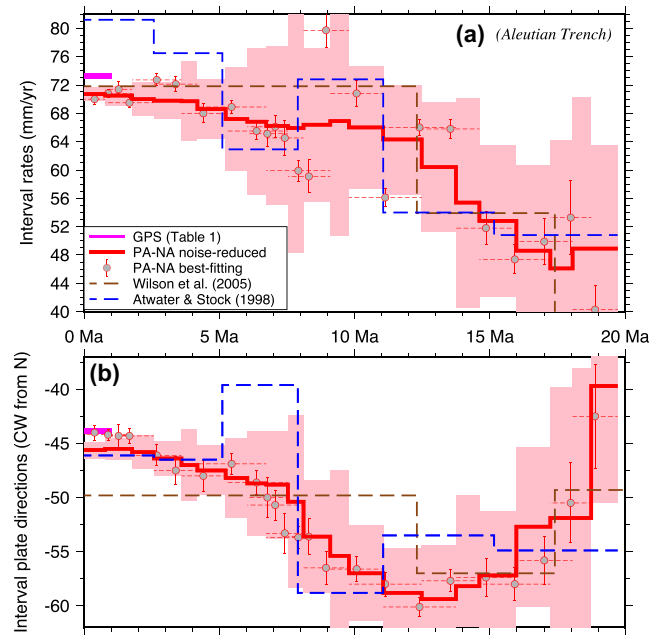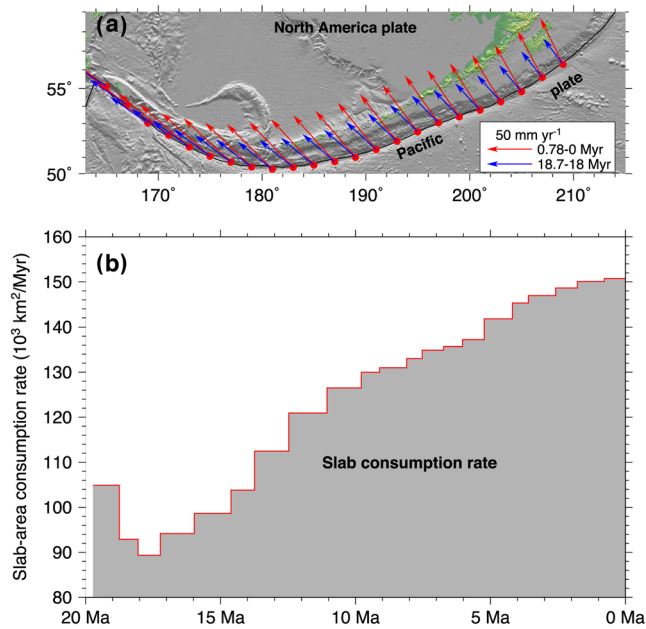

Figure 19. Pacific–North America (PA–NA) interval rates (a) and slip directions (b) along the Aleutian Trench (51.0°N, 180.0°E) estimated with angular velocities from sources specified in the legend. The horizontal dashed lines show the time intervals spanned by the best-fitting angular velocities. Pink-shaded region shows the 1σ uncertainties propagated from the angular velocity covariances.

the Haida Gwaii archipelago to depths of ≈40 km and to horizontal distances 65–70 km inland from the Queen Charlotte Fault. From gravity and seismic constraints shown in fig. 8 of Hyndman (2015), we estimate that ≈70 km of the Pacific plate has underthrust the continent. Although this agrees to first order with our 115±7 km kinematic estimate, the 45±7 km discrepancy between the two may indicate that the tectonic history along this part of the margin is more complicated than envisioned in our simple model or that the amount of underthrust Pacific plate and/or uncertainties in our rotations are underestimated.

Models that exclude an underthrust Pacific slab also fit the gravity observations from Haida Gwaii (Rohr *et al.* 2000). Such models, however, require the upper plate to have accommodated 115±7 km of boundary-normal shortening, contrary to the ≈1-km correspondence between the reconstructed flow line and present plate boundary west of Haida Gwaii.

5.7 Implications for Aleutian arc subduction

Along the Aleutian Trench, our angular velocities (Table 6) indicate that convergence rates have increased ≈50 per cent and rotated ≈15° clockwise since 19.7 Ma (Fig. 19). The convergence rates estimated with the Atwater & Stock (1998) and Wilson *et al.* (2005) rotations also increase by ≈50 per cent since 20 Ma (blue and brown dashed lines in Fig. 19a). The convergence directions, however, differ significantly. Whereas the Atwater & Stock (1998) rotations suggest that the direction of convergence rotated ≈20° clockwise at 7.9 Ma, our angular velocities indicate only a 3° change in direction at 7.8 Ma as part of a more gradual 15° clockwise change in the direction since 15 Ma. The instantaneous rate and direction estimated with our GPS angular velocity (pink lines in Fig. 19) corroborates our 0.78-Myr-to-present estimates.

Figure 20. (a) Pacific–North America interval velocities along the Aleutian trench and Alaska subduction zone from 0.78 Ma to the present (red) and 18.75 to 18.06 Myr (blue) from angular velocities in Table 6. (b) History of Pacific plate, slab-area subduction rate reconstructed from Table 6 angular velocities. The total slab area subducted per Myr between the western end of the Aleutian trench and 210°E was determined by calculating the interval convergence velocities at the midpoints of 23 equal-length trench segments with the Table 6 angular velocities, projecting each convergence velocity onto the trench-normal direction for each trench segment, multiplying the trench-normal velocity component per segment by the corresponding segment length, and summing the slab consumption rates for all 23 segments. The red circles in Panel a show the segment centre points.

The gradual change from slower, more oblique subduction before 15 Ma to faster, less oblique subduction at present (Fig. 20a) requires that more Pacific plate is now subducted per unit time than was the case at 18 Ma. Based on the Table 6 angular velocities, Fig. 20(b) shows the area of the Pacific plate that has been consumed by Aleutian Trench subduction per unit time since 20 Ma as estimated using the trench-normal velocity components for 23 equal-length segments along the trench. The slab-area consumption rate has increased by nearly 70 per cent since 20 Ma.

If the rate of subduction governs the flux of water into the mantle above a subducting plate (Davies & Bickle 1991), which in turn determines the magma production rate along an arc (Grove *et al.* 2012), then the estimated ≈70 per cent increase in the slab consumption rate since 20 Ma should have increased the volume of Aleutian arc magmatism through time. Testing for this increase will be challenging. Although Jicha *et al.* (2006) describe evidence for apparent pulses of Aleutian whole-arc magmatism at 16–11 Ma and 6–0 Ma, we were unable to locate other estimates of the magma production rates for the Aleutian arc.

6 UNCERTAINTIES AND ROBUSTNESS OF RESULTS

6.1 Timing and duration of a Late Neogene change in Pacific–Antarctic plate motion

Given that Pacific–Antarctic plate motion is 2–3 times faster than for the Nubia–North America and Nubia–Antarctic plate pairs (e.g.

Fig. 7) and the motions of the latter two plate pairs have been steady for much of the past 10 Myr, changes in Pacific–Antarctic plate motion since 10 Ma have mapped nearly one-to-one into changes in Pacific–North America plate motion (Fig. 7). As a consequence, our Pacific–North America plate motion estimates are sensitive to possible inaccuracies in our estimates of Pacific–Antarctic plate motion. In this regard, Cande *et al.* (1995) propose that the Pitman fracture zone and adjacent seafloor fabric rotated abruptly clockwise by 5°–8° at 5.9 Ma, significantly different than the steady changes estimated with our REDBACK and the Croon *et al.* best-fitting rotations (Fig. 5b). Austermann *et al.* (2011) propose an even larger-magnitude, 10°–13° abrupt change at ≈6 Ma. We thus examined in more detail the evidence for a rapid change in motion.

The primary evidence cited by Cande *et al.* (1995) for the abrupt change in direction is a change in the azimuths of abyssal hills adjacent to the Pitman Fracture Zone on seafloor just older and younger than 5.9 Ma (see their fig. 8). In our view, the numerous abyssal hill azimuths shown in their figure are equally well fit by a gradual clockwise directional change between 13 Ma and the present. In support of this interpretation, we note that the instantaneous Pacific–Antarctic slip direction estimated at the Pitman Fracture Zone with the GEODVEL GPS-based angular velocity (Argus *et al.* 2010) is oriented ≈5° clockwise from the slip direction at 5 Ma (Fig. 5b). Geodetic measurements are thus consistent with sustained clockwise rotation of the slip direction since at least 5 Ma.

The abrupt, 10°–13° clockwise change at 5.9 Ma proposed by Austermann *et al.* (2011) is based on their best straight-line fits to segments of the Pitman Fracture Zone that abut seafloor younger and older than 5.9 Ma (see their fig. 1). We note, however, that the well-mapped fracture zone trace and abyssal hill fabric also clearly show continued clockwise changes up to the present, consistent with a gradual rather than abrupt change in direction. Multibeam surveys of the sparsely mapped fracture zones along the southwestern portion of the Pacific–Antarctic Rise, which are near the pole of rotation and thus sensitive to even small changes in the pole location, could be used to test whether the pole has migrated gradually or via occasional, discrete jumps.

6.2 Sensitivity to corrections for outward displacement

The corrections for outward displacement that were applied to the plate-circuit finite rotations (Section 3.4) were determined empirically and are thus a likely source of rotation noise. Based on the scatter of localized versus boundary-wide estimates of outward displacement that are reported by Merkouriev & DeMets (2008, 2014) and DeMets *et al.* (2015b), we estimate that the calibrations for outward displacement that were applied for this analysis contribute an additional ±1 km uncertainty to the opening distances that are estimated with our finite rotations. These uncertainties are not formally incorporated into the finite rotation covariances in Table 5. Over- or under-rotations of 1-km or less for points that are reconstructed with finite rotations are unlikely to be of major consequence for most users and are thus ignored here.

Except for the angular velocity/finite rotation that describes motion from 0.78 Ma to the present, the impact on our angular velocity estimates of errors in our calibrations for outward displacement is negligible because any such errors cancel when finite rotations of different ages are differentiated to estimate angular velocities. We evaluated the impact of an error in the correction for outward displacement on our estimate of 0.78 Ma-to-present Pacific–North America plate motion as follows: We first derived Pacific–Antarctic

best-fitting rotations calibrated for an assumed 1-km of outward displacement instead of the 2-km calibration that is described in Section 4.1. We then used REDBACK to estimate their corresponding, noise-reduced Pacific–Antarctic rotations and propagated the noised-reduced rotations through the global circuit to determine alternative Pacific–North America rotations and angular velocities. At key locations along the Pacific–North America plate boundary, the alternative Pacific–North America angular velocities give 0.78-Myr-to-present velocities that differ by only 0.1 to 0.6 mm yr^{-1} and 0.3 to 0.6° from the velocities estimated with the preferred angular velocities (Table 6). The velocities for times older than 0.78 Ma agree to within 0.1 mm yr^{-1} and 0.2°.

None of the changes above are large enough to alter our primary results or interpretations. We conclude that our results are robust with respect to modest (∼1 km) errors in the corrections that were applied to the plate circuit rotations for outward displacement.

6.3 Effect of spline-smoothing versus Bayesian methodology

As a test of the robustness of our new plate kinematic rotations with respect to the Bayesian method that was used to determine the Pacific–Antarctic, Antarctic–Nubia, and Nubia–North America noise-reduced rotations, we derived alternative, smoothed rotations from the best-fitting rotations for all three circuit plate pairs using a cubic spline method described by Hanna & Chang (2000). Successful application of the spline-smoothing methodology requires the user to identify an optimal value for a spline smoothing parameter. Three alternative methods are available for estimating the best smoothing parameter. Two of these, the 'cross-validation' and 'discrepancy' methods described by Hanna & Chang (2000), employ different statistical assumptions about the nature of the rotation variances in order to optimize the smoothing parameter. A third method not described in Hanna & Chang (2000), but incorporated into their spline-smoothing software, requires the smoothed rotations to lie inside the confidence region of their corresponding, original rotation. We refer to this method below as the 'confidence regions' method.

Using the 21 Nubia–North America best-fitting rotations as our input, we applied all three splining methods to find spline-smoothed rotations. We gauged the success of the methods by evaluating how well each method reduced the scatter in the estimated poles and stage velocities relative to that associated with the original, best-fitting rotations and angular velocities (Figs 21 and 22). We focused in particular on whether a given method successively reduced or eliminated obvious examples of spurious noise in the best-fitting rotations such as the highly discrepant best-fitting poles for Chrons 2An.3 and 5n.1 (Fig. 21a) and the spurious stage rates for 4.2–3.6 Ma and 14.6–13.7 Ma (Fig. 22a).

The 'discrepancy' method failed both of the above tests (Figs 21b and 22) and was the least effective at reducing noise in the rotations. In contrast, the 'confidence-regions' and 'cross-validation' spline-smoothing methods both defined smoother pole paths than did the discrepancy method (compare Figs 21b–d) and more smoothly varying stage velocities (black and blue lines in Fig. 22). In particular, the stage velocities determined from rotations that we derived using the 'cross-validation' method change smoothly at 14.6–13.7 Ma and 4.2–3.6 Ma (Fig. 22), whereas the rotations determined via the 'confidence-regions' method indicate less plausible, abrupt velocity changes for both intervals (Fig. 22a).

The Bayesian methodology yields the simplest pole path of any of the methodologies; the path described by the noise-reduced poles has only one sharp bend (Fig. 21e), whereas all three spline-derived rotation sequences describe more complex, two-bend pole paths. Although the stage velocities estimated with the Bayesian angular velocities (red line in Fig. 22) are clearly less noisy than for two of the three spline-smoothed methods, the Bayesian and cross-validation stage velocities (blue line in Fig. 22) are similar.

As might be expected, the different rotation sequences are associated with different fitting penalties relative to the optimized, least-squares fit of the original best-fitting rotations. Rotations for the least effective spline-smoothing method, namely, the discrepancy method, fit the original Nubia–North America reversal and fracture zone crossings only 4.5 per cent worse than did the best-fitting rotations. The other two spline-smoothing methods were associated with larger fitting penalties (17.1 per cent and 18.5 per cent) and the Bayesian rotations had the largest fitting penalty (25.7 per cent). The association of increasingly large fitting penalties with increasing simple rotation sequences reflects the expected trade-off between model simplicity and data fit. DeMets *et al.* (2015a,b) report that the Bayesian rotations for the Nubia–North America and Nubia–Antarctic plate pairs increased the average reconstruction misfits by only 100–300 m relative to the fits of the best-fitting rotations, smaller than the potential systematic errors in the underlying magnetic reversal and fracture zone data. They conclude that the fitting penalty introduced by the Bayesian noise method constitutes an acceptable trade-off given the more plausible plate kinematic history that is estimated with the Bayesian rotations.

Using the cross-validation method, we estimated spline-smoothed rotations for the Nubia–Antarctic and Pacific–Antarctic plate pairs and combined them with the spline-smoothed Nubia–North America rotations to estimate Pacific–North America rotations. The spline-smoothed Pacific–North America poles migrate from north-to-south during the past 20 Myr in a manner similar to the best-fitting and Bayesian pole sequences (Supporting Information Fig. S3). All but one of the spline-smoothed estimates of Pacific–North America stage rates and directions agree with their Bayesian counterparts within their 1σ uncertainties (Supporting Information Fig. S4). We conclude that the noise-reduced results cited throughout the paper are robust with respect to the Bayesian method that was used to reduce noise in the best-fitting rotations. The 1–2 mm yr^{-1} and 1°–2° differences between the Bayesian and spline-smoothed stage velocities (Supporting Information Fig. S4) suggest a practical lower bound on the accuracy of the stage rates and directions that can be determined from our data.

6.4 Possible limitations due to data biases, plate non-rigidity and thermal contraction

Although we took care throughout the analysis to validate our newly estimated plate kinematic results against independent geodetic, geological, structural, and geochronological observations that variously constrain the magnitude and timing of Pacific–North America plate boundary deformation for times from the present back to 16 Ma (e.g. Figs 9, 13, 16 and 17), some caution is warranted in interpreting the agreements and differences between the two.

For example, the apparent, good agreement between our plate kinematic and independent structural and geodetic estimates of plate motion across the northern Gulf of California since 6.2 Ma (Section 5.4.2) depends partly on the accuracy of the Plattner *et al.* (2007) geodetic estimate of the Baja Peninsula angular velocity. A recently
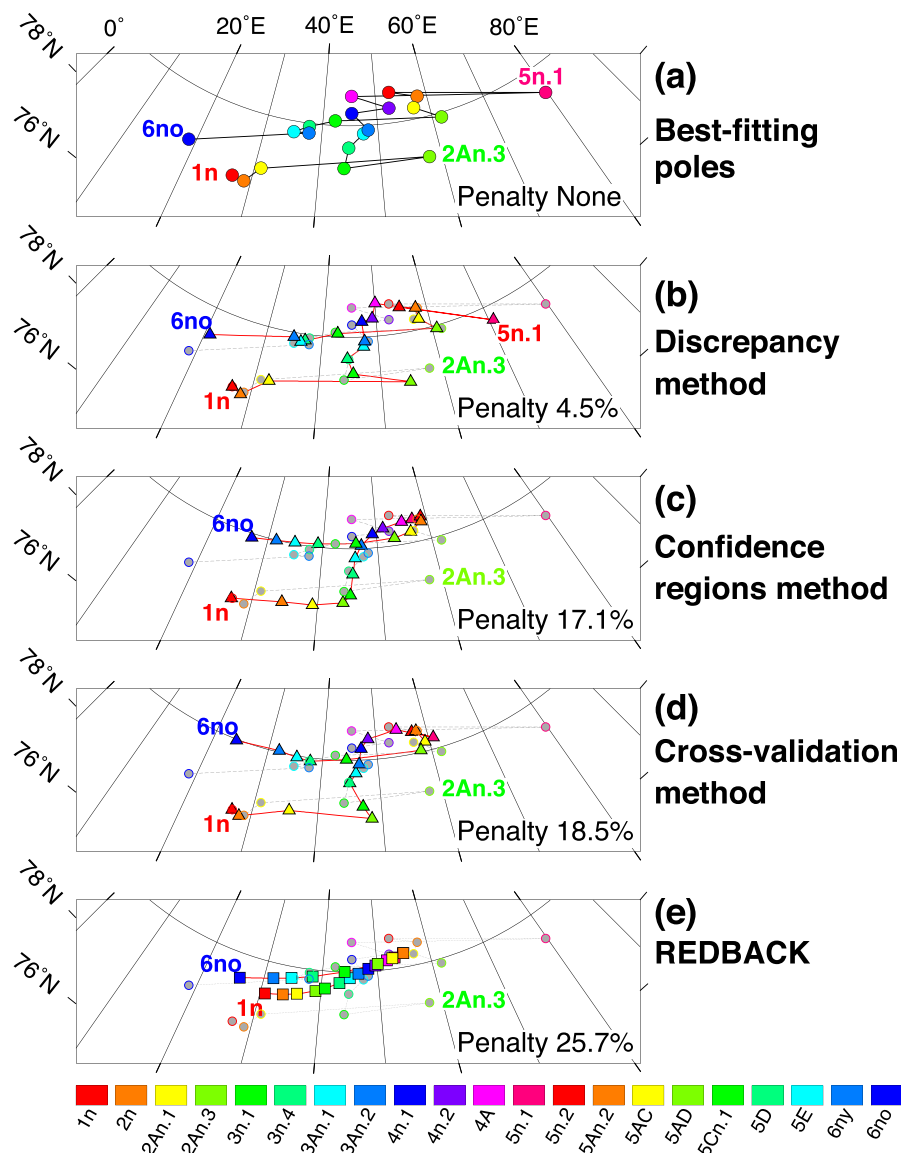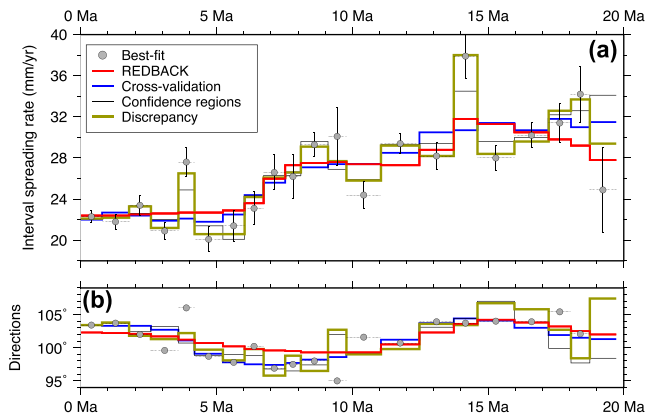
Figure 21. Comparison of best-fitting Nubia–North America finite rotations (Panel a and circles in Panels b–e) to alternative rotation estimates shown in Panels b–e. 'Penalty' denotes the percentage increase in the least-squares misfit of each set of rotations to the Nubia–North America data relative to the misfit of the best-fitting rotations (see the text). Poles shown in Panels b and d were derived via the discrepancy and cross-validation cubic spline methods for smoothing a series of noisy rotations (Hanna & Chang 2000). Poles in Panel c were derived using a spline-smoothing method that requires the smoothed rotations to lie within their 3-D confidence regions. (e) Poles and fitting penalty for REDBACK noise-reduced rotations estimated by DeMets *et al.* (2015a) using the Bayesian method described by Iaffaldano *et al.* (2012).

published velocity estimate for continuous GPS site MSD1 in the southern Baja peninsula relative to an updated Pacific plate frame of reference (DeMets *et al.* 2014a) is a factor of two slower than expected based on Plattner *et al.*'s results. An updated analysis that uses all continuous and campaign GPS data from the Baja Peninsula and Pacific plate and that calibrates for the interseismic elastic and post-seismic viscoelastic effects of the rapidly slipping faults in the nearby Gulf of California is needed.

The persistent discrepancy between our new geologic estimates of Pacific–North America plate motion and numerous geodetic estimates, including our own (Figs 6 and 9), offers a further cautionary note about possible systematic biases and/or inaccuracies in the geodetic and/or geologic estimates. Our geologic rotations could be negatively impacted by possible tectonic deformation within one of

the four plates in the global plate circuit, a systematic bias in one or more subsets of the plate kinematic data from the three plate circuit boundaries, or thermal contraction of cooling seafloor (Kumar & Gordon 2009; Kreemer & Gordon 2014). Significant 1–1.5 mm yr^{-1} southward motions of two GPS island sites on young seafloor on the eastern Pacific plate towards older parts of the Pacific plate interior may indicate that thermal contraction is rapid enough to affect plate motion estimates at a detectable level (DeMets *et al.* 2014a). Our calibration for outward displacement implicitly removes most or all of any ridge-normal component of thermal contraction that might degrade our young rotations. Seeking evidence for the horizontal contractional effects of thermal cooling to better understand its limiting effects on the accuracy of plate reconstructions remains at the cutting edge of plate tectonic research.

Figure 22. Comparison of Nubia–North America interval velocities based on different methods for reducing noise in or smoothing the underlying best-fitting finite rotations. Panels a and b show the estimated interval seafloor spreading rates and slip directions, respectively. The best-fitting and RED-BACK interval velocities are estimated with angular velocities from DeMets *et al.* (2014a, 2015a). The other interval velocities are estimated with angular velocities we determined from smoothed finite rotations that we derived using the cross-validation and discrepancy cubic spline methods of Hanna & Chang (2000) and from an alternative spline-smoothing method discussed in the text. Velocities are estimated at 27.6°N, 44.4°W, near the geographic centre of the plate boundary. Uncertainties are omitted for clarity.

7 CONCLUSIONS

From rotations that reconstruct Pacific–Antarctic, Antarctic–Nubia, and Nubia–North America plate motions at 21 times between 19.7 and 0.78 Ma, we estimate new, high-resolution rotations that describe Pacific–North America plate motion at ≈1-Myr intervals since 20 Ma. We extend the kinematic estimates to the present using the velocities of 935 GPS sites on the Pacific and North America plates. Methodologically, our rotations differ from previous estimates in several respects. The new reconstructions are spaced more closely than for previous studies, thereby reducing the likelihood of kinematic artefacts due to undersampling of the plate motion history. Bayesian analyses of the noisy best-fitting rotations for all three of the circuit plate pairs indirectly reduce noise in the Pacific–North America rotations, giving a more plausible and hopefully more accurate description of the plate motion history. Finally, all of the rotations are calibrated for outward displacement, an important source of systematic bias in rotations for the youngest times.

The new high-resolution sequence of Pacific–North America rotations defines a relatively simple Neogene-to-recent plate motion history in western North America, consisting of a ≈70 per cent speed-up in relative motion from 19.7 to 9±1 Ma, a rate of motion that has varied by less than ±2 per cent for the past 8 Myr, and a progressive ≈25° clockwise rotation of the plate slip direction during the past 20 Ma, with a possible hiatus from 9–5 Ma. Relative to previously published estimates, the estimated stage velocities vary more smoothly and exhibit no evidence for a previously reported 20°–25° clockwise change in the plate slip direction at ≈8 Ma (Atwater & Stock 1998) or a proposed clockwise change in motion at 6 Ma (Austermann *et al.* 2011).

Comparisons of the plate motion estimated with the new Pacific–North America rotations and their associated angular velocities to a variety of independent observations give the following results:

(1) The 0.78-Myr average velocity estimated with our new rotations at a fiducial point in central California differs an insignificant 1.6 ± 1.7 mm yr^{-1} from that estimated with our GPS angular velocity

(Fig. 9b). The good agreement between these independent estimates confirms that the rate of motion has remained steady since 8 Ma, but that the direction has rotated 7°–8° clockwise during this period.

(2) The velocities estimated with our stage rotations for all periods during the past 3.6 Myr differ significantly from that estimated with the 3.16-Myr-average MORVEL angular velocity. Two simple modifications to the MORVEL data that are warranted by recently published studies, however, give rise to a modified MORVEL angular velocity that gives plate motion that differs insignificantly from our new estimates (Fig. 9b).

(3) Our new rotations indicate that Pacific plate motion relative to the Sierra Nevada microplate first became obliquely convergent with respect to the San Andreas Fault in central California at 5.2–4.2 Ma, consistent with Pliocene ages estimated from geological observations for the onset of folding and faulting in central California. A gradual clockwise change in the plate slip direction is thus implicated as the cause of the orogeny. The magnitude of the estimated fault-normal shortening since 4.2 Ma, 24 ± 5 km (1σ), agrees within its uncertainties with 12–33 km geological estimates of the total boundary-normal contraction and with the total shortening extrapolated from fault-normal rates of contraction measured with GPS.

(4) 6.3-Ma-to-present Pacific–North America displacement extrapolated from our C3An.1 (6.03 Myr) finite rotation differs by as little as 15 ± 22 km from the cumulative 6.3-Ma-to-present displacement estimated from structural and palaeomagnetic studies of the northern Gulf of California and extrapolated from GPS measurements of the present motion between the Baja California Peninsula and Pacific plate (Plattner *et al.* 2007). From this agreement, we estimate an approximate upper limit of 10–30 km for the effects of plate non-rigidity integrated around the global plate circuit for the past 6.3 Ma.

(5) Similar comparisons of vector displacements for the past 12 Myr from our own and structural reconstructions of the northern and southern Gulf of California and its deforming margins yield respective differential vectors of 200 ± 54 km and 68 ± 59 km. We interpret the 200 ± 54 km structural slip deficit as evidence that a significant fraction of the plate motion from 12 to 6.3 Ma was accommodated by faults in northwestern Mexico and/or the palaeo-subduction fault and abandoned spreading centres west of the Baja Peninsula (Michaud *et al.* 2006). We interpret the 68 ± 59 km structural slip deficit as evidence that most or all of the plate motion in the southern Gulf of California has been confined to faults within the Gulf since 12 Myr, in accord with geological evidence.

(6) Our Pacific–North America rotations give 16-Myr-to-present finite displacements that exceed by only 65 ± 20 km and 56 ± 29 km the integrated geological offsets of faults crossed by two transects of the western United States, including the San Andreas Fault, the central Basin and Range, and variously the Transverse Ranges of southern California and other strike-slip faults in central California. Rotation of the Colorado Plateau, which is not accounted for in the structural summation, may account for up to half of the 60 km of missing motion, with the remainder accounted for by some combination of errors within the global plate circuit, errors in the geological estimates of fault offsets, and other deformation not included in our structural summation.

(7) A 20-Myr-to-present flow line reconstructed with the new rotations for the west coast of Canada closely reproduces the trace of the present Queen Charlotte Fault and continental margin. We hypothesize that the shape of the plate margin has been influenced by the passage of the Pacific plate and accompanying Yakutat terrane. Our kinematic analysis suggests that any margin-normal shortening

of the North America plate since 20 Ma has been zero within uncertainties in areas located inland from Haida Gwaii and 25±8 km in areas north and northeast of Haida Gwaii. A clockwise rotation of the plate slip direction previously estimated to have occurred at 8–4 Ma and widely used by previous authors to interpret the tectonic history of Canada's western margin occurred at 11±1 Ma, 5–8 Myr earlier than previously recognized. Our results also indicate that the Pacific plate has underthrust the Haida Gwaii archipelago by 115±7 km since 12–11 Ma.

(8) Along the Aleutian subduction zone, changes in the velocities estimated with our new stage rotations imply that the rate at which Pacific plate lithosphere is subducted beneath the arc has increased by ≈70 per cent since 20 Ma. This previously unrecognized subduction acceleration may imply that Aleutian arc magma production rate has increased significantly since 20 Ma.

REFERENCES

Altamimi, Z., Collilieux, X. & Metivier, L., 2011. ITRF2008: an improved solution of the international terrestrial reference frame, *J. Geodesy,* **85**(8), 457–473.

Argus, D.F., 2007. Defining the translational velocity of the reference frame of Earth, *Geophys. J. Int.,* **169,** 830–838.

Argus, D.F., 2012. Uncertainty in the velocity between the mass center and surface of Earth, *J. Geophys. Res.,* **117,** B10405, doi:10.1029/2012JB009196.

Argus, D.F. & Gordon, R.G., 2001. Present tectonic motion across the Coast Ranges and San Andreas fault system in central California, *Bull. geol. Soc. Am.,* **113,** 1580–1592.

Argus, D.F., Gordon, R.G., Heflin, M.B., Ma, C., Eanes, R., Willis, P., Peltier, W.R. & Owen, S.E., 2010. The angular velocities of the plates and the velocity of Earth's centre from space geodesy, *Geophys. J. Int.,* **180**(3), 913–960.

Atwater, T., 1970. Implications of plate tectonics for the Cenozoic tectonic evolution of western North America, *Bull. geol. Soc. Am.,* **81,** 3513–3536.

Atwater, T., 1989. Plate tectonic history of the Northeast Pacific and Western North America, in *The Eastern Pacific Ocean and Hawaii,* The Geology of North America, N, eds Winterer,, E.L., Hussong, D.M. & Decker, R.W., Geological Society of America.

Atwater, T. & Molnar, P., 1973. Relative motions of the Pacific and North American plates deduced from sea-floor spreading in the Atlantic, Indian, and South Pacific oceans, in *Proceedings of the Conference on Tectonic Problems of the San Andreas Fault System,* eds Kovach, R.L. & Nur, A., Stanford Univ. Pub. Geol. Sci. 13, pp. 136–148.

Atwater, T. & Mudie, J.D., 1973. Detailed near-bottom geophysical study of the Gorda Rise, *J. geophys. Res.,* **78,** 8665–8686.

Atwater, T. & Stock, J., 1998. Pacific-North America plate tectonics of the Neogene Southwestern United States: an update, *Int. Geol. Rev.,* **40,** 375–402.

Austermann, J., Ben-Avraham, Z., Bird, P., Heidbach, O., Schubert, G. & Stock, J.M., 2011. Quantifying the forces needed for the rapid change of Pacific plate motion at 6 Ma, *Earth planet. Sci. Lett.,* **307,** 289–297.

Aydin, A. & Page, B.M., 1984. Diverse Pliocene-Quaternary tectonics in a transform environment, San Francisco Bay region, California, *Bull. geol. Soc. Am.,* **95,** 1303–1317.

Bennett, R.A., Davis, J.L. & Wernicke, B.P., 1999. Present-day pattern of Cordilleran deformation in the western United States, *Geology,* **27,** 371–374.

Bennett, S.E.K. & Oskin, M.E., 2014. Oblique rifting ruptures continents: example from the Gulf of California shear zone, *Geology,* **42,** 215–218.

Bennett, S.E.K., Oskin, M.E. & Iriondo, A., 2013. Transtensional rifting in the proto-Gulf of California near Bahia Kino, Sonora, Mexico, *Bull. geol. Soc. Am.,* **125,** 1752–1782.

Bennett, S.E.K., Oskin, M.E., Dorsey, R.J., Iriondo, A. & Kunk, M.J., 2015. Stratigraphy and structural development of the southwest Isla Tiburon marine basin: implications for latest Miocene tectonic opening and flooding of the northern Gulf of California, *Geosphere,* **11,** 977–1007.

Bruns, T.R., 1983. Model for the origin of the Yakutat block, an accreting terrane in the northern Gulf of Alaska, *Geology,* **11,** 718–721.

Bryan, P. & Gordon, R.G., 1990. Rotation of the Colorado Plateau: an updated analysis of paleomagnetic poles, *Geophys. Res. Lett.,* **17,** 1501–1504.

Bustin, A.M.M., Hyndman, R.D., Kao, H. & Cassidy, J.F., 2007. Evidence for underthrusting beneath the Queen Charlotte margin, British Columbia, from teleseismic receiver function analysis, *Geophys. J. Int.,* **171,** 1198–1211.

Calais, E., Han, J.Y., DeMets, C. & Nocquet, J.M., 2006. Deformation of the North American plate interior from a decade of continuous GPS measurements, *J. geophys. Res.,* **111,** B06402 doi:10.1029/2005JB004253.

Cande, S.C., Raymond, C.A., Stock, J. & Haxby, W.F., 1995. Geophysics of the Pitman fracture zone and Pacific-Antarctic plate motions during the Cenozoic, *Science,* **270,** 947–953.

Chang, T., 1987. On the statistical properties of estimated rotations, *J. geophys. Res.,* **87,** 6319–6329.

Chang, T., 1988. Estimating the relative rotation of two tectonic plates from boundary crossings, *J. Am. Stat. Assoc.,* **83,** 1178–1183.

Chang, T., Stock, J. & Molnar, P., 1990. The rotation group in plate tectonics and the representation of uncertainties of plate reconstructions, *Geophys. J. Int.,* **101,** 649–661.

Chase, C.G., 1972. The *n*-plate problem of plate tectonics, *Geophys. J. R. astr. Soc.,* **29,** 117–122.

Colgan, J.P., Dumitru, T.A., Reiners, P.W., Wooden, J.L. & Miller, E.L., 2006. Cenozoic tectonic evolution of the Basin and Range Province in northwestern Nevada, *Am. J. Sci.,* **306,** 616–654.

Croon, M.B., Cande, S.C. & Stock, J.M., 2008. Revised Pacific-Antarctic plate motions and geophysics of the Menard Fracture Zone, *Geochem. Geophys. Geosyst.,* **9,** Q07001, doi:10.1029/2008GC002019.

d'Alessio, M.A., Johanson, I.A., Burgmann, R., Schmidt, D. & Murray, M.H., 2005. Slicing up the San Francisco Bay Area: block kinematics and fault slip rates from GPS-derived surface velocities, *J. geophys. Res.,* **110,** B06403, doi:10.1029/2004JB003496.

Davies, J.H. & Bickle, M.J., 1991. A physical model for the volume and composition of melt produced by hydrous fluxing above subduction zones, *Phil. Trans. R. Soc. Lond., A,* **335,** 355–364.

DeMets, C. & Dixon, T., 1999. New kinematic models for Pacific-North America motion from 3 Ma to present, 1: Evidence for steady motion and biases in the NUVEL-1A model, *Geophys. Res. Lett.,* **26,** 1921–1924.

DeMets, C. & Wilson, D.S., 2008. Toward a minimum change model for recent plate motions: calibrating seafloor spreading rates for outward displacement, *Geophys. J. Int.,* **174,** 825–841.

DeMets, C., Gordon, R.G., Stein, S. & Argus, D.F., 1987. A revised estimate of Pacific-North America motion and implications for western North America plate boundary zone tectonics, *Geophys. Res. Lett.,* **14,** 911–914.

DeMets, C., Gordon, R.G., Argus, D.F. & Stein, S., 1990. Current plate motions, *Geophys. J. Int.* **101,** 425–478.

DeMets, C., Gordon, R.G., Argus, D.F. & Stein, S., 1994. Effect of recent revisions to the geomagnetic reversal timescale on estimates of current plate motions, *Geophys. Res. Lett.* **21,** 2191–2194.

DeMets, C., Gordon, R.G. & Argus, D.F., 2010. Geologically current plate motions, *Geophys. J. Int.,* **181,** 1–80.

DeMets, C., Marquez-Azua, B. & Cabral-Cano, E., 2014a. A new GPS velocity field for the Pacific plate - Part 1: Constraints on plate motion, intraplate deformation, and the viscosity of Pacific basin asthenosphere, *Geophys. J. Int.,* **199,** 1878–1899.

DeMets, C., Marquez-Azua, B. & Cabral-Cano, E., 2014b. A new GPS velocity field for the Pacific plate - Part 2: Implications for fault slip rates in western California, *Geophys. J. Int.,* **199,** 1900–1909.

DeMets, C., Iaffaldano, G. & Merkouriev, S., 2015a. High-resolution Neogene and Quaternary estimates of Nubia-Eurasia-North America plate motion, *Geophys. J. Int.,* **203,** 416–427.

DeMets, C., Merkouriev, S. & Sauter, D., 2015b. High-resolution estimates of Southwest Indian Ridge plate motions, 20 Ma to present, *Geophys. J. Int.,* **203,** 1495–1527.

Dibblee, T.W., 1976. *The Rinconanda and related faults in the southern Coast Ranges, California, and their tectonic significance, U.S. Geological Survey Professional Paper 981*, 55 p.

Dickinson, W.R., 1996. Kinematics of transrotational tectonism in the California Transverse Ranges and its contribution to cumulative slip along the San Andreas transform fault system, *Geol. Soc. Am. Spec. Paper,* **305,** 1–46.

Dickinson, W.R. & Wernicke, B.P., 1997. Reconciliation of San Andreas slip discrepancy by a combination of interior basin and range extension and transrotation near the coast, *Geology,* **25,** 663–665.

Dickinson, W.R. *et al.*, 2005. Net dextral slip, Neogene San Gregorio-Hosgri fault zone, coastal California: geologic evidence and tectonic implications, *Geol. Soc. Am. Spec. Paper,* **391,** 1–43.

Dixon, T. *et al.*, 2000. New kinematic models for Pacific-North America motion from 3 Ma to present, II: Tectonic implications for Baja and Alta California, *Geophys. Res. Lett.,* **27,** 3961–3964.

Doubrovine, P.V. & Tarduno, J.A., 2008. A revised kinematic model for the relative motion between Pacific oceanic plates and North America since the Late Cretaceous, *J. geophys. Res.,* **113,** B12101, doi:10.1029/2008JB005585.

Ducea, M., House, M.A. & Kidder, S., 2003. Late Cenozoic denudation and uplift rates in the Santa Lucia Mountains, California, *Geology,* **31,** 139–142.

Elliott, J.L., Larsen, C.F., Freymueller, J.T. & Motyka, R.J., 2010. Tectonic block motion and glacial isostatic adjustment in southeast Alaska and adjacent Canada constrained by GPS measurements, *J. Geophys. Res.,* **115,** B09407, doi:10.1029/2009JB007139.

Engebretson, D.C., Cox, A. & Gordon, R.G., 1985. Relative motions between oceanic and continental plates in the Pacific basin, *Geol. Soc. Amer. Special Paper,* **206,** 1–60.

Fletcher, J.M., Grove, M., Kimbrough, D., Lovera, O. & Gehrels, G.E., 2007. Ridge-trench interactions and the Neogene tectonic evolution of the Magdalena shelf and southern Gulf of California: insights from detrital zircon U-Pb ages from the Magdalena fan and adjacent areas, *Bull. geol. Soc. Am.,* **19,** 1313–1336.

Gans, P.B., 1997. Large-magnitude Oligo-Miocene extension in southern Sonora: implications for the tectonic evolution of northwest Mexico, *Tectonics,* **16,** 388–408.

Gosselin, J.M., Cassidy, J.F. & Dosso, S.E., 2015. Shear-wave velocity structure in the vicinity of the 2012 M_w 7.8 Haida Gwaii earthquake from receiver function inversion, *Bull. seism. Soc. Am.,* **105,** 1106–1113.

Graham, S.A., 1978. Role of Salinian block in evolution of San Andreas fault system, California, *Am. Assoc. Petr. Geol. Bull.,* **62,** 2214–2231.

Graham, S.A., Stanley, R.G., Bent, J.V. & Carter, J.B., 1989. Oligocene and Miocene paleogeography of central California and displacement along the San Andreas fault, *Bull. geol. Soc. Am.,* **101,** 711–730.

Grove, T.L., Till, C.B. & Krawczynski, M.J., 2012. The role of H_2O in subduction zone magmatism, *Annu. Rev. Earth Planet. Sci.,* **40,** 413–439.

Hall, N.T., Hunt, T.D. & Vaughan, P.R., 1994. Holocene behavior of the San Simeon fault zone, south-central coastal California, *Geol. Soc. Am. Special Paper,* **292,** 167–190.

Hanna, M.S. & Chang, T., 2000. Fitting smooth histories to rotation data, *J. Multivariate Anal.,* **75,** 47–61.

Harbert, W. & Cox, A., 1989. Late Neogene motion of the Pacific plate, *J. geophys. Res.,* **94,** 3052–3064.

Hellinger, S.J., 1981. The uncertainties of finite rotations in plate tectonics, *J. geophys. Res.,* **86,** 9312–9318.

Henry, C.D. & Aranda-Gomez, J.J., 2000. Plate interactions control middle-late Miocene, proto-Gulf and Basin and Range extension in the southern Basin and Range, *Tectonophys.,* **318,** 1–26.

Hilgen, F.J., Lourens, L.J. & Van Dam, J.A., 2012. The Neogene Period, in *The Geologic Time Scale 2012,* pp. 947–1002, eds Gradstein, F.M., Ogg, J.G., Schmitz, M. & Ogg, G., Elsevier.

Hyndman, R.D., 2015. Tectonics and structure of the Queen Charlotte fault zone, Haida Gwaii, and large thrust earthquakes, *Bull. seism. Soc. Am.,* **105,** 1058–1075.

Hyndman, R.D. & Hamilton, T.S., 1993. Queen Charlotte area Cenozoic tectonics and volcanism and their association with relative plate motions along the northeastern Pacific margin, *J. geophys. Res.,* **98,** 14 257–14 277.

Iaffaldano, G., Bodin, T. & Sambridge, M., 2012. Reconstructing plate-motion changes in the presence of finite-rotations noise, *Nat. Commun.,* **3,** 1048, doi:10.1038/ncomms2051.

Iaffaldano, G., Hawkins, R., Bodin, T. & Sambridge, M., 2014. REDBACK: Open-source software for efficient noise-reduction in plate kinematic reconstructions, *Geochem. Geophys. Geosyst.,* **15,** 1663–1670.

Jicha, B.R., Scholl, D.W., Singer, B.S., Yogodzinski, G.M. & Kay, S.M., 2006. Revised age of Aleutian Island Arc formation implies high rate of magma production, *Geology,* **34,** 661–665.

Johnson, S.Y., Hartwell, S.R. & Dartnell, P., 2014. Offset of latest Pleistocene shoreface reveals slip rate on the Hosgri strike-slip fault, offshore central California, *Bull. seism. Soc. Am.,* **104,** 1650–1662.

Kirkwood, B.H., Royer, J.-Y., Chang, T.C. & Gordon, R.G., 1999. Statistical tools for estimating and combining finite rotations and their uncertainties, *Geophys. J. Int.,* **137,** 408–428.

Kreemer, C. & Gordon, R.G., 2014. Pacific plate deformation from horizontal thermal contraction, *Geology,* **42,** 847–850.

Kreemer, C., Blewitt, G. & Bennett, R.A., 2010. Present-day motion and deformation of the Colorado Plateau, *Geophys. Res. Lett.,* **37,** L10311, doi:10.1029/2010GL043374.

Kumar, R.V. & Gordon, R.G., 2009. Horizontal thermal contraction of oceanic lithosphere: the ultimate limit to the rigid plate approximation, *J. geophys. Res.,* **114,** B01403, doi:10.1029/2007JB005473.

Langenheim, V.E., Jachens, R.C., Graymer, R.W., Colgan, J.P., Wentworth, C.M. & Stanley, R.G., 2013. Fault geometry and cumulative offsets in the central Coast Ranges, California: evidence for northward increasing slip along the San Gregorio-San Simeon-Hosgri fault, *Lithosphere,* **5,** 29–48.

Larson, R.L., Menard, H.W. & Smith, S.M., 1968. Gulf of California: a result of ocean-floor spreading and transform faulting, *Science,* **161,** 781–783.

Lewis, C.J. & Stock, J.M., 1998. Paleomagnetic evidence of localized vertical axis rotation during Neogene extension, Sierra San Fermin, northeastern Baja California, Mexico, *J. geophys. Res.,* **103,** 2455–2470.

Lonsdale, P., 1991. Structural patterns of the Pacific floor offshore of Peninsular California, in *Gulf and Peninsula Provinces of the Californias, AAPG Memoir 47,* pp, 87–125, eds Dauphin, J.P. & Simoneit, B.R.T., American Association of Petroleum Geologists.

Luyendyk, B.P., 1991. A model for Neogene crustal rotations, transtension, and transpression in southern California, *Bull. geol. Soc. Am.,* **103,** 1528–1536.

Luyendyk, B.P., Kamerling, M.J. & Terres, R.R., 1980. Geometric model for Neogene crustal rotations in southern California, *Bull. geol. Soc. Am.,* **91,** 211–217.

Luyendyk, B.P., Kamerling, M. J., Terres, R.R. & Hornafius, J.S., 1985. Simple shear of southern California during Neogene time suggested by paleomagnetic declinations, *J. geophys. Res.,* **90,** 12 454–12 466.

Marquez-Azua, B. & DeMets, C., 2009. Deformation of Mexico from continuous GPS from 1993 to 2008, *Geochem. Geophys. Geosyst.,* **10,** Q02003, doi:10.1029/2008GC002278.

Mazzotti, S., Leonard, L.J., Hyndman, R.D. & Cassidy, J.F., 2008. Tectonics, dynamics, and seismic hazard in the Canada-Alaska Cordillera, in *Active Tectonics and Seismic Potential of Alaska,* pp. 297–320, eds Freymueller, J.T. *et al.*, AGU.

McCaffrey, R., 2005. Block kinematics of the Pacific-North America plate boundary in the southwestern United States from inversion of GPS, seismological, and geologic data, *J. geophys. Res.,* **110,** B07401, doi:10.1029/2004JB003307.

McCaffrey, R., 2015. Time-dependent deformation of California from inversion of GPS time series, SCEC Annual Meeting, Palm Springs, CA.

McQuarrie, N. & Wernicke, B.P., 2005. An animated tectonic reconstruction of southwestern North America since 36 Ma, *Geosphere,* **1,** 147–172.

Merkouriev, S. & DeMets, C., 2006. Constraints on Indian plate motion since 20 Ma from dense Russian magnetic data: implications for Indian plate dynamics, *Geochem. Geophys. Geosyst.,* **7,** Q02002, doi:10.1029/2005GC001079.

Merkouriev, S. & DeMets, C., 2008. A high-resolution model for Eurasia-North America plate kinematics since 20 Ma, *Geophys. J. Int.,* **173,** 1064–1083.

Merkouriev, S. & DeMets, C., 2014. High-resolution estimates of Nubia-North America plate motion: 20 Ma to present, *Geophys. J. Int.,* **196,** 1281–1298.

Michaud, F. *et al.*, 2004. Motion partitioning between the Pacific plate, Baja California, and the North America plate: the Tosco-Abreojos fault revisited, *Geophys. Res. Lett.,* **31,** L08604, doi:10.10292004GL019665.

Michaud, F. *et al.*, 2006. Oceanic-ridge subduction vs. slab break off: Plate tectonic evolution along the Baja California Sur continental margin since 15 Ma, *Geology,* **34,** 13–16.

Miller, D.D., 1999. Sequence stratigraphy and controls on deposition of the Upper Cenozoic Tulare Formation, San Joaquin Valley, California, [*Ph. D. thesis*], 179 p.

Minster, J.B. & Jordan, T.H., 1978. Present-day plate motions, *J. geophys. Res.,* **83,** 5331–5354.

Minster, J.B. & Jordan, T.H., 1987. Vector constraints on western U.S. deformation from space geodesy, neotectonics, and plate motions, *J. geophys. Res.,* **92,** 4798–4804.

Minster, J.B., Jordan, T.H., Molnar, P. & Haines, E., 1974. Numerical modeling of instantaneous plate tectonics, *Geophys. J. R. astr. Soc.,* **36,** 541–576.

Namson, J.S. & Davis, T.L., 1988. Seismically active fold and thrust belt in the San Joaquin Valley, central California, *Bull. geol. Soc. Am.,* **100,** 257–273.

Nicholson, C., Sorlien, C., Atwater, T., Crowell, J. & Luyendyk, B., 1994. Microplate capture, rotation of the Western Transverse Ranges, and initiation of the San Andreas Transform as a low-angle fault system, *Geology,* **22,** 491–495.

Noriega, G.R., Arrowsmith, J.R., Grant, L.B. & Young, J.J., 2006. Stream channel offset and late Holocene slip rate of the San Andreas Fault at the Van Matre ranch site, Carrizo Plain, California, *Bull. seism. Soc. Am.,* **96,** 33–47.

Ogg, J.G., 2012. Geomagnetic polarity time scale, in *The Geologic Time Scale 2012,* pp. 85–113, eds Gradstein, F.M., Ogg, J.G., Schmitz, M. & Ogg, G., Elsevier.

Oskin, M. & Stock, J., 2003. Pacific-North America plate motion and opening of the Upper Delfin Basin, northern Gulf of California, Mexico, *Bull. geol. Soc. Am.,* **115,** 1173–1190.

Oskin, M., Stock, J. & Martin-Barajas, A., 2001. Rapid localization of Pacific-North America plate motion in the Gulf of California, *Geology,* **29,** 459–462.

Page, B.M., Thompson, G.A. & Coleman, R.G., 1998. Late Cenozoic tectonics of the central and southern Coast Ranges of California, *Bull. geol. Soc. Am.,* **110,** 846–876.

Perry, S.E., Garver, J.I. & Ridgway, K.D., 2009. Transport of the Yakutat Terrane, southern Alaska: evidence from sediment petrology and detrital zircon fission-track and U/Pb double dating, *J. Geol.,* **118,** 156–173.

Plafker, G., Moore, J.C. & Winkler, G.R., 1994. Geology of the southern Alaska margin, in *The geology of Alaska, Geology of North America,* G-1, pp. 389–449, eds Plafker, G. & Berg, H.C., Geol. Soc. Am.

Plattner, C., Malservisi, R., Dixon, T.H., LaFemina, P., Sella, G., Fletcher, J. & Vidal-Suarez, F., 2007. New constraints on relative motion between the Pacific plate and Baja California microplate (Mexico) from GPS measurements, *Geophys. J. Int.,* **170,** 1373–1380.

Rohr, K.M.M. & Currie, L., 1997. Queen Charlotte basin and Coast Mountains: paired belts of subsidence and uplift caused by a low-angle normal fault, *Geology,* **25,** 819–822.

Rohr, K.M.M. & Tryon, A.J., 2010. Pacific-North America plate boundary reorganization in response to a change in relative plate motion: offshore Canada, *Geochem. Geophys. Geosyst.,* **11,** Q06007, doi:10.1029/2009GC003019.

Rohr, K.M.M., Scheidhauer, M. & Trehu, A.M., 2000. Transpression between two warm mafic plates: the Queen Charlotte Fault revisited, *J. geophys. Res.,* **105,** 8147–8172.

Rolandone, F. *et al.*, 2008. Aseismic slip and fault-normal strain along the central creeping section of the San Andreas fault, *Geophys. Res. Lett.,* **35,** L14305, doi:10.1029/2008GL034437.

Royer, J.-Y. & Chang, T., 1991. Evidence for relative motions between the Indian and Australian plates during the last 20 Myr from plate tectonic reconstructions: implications for the deformation of the Indo-Australian plate, *J. geophys. Res.,* **96,** 11 779–11 802.

Royer, J.-Y., Gordon, R.G. & Horner-Johnson, B.C., 2006. Motion of Nubia relative to Antarctica since 11 Ma: implications for Nubia-Somalia, Pacific-North America, and India-Eurasia motion, *Geology,* **34,** 501–504.

Schmalzle, G., Dixon, T., Malservisi, R. & Govers, R., 2006. Strain accumulation across the Carrizo segment of the San Andreas fault, California: impact of laterally varying crustal properties, *J. Geophys. Res.,* **111,** B05403, doi:10.1029/2005JB003843.

Seiler, C., Fletcher, J.M., Quigley, M.C., Gleadow, A. J.W. & Kohn, B.P., 2010. Neogene structural evolution of the Sierra San Felipe, Baja California: evidence for proto-gulf transtension in the Gulf Extensional Province?, *Tectonophys,* **488,** 87–109.

Sella, G.F., Stein, S., Dixon, T.H., Craymer, M., James, S., Mazzotti, S. & Dokka, R.K., 2007. Observation of glacial isostatic adjustment in "stable" North America with GPS, *Geophys. Res. Lett.,* **34,** L02306, doi:10.10292006GL027081.

Sempere, J-C., Macdonald, K.C. & Miller, S.P., 1987. Detailed study of the Brunhes/Matuyama reversal boundary on the East Pacific Rise at 19 °30' S: implications for crustal emplacement processes at an ultra fast spreading center, *Mar. Geophys. Res.,* **9,** 1–23.

Shaw P.R. &Cande, S.C., 1990. High-resolution inversion for South Atlantic plate kinematics using joint altimeter and magnetic anomaly data, *J. geophys. Res.,* **95,** 2625–2644.

Sieh, K.E. & Jahns, R., 1984. Holocene activity of the San Andreas fault at Wallace Creek, California, *Bull. geol. Soc. Am.,* **95,** 883–896.

Smith, A.J., Hyndman, R.D., Cassidy, J.F. & Wang, K., 2003. Structure, seismicity, and thermal regime of the Queen Charlotte transform margin, *J. geophys. Res.,* **108**(B11), 2539, doi:10.1029/2002JB002247.

Snow, J.K. & Wernicke, B.P., 2000. Cenozoic tectonism in the central Basin and Range: magnitude, rate, and distribution of upper crustal strain, *Am. J. Sci.,* **300,** 659–719.

Stock, J. & Molnar, P., 1988. Uncertainties and implications of the Late Cretaceous and Tertiary position of North America relative to the Farallon, Kula, and Pacific plates, *Tectonics,* **7,** 1339–1384.

Stock, J.M. & Hodges, K.V., 1989. Pre-Pliocene extension around the Gulf of California and the transfer of Baja California to the Pacific plate, *Tectonics,* **8,** 99–115.

Stock, J.M. & Lee, J., 1994. Do microplates in subduction zones leave a geological record?, *Tectonics,* **13,** 1472–1487.

Sutherland, F.H., 2006. Continental rifting across the southern Gulf of California, *PhD thesis,* University of California, San Diego.

Sutherland, F.H. *et al.*, 2012. Middle Miocene to early Pliocene oblique extension in the southern Gulf of California, *Geosphere,* **8,** 752–770.

Titus, S.J., Dyson, M., DeMets, C., Tikoff, B., Rolandone, F. & Burgmann, R., 2011. Geologic versus geodetic deformation adjacent to the San Andreas fault, central California, *Bull. geol. Soc. Am.,* **123,** 794–820.

Tong, X., Smith-Konter, B. & Sandwell, D.T., 2014. Is there a discrepancy between geological and geodetic slip rates along the San Andreas Fault system? *J. geophys. Res.,* **119,** 2518–2538.

Umhoefer, P.J., Mayer, L. & Dorsey, R.J., 2002. Evolution of the margin of the Gulf of California near Loreto, Baja California Peninsula, Mexico, *Bull. geol. Soc. Am.,* **114,** 849–868.

Wessel, P. & Smith, W.H.F., 1991. Free software helps map and display data, *EOS, Trans. Am. Geophys. Un.,* **72,** 441–446.

Wilson, D.S., McCrory, P.A. & Stanley, R.G., 2005. Implications of volcanism in coastal California for the Neogene deformation history of western North America, *Tectonics,* **24,** TC3008, doi:10.1029/2003TC001621.

Wu, X., Collilieux, X., Altamimi, Z., Vermeersen, B.L.A., Gross, R.S. & Fukumori, I., 2011. Accuracy of the international terrestrial reference frame origin and Earth expansion, *Geophys. Res. Lett.,* **38,** L13304, doi:10.1029/2011GL047450.

SUPPORTING INFORMATION

Additional Supporting Information may be found in the online version of this paper:

Table S1. North America-Pacific best-fitting finite rotations and rotation covariances.
Table S2. Sierra Nevada-Great Valley microplate relative to Pacific plate finite rotations.
Figure S1. (a) Motions of North America plate continuous GPS sites corrected for the rotation of the North America plate in IGS08. The angular velocity that was used to correct all of the GPS site velocities shown in panel (a) is given in Table 1 of the main paper and was derived from the velocities of 908 intraplate stations, as described and illustrated in the main paper. The velocities shown in red and blue show GPS sites whose velocities were and were not used to estimate the best-fitting North America-IGS08 angular velocity, respectively.For clarity, sites moving faster than 12 mm yr^{-1} were omitted from the figure. (b) Distribution of vertical rates in IGS08. Fig. S2 shows additional detail for the vertical rates. Site names in panel (a) are visible on high magnification.
Figure S2. Vertical rates in areas of the North America plate interior with high concentrations of GPS sites and glacial isostatic rebound.

The upper map subdivides the eastern half of North America into three NNE-oriented transects that are roughly orthogonal to the hinge line (at 0 km) that separates areas of glacial isostatic uplift from areas that are subsiding. The three transects below the map show vertical GPS site rates as a function of great-circle distance orthogonal to the hinge line.
Figure S3. Likelihood of changes in pole locations (dashed lines) and angular opening rates (solid lines) during the past 20 Myr for the Pacific–Antarctic (a), Nubia–North America (b), and Nubia–Antarctic (c) plate pairs from REDBACK (Bayesian) analyses of their respective best-fitting rotation sequences (see the text). Narrow peaks define periods when well-timed changes in motion were the most likely to have occurred. The likelihood of change within the millions of models that were sampled for the Bayesian analysis is normalized to 1.0.
Figure S4. Pacific–North America best-fitting, noise-reduced and spline poles. The latter poles were derived using the cross-validation method of Hanna & Chang (2000), as discussed in the text. As shown in the legend, solid circles connected by the red line show the noise-reduced, finite rotation poles, open circles connected by the black line show the best-fitting finite rotation poles, and stars connected by the blue line show the spline poles.
Figure S5. Comparison of Pacific plate interval rates (a) and directions (b) relative to the North America plate estimated with stage angular velocities determined from the best-fitting, noise-reduced and spline-smoothed finite rotations. Velocities are estimated at 36.0°N, 120.6°W along the San Andreas Fault of central California. Two sets of interval velocities were derived from the best-fitting finite rotations in Table 4. One, shown by the red triangles, averages motion over the shortest possible intervals between the finite rotations. The other, shown by the grey circles, employs longer averaging intervals (0.8–2 Myr) as a means of suppressing noise. The horizontal dashed lines show the averaging interval that each velocity spans. All uncertainties are 1σ and are propagated from the interval rotation covariances. The light blue line in (b) shows the San Andreas Fault (SAF) azimuth in central California. (http://gji.oxfordjournals.org/lookup/suppl/doi:10.1093/gji/ggw305/-/DC1)

Please note: Oxford University Press is not responsible for the content or functionality of any supporting materials supplied by the authors. Any queries (other than missing material) should be directed to the corresponding author for the paper.